

Nuclear Magnetic Resonance in pulsed high magnetic fields

Von der Fakultät für Physik und Geowissenschaften

der Universität Leipzig

genehmigte

DISSERTATION

zur Erlangung des akademischen Grades

Doktor rerum naturalium

Dr. rer. nat.

vorgelegt

von Dipl.-Phys. Benno Meier
geboren am 01.10.1984 in Geseke

Gutachter: Prof. Dr. Jürgen Haase
Prof. Dr. Andrew G. Webb

Tag der Verleihung: 19. November 2012

Wissenschaftlicher Werdegang

1995 - 2004	Abitur am Gymnasium Petrinum Brilon (1,4)
Oktober 2004	Studium der Physik an der Universität Leipzig
Februar 2009	Abschluss des Studiums mit Auszeichnung (1,0) Diplomarbeit: Hochfeld-NMR an Hochtemperatur-Supraleitern
seit März 2009	Promotion an der Universität Leipzig zum Thema Nuclear Magnetic Resonance in pulsed high magnetic fields Mitglied der Leipzig School of Natural Sciences - BuildMoNa
seit April 2011	Wissenschaftlicher Mitarbeiter am Helmholtz-Zentrum Dresden-Rossendorf (10h / Woche)

Stipendien

Alumnus der Studienstiftung des deutschen Volkes

Stipendiat bei e-fellows.net

Bibliographische Beschreibung

Meier, Benno

Nuclear Magnetic Resonance in pulsed high magnetic fields

Universität Leipzig, Dissertation

99 S.*, 62 Lit.*, 53 Abb., 1 Anhang

Referat

Höchste Magnetfelder haben sich zu einem unverzichtbaren Werkzeug der Festkörperphysik entwickelt. Sie werden insbesondere verwendet, um die elektronischen Eigenschaften von modernen Materialien zu erforschen. Da Magnetfelder oberhalb von 45 Tesla nicht mehr mit statischen (z.B. supraleitenden) Feldern zu erreichen sind, haben sich weltweit verschiedene Labore auf die Erzeugung gepulster Magnetfelder mit angestrebten Maximalwerten von 100 Tesla spezialisiert.

In der vorliegenden Arbeit werden Anwendungsmöglichkeiten der kernmagnetischen Resonanz (NMR) in gepulsten Magnetfeldern aufgezeigt. Es ist gelungen, die starke Zeitabhängigkeit der gepulsten Magnetfelder mittels NMR präzise zu vermessen. Die genaue Kenntnis des Magnetfelds nach dem Puls ermöglicht, die Zeitabhängigkeit aus den Daten zu entfernen, sodass auch eine kohärente Signal-Mittelung möglich ist. Davon ausgehend werden erstmalig Messungen der chemischen Verschiebung, der Knight Shift, der Spin-Gitter-Relaxationsrate $1/T_1$ und der Spin-Spin-Relaxationsrate $1/T_2$ diskutiert.

Schließlich werden die im Zusammenhang mit gepulsten Magnetfeldern erarbeiteten Gleichungen in vereinfachter Form zur genauen Messung und Analyse des freien Induktions-Zerfalls von ^{19}F Kernspins in Calciumfluorid verwendet. Durch Messung des Zerfalls über sechs Größenordnungen wird eine genaue Analyse bezüglich einer neuartigen Theorie ermöglicht, welche den Zerfall basierend auf der Annahme mikroskopischen Chaos' erklärt. Diese Theorie hat das Potenzial, zu einem tieferen Verständnis von Quantenchaos in makroskopischen Vielteilchensystemen zu führen.

*... S. (Seitenzahl insgesamt)

... Lit. (Anzahl der im Literaturverzeichnis ausgewiesenen Literaturangaben)

Contents

1. Introduction	1
2. NMR Concepts	5
2.1. Zeeman Interaction	5
2.2. Dipolar Interaction	8
2.3. Spin-lattice Relaxation	10
3. The NMR spectrometer and its implementation in the pulsed field lab	13
3.1. The Hochfeld-Magnetlabor Dresden	13
3.2. The spectrometer	16
3.2.1. Requirements for a pulsed field NMR spectrometer	16
3.2.2. Implementation into the pulsed field facility	16
3.2.3. Hardware	17
3.2.4. Software	22
3.3. Probe	25
3.4. Performance	27
3.4.1. Noise	28
3.4.2. Excitation	30
3.4.3. Signal	31
3.5. Discussion	32
4. NMR and the time dependence of pulsed magnetic fields	33
4.1. Experimental	33
4.2. Estimate of $B(t)$ at low field	34
4.3. Time and Phase	37
4.3.1. Offset excitation	38
4.3.2. Offset precession	40
4.3.3. Fit results	41
4.3.4. Demodulation	41
4.4. Field measurement at 44 Tesla	43
4.5. Field measurement at 62 Tesla	44
4.6. Discussion	46

5. Advanced NMR experiments in pulsed fields	47
5.1. Exploratory measurements of the field homogeneity	47
5.1.1. Experimental	48
5.1.2. Results	49
5.2. Measurements in a dual coil	51
5.2.1. Experimental	52
5.2.2. Results	53
5.3. Chemical shift	55
5.3.1. Experimental	56
5.3.2. Results	56
5.4. Knight shift	57
5.4.1. Experimental	57
5.4.2. Results	57
5.4.3. Discussion	58
5.5. Measurement of the spin-spin relaxation rate	61
5.5.1. Experimental	61
5.5.2. Results	62
5.5.3. Discussion	62
5.6. Carr-Purcell sequence at 62 Tesla	66
5.6.1. Experimental	66
5.6.2. Results	67
5.6.3. Discussion	67
5.7. Measurement of the spin-lattice relaxation rate	68
5.7.1. Experimental	68
5.7.2. Results	69
5.7.3. Discussion	69
6. Eigenmodes in the long-time behavior of a coupled spin system	73
6.1. Introduction	73
6.2. Description in terms of chaotic dynamics	75
6.3. Experimental	79
6.4. Results	80
6.4.1. Solid echoes	80
6.4.2. Free induction decay	81
6.5. Discussion	83
6.6. Conclusion	87
7. Conclusion	89

A. Composition of the CaF₂ FID for B parallel (100)	93
---	-----------

Abbreviations

BPP Bloembergen, Purcell, and Pound

EPR Electron Paramagnetic Resonance

FID Free Induction Decay

HLD Hochfeld-Magnetlabor Dresden

HZDR Helmholtz-Zentrum Dresden-Rossendorf

IFW Leibniz-Institut für Festkörper- und Werkstoffforschung

KS3 Kompakt-Spule 3 (compact coil 3)

LOESS Local Regression

LP Long-Pulse Coil

NMR Nuclear Magnetic Resonance

NMRD NMR Dispersion

PRE Paramagnetic Relaxation Enhancement

RF Radio Frequency

SNR Signal-to-Noise Ratio

1. Introduction

High magnetic fields are an indispensable tool for modern materials science, in particular for the investigation of correlated electronic systems. The rather high energies required to tune the electronic properties demand correspondingly large field strengths. Since superconducting magnets currently are limited to fields up to 23.5 Tesla, designated high magnetic field laboratories provide static as well as pulsed, transient fields. High static fields, generated using resistive magnets, are currently limited to 45 Tesla. Therefore, transient pulsed methods have been developed, which have reached 100 Tesla very recently. Standard experiments in these fields concern resistivity and magnetization.

Since we also need local probes that can study the electronic properties at high fields, we explore in this thesis possible applications of nuclear magnetic resonance (NMR) in pulsed high magnetic fields up to 62 Tesla at the newly established Hochfeld-Magnetlabor Dresden-Rossendorf (HLD).

These fields are generated by discharging a large capacitor bank through a resistive coil. Therefore, their time dependence resembles that of a simple LC circuit; the electrical energy of the charged capacitor is first transformed into magnetic field energy that is converted into heat in the coil, eventually. After the pulse, the coil is cooled in a bath of liquid nitrogen. For a maximum field pulse, this process can take from two hours up to a full day depending on the coil design. The strong time dependence of the magnetic field, the low repetition rate, and the rather large inhomogeneity of the used coils have long hampered an in-depth investigation of perspectives for NMR in pulsed magnetic fields.

While especially NMR itself has greatly profited from the development of superconducting magnets with field strengths of nowadays more than 20 Tesla, a few laboratories worldwide have focussed on the generation of higher static fields of up to 45 Tesla. These fields can only be generated by using resistive magnets or hybrid magnets comprised of an outer superconducting magnet and a resistive insert. Due to the resistivity of the coils tremendous amounts of electrical energy and corresponding cooling capacities are needed. The high operating costs of resistive magnets as well as the urge towards even higher fields have led to the development of the above mentioned pulsed field technologies.

Today, pulsed magnetic fields are routinely used to probe field-dependent phenomena in condensed matter physics. The applied methods usually study bulk properties of the investigated materials; resistivity, magnetization and ultrasound are the most important ones. Other measurements, such as specific heat, electron paramagnetic resonance (EPR), but also NMR, can be considered to be in development.

The first successful NMR experiments have been performed at the Leibniz-Institut für Festkörper- und Werkstoffforschung (IFW), Dresden, Germany in 2003 by Haase et al. [1]. Subsequently, the method was expanded towards higher fields of up to 58 Tesla [2]. Kozlov et al. reported the first spin echoes in pulsed magnetic fields at a Larmor frequency of 2.4 GHz [3]. Later on, Zheng et al. performed spin echo measurements in a group at the High Magnetic Field Laboratory at KYOKUGEN, Osaka University, Japan. Finally, a group at the Laboratoire Nationale des Champs Magnétiques Intense (LNCMI), Toulouse, France, has observed first NMR signals [4].

While the quoted experiments have developed the NMR experiment towards the highest available fields, they have not solved the most fundamental problem of pulsed field NMR, i.e., the intrinsic time dependence of the pulsed magnetic fields, yet. Likewise, no NMR parameters other than the linewidth were measured prior to this thesis. Another key concern is the homogeneity of the magnetic field across the sample volume that additionally is influenced by eddy currents and mechanical vibrations.

In this work we address the above mentioned issues. We solve the challenging problem of the time dependence and demonstrate first measurements of the NMR parameters chemical and Knight shift as well as of T_1 and T_2 .

We begin by reviewing a few NMR concepts essential for its application in pulsed magnetic fields. We will then describe the home-built spectrometer and its implementation into the pulsed magnetic field laboratory. In the fourth chapter we will develop a set of equations describing the NMR signal's time dependence in pulsed magnetic fields. These equations can be used to fit the phase of the NMR signal with a set of parameters describing the time dependence of the magnetic field. As a result, the magnetic field can be determined with sub-ppm (parts per million) precision and thus effective signal-averaging is possible [5]. In chapter 5 we report on advanced NMR experiments that build on the results of the previous chapter. In terms of the linewidth we report on a first measurement indicating that the linewidth scales quadratically with the distance between sample and field center. However, there is a non-negligible constant contribution to the linewidth. In a next step we report first measurements in a dual coil extending the range of fields in which NMR can be applied to more than 90 Tesla. We then discuss first measurements of the NMR parameters mentioned above.

In the final chapter, we will address a different topic that arose from work performed in-between measurement periods at the HLD and that rests on the insight gained in methodological development of NMR.¹ We investigate the long-time behavior of a large system of dipole coupled spins in the context of a recent prediction by Fine [6, 7] based on the notion

¹Currently, the HLD has five experimental cells with pulsed magnets, three of them equipped with coils big enough to further develop NMR in pulsed magnetic fields. These cells have to serve a variety of users through the EuroMagnet II user program and additionally are used to test new coils with higher maximum fields. Therefore the total time during which measurements in pulsed fields were performed amounts to only four months.

of microscopic quantum chaos. By improving the signal-to-noise ratio by two orders of magnitude we could contribute a strong support for this fundamental theory.

Part of the work described in chapters 4 and 6 is published in [5] and [8], respectively. Where appropriate we have duplicated selected paragraphs of the original publications that were written by the author of this thesis.

2. NMR Concepts

In this chapter we discuss briefly those basic concepts of nuclear magnetic resonance which underlie the experiments described in this thesis.

We will sketch the Zeeman interaction for static and radio frequency (RF) fields and subsequently discuss the dipolar interaction in presence of a strong applied magnetic field. Taken together, these interactions will give rise to the spin Hamiltonian \mathcal{H} .

The dynamics of a spin system are usually characterized by the transversal *spin-spin* relaxation time T_2 and the longitudinal *spin-lattice* relaxation time T_1 . While the former corresponds to couplings between spins such as the dipolar coupling, the latter describes how the coupling of the spin system to a bath called “lattice” establishes the thermal equilibrium magnetization. For the systems studied within this work, coherence losses due to T_2 occur much faster than T_1 so that we can neglect the influence of the bath in most cases. Yet, for pulsed magnetic fields the equilibration with the bath needs to happen sufficiently fast. Therefore, T_1 is usually reduced by exploiting the paramagnetic relaxation enhancement (PRE) effect; a neighbouring free electron spin promotes relaxation. We note already here that the PRE effect is itself field dependent and that there is some controversy on the underlying mechanisms which we will discuss briefly.

Of course, the concepts presented in this chapter are in no way new and most of them can be found in standard textbooks like [9–12]. More specialized literature concerning the PRE effect will be cited when appropriate.

2.1. Zeeman Interaction

Consider a magnetic moment $\boldsymbol{\mu}$ in an applied magnetic field \mathbf{B}_0 . Then, the interaction energy is given as

$$E = -\boldsymbol{\mu} \cdot \mathbf{B}_0. \quad (2.1)$$

A *nuclear* magnetic moment is directly related to the *angular momentum* \mathbf{J} of the nucleus:

$$\boldsymbol{\mu} = \gamma \mathbf{J} \quad (2.2)$$

Of course, the total angular momentum is conserved and thus the magnetic moment does not oscillate about the field (like a friction less compass needle would do), but it *precesses*

about the applied magnetic field. The ratio between magnetic moment $\boldsymbol{\mu}$ and angular momentum \mathbf{J} is the gyromagnetic ratio γ , a property of the nucleus.

Obviously, in quantum mechanics, $\boldsymbol{\mu}$ and \mathbf{J} are operators and hence the Zeeman Hamiltonian can be written as

$$\mathcal{H}_Z = -\boldsymbol{\mu} \cdot \mathbf{B}_0 = -\gamma \mathbf{J} \mathbf{B}_0 = -\gamma \hbar I_z B_0. \quad (2.3)$$

Here, we have introduced the dimensionless spin operator $\mathbf{I} = \mathbf{J}/\hbar$ and assumed the magnetic field $\mathbf{B}_0 = B_0 \mathbf{e}_z$ to be along the z -axis. The eigenvalues of I_z are simply $m = -I_z, -I_z + 1, \dots, I_z - 1, I_z$. These eigenvalues directly give the energy levels of the spin:

$$E_m = -\gamma \hbar B_0 m. \quad (2.4)$$

For a spin $I = 1/2$ we thus have two levels corresponding to $m_1 = 1/2$ and $m_2 = -1/2$; the energy splitting amounts to $\hbar \gamma B_0 = \hbar \omega$ where $\omega = \gamma B_0$ is the *Larmor* frequency.

On the other hand, the time dependence of our magnetic moment is simply given by the Heisenberg equation¹

$$\frac{d\boldsymbol{\mu}}{dt} = \frac{i}{\hbar} [\mathcal{H}_Z, \boldsymbol{\mu}] = \boldsymbol{\mu} \times \gamma \mathbf{B}_0, \quad (2.5)$$

i.e., we obtain the classical equation of motion. Note that the frequency of precession is *also* given by the Larmor frequency.²

In order to do spectroscopy, we need to induce transitions between the levels of \mathcal{H}_z . This is achieved by applying a Hamiltonian that interconnects the eigenstates m_1 and m_2 . From elementary theory of angular momentum we have $I_{\pm} = I_x \pm iI_y$, so that the application of a time-dependent field perpendicular to B_0 can cause transitions between the given states while energy is conserved.

When we derived Eq. (2.5) we did not require the field \mathbf{B}_0 to be static, yet we obtained the classical equation of motion. We may therefore use a classical treatment and ask what time-dependent field \mathbf{B}_1 we have to apply in order to best flip the magnetization into the xy -plane. In most NMR experiments, this flipping is achieved through the application of linearly polarized fields that oscillate with frequency ω_x .

Consider such a linearly polarized radio-frequency (RF) field \mathbf{B}_{RF} which oscillates along the x axis with amplitude $2B_1$, i.e., $\mathbf{B}_{\text{RF}}(t) = 2B_1 \cos(\omega_x t) \mathbf{e}_x$. The field can be decomposed into two counter-rotating circularly polarized fields \mathbf{B}_+ and \mathbf{B}_- :

$$\begin{aligned} \mathbf{B}_+(t) &= B_1 (\cos(\omega_x t) \mathbf{e}_x + \sin(\omega_x t) \mathbf{e}_y) \\ \mathbf{B}_-(t) &= B_1 (\cos(\omega_x t) \mathbf{e}_x - \sin(\omega_x t) \mathbf{e}_y) \\ \Rightarrow \mathbf{B}_{\text{RF}}(t) &= \mathbf{B}_+(t) + \mathbf{B}_-(t) = 2B_1 \cos(\omega_x t) \mathbf{e}_x \end{aligned} \quad (2.6)$$

¹The result is obtained by exploiting the commutation relations for the components of an angular momentum operator.

²The time-dependence of the magnetic moment can of course be exploited by means of Faraday's law of induction: The precession of the magnetic moment about the magnetic field will induce a voltage in a coil wound around any axis with a component perpendicular to the applied field. The voltage will reach it's maximum if the magnetization precesses exactly in the xy -plane.

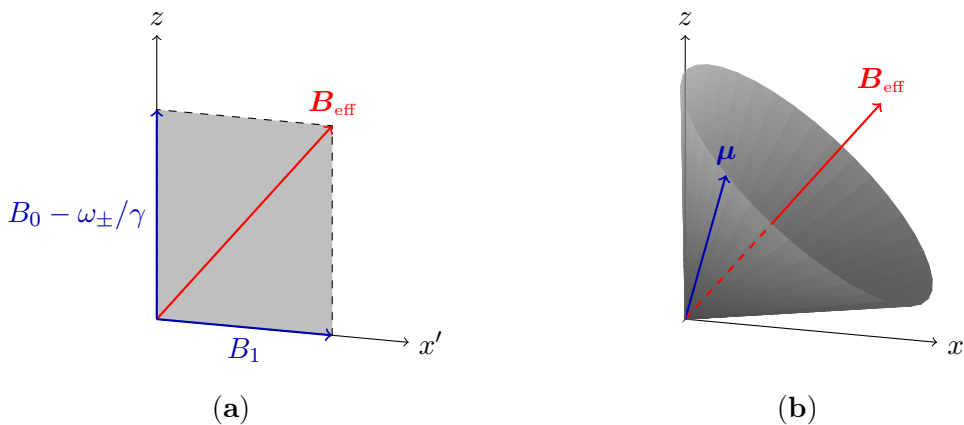


Figure 2.1.: Effective field \mathbf{B}_{eff} in the rotating frame. (a) On resonance, the z -component of the effective field vanishes, i.e., either $\gamma B_0 = \omega_+$ (positive γ) or $\gamma B_0 = \omega_-$ (negative γ); close to resonance, only the part of \mathbf{B}_{RF} that rotates in the same sense as the magnetization has to be taken into account. (b) The magnetization precesses about the effective field, describing a cone. Adapted from [9].

Now, we ask what happens if we apply *either* \mathbf{B}_+ or \mathbf{B}_- . Following Slichter's convention, we use $\omega_{\pm} := \pm\omega_x$ and define

$$\mathbf{B}_1^{\pm}(t) = B_1(\cos(\omega_{\pm}t)\mathbf{e}_x + \sin(\omega_{\pm}t)\mathbf{e}_y). \quad (2.7)$$

Then, ω_+ corresponds to \mathbf{B}_+ and ω_- corresponds to \mathbf{B}_- , respectively. In either case, the time evolution of the magnetization will be given by taking into account the total applied field:

$$\frac{d\boldsymbol{\mu}}{dt} = \boldsymbol{\mu} \times \gamma (\mathbf{B}_0 + \mathbf{B}_1^{\pm}(t)) \quad (2.8)$$

This equation is simplified by using a coordinate system which itself rotates at the frequency of $\mathbf{B}_1(t)$ about the z -axis of the laboratory frame, i.e., the *rotating frame* (denoted with a prime). In such a coordinate system, \mathbf{B}_1 is static. Of course, the time derivative of any quantity in the laboratory frame equals its time derivative in the rotating frame plus the angular velocity of the rotating frame, therefore:

$$\frac{d\boldsymbol{\mu}}{dt} = \left(\frac{d\boldsymbol{\mu}}{dt}\right)' + \omega_{\pm}\mathbf{e}_z \times \boldsymbol{\mu}' \quad (2.9)$$

If we combine equations (2.9) and (2.8), we obtain

$$\left(\frac{d\boldsymbol{\mu}}{dt}\right)' = \boldsymbol{\mu}' \times [(\gamma B_0 - \omega_{\pm})\mathbf{e}_z + \gamma B_1\mathbf{e}_{x'}] \quad (2.10)$$

Thus, in the rotating frame, the magnetization precesses about an effective magnetic field \mathbf{B}_{eff} which has a z component of $B_0 - \omega_{\pm}/\gamma$ and a x component of B_1 . The situation is summarized in Fig. 2.1. Note that the z component of the effective field vanishes for $\gamma B_0 = \omega_{\pm}$, i.e., if the resonance condition is fulfilled. In this case, the magnetization

precesses about the x' -axis with angular frequency $\omega_1 = \gamma B_1$. After some time τ , the magnetization will lie along the $-y'$ -direction, $\omega_1 \tau = \pi/2$. The time τ is called the $\pi/2$ pulse length.

Note that the above discussion bears some additional importance for NMR in pulsed high magnetic fields. In these fields, the applied field B_0 changes with time.³ Thus, the effective field almost always has a non-vanishing z -component. In order to effectively flip the magnetization into the xy -plane it is therefore important to use relatively strong B_1 fields. Also, the different tilt of the effective field at different times will lead to varying initial phases of the magnetization immediately after the pulse. We will discuss these issues in greater detail in the following chapters.

So far, we have considered non-interacting nuclear magnetic moments. In what follows, we will discuss the dipolar interaction that couples neighbouring spins. A model system for macroscopic, dipole coupled systems is CaF_2 , where the spin 1/2 fluorine nuclei sit on a simple cubic lattice. (Due to their low abundance and their small magnetic moment the Ca spins can be neglected.) The long-time behavior of CaF_2 spins is interpreted in the last chapter 6 in terms of a recent theory by B. Fine [6, 7] based on the notion of microscopic chaos.

2.2. Dipolar Interaction

The typical strength of nuclear magnetic dipole dipole interactions is of the order of 10 kHz, compared to a Zeeman interaction of typically 100 MHz. It is therefore an excellent approximation to treat the dipolar interaction as a weak perturbation. The dipolar Hamiltonian is obtained by summing up all pairwise interactions between different nuclear magnetic moments,⁴

$$\mathcal{H}_{\text{dip}} = \frac{\gamma_n^2 \hbar^2}{2} \sum_{j,k,j \neq k}^N \left[\frac{\mathbf{I}_j \mathbf{I}_k}{r_{jk}^3} - \frac{3(\mathbf{I}_j \cdot \mathbf{r}_{jk})(\mathbf{I}_k \cdot \mathbf{r}_{jk})}{r_{jk}^5} \right]. \quad (2.11)$$

The usual procedure now is to rewrite the Hamiltonian in terms of lowering and raising operators, i.e.,

$$\mathcal{H}_{\text{dip}} = \frac{\gamma_n^2 \hbar^2}{2} \sum_{j,k,j \neq k}^N \frac{1}{r_{jk}^3} [A_{jk} + B_{jk} + C_{jk} + D_{jk} + E_{jk} + F_{jk}] \quad (2.12)$$

³The change is slow when compared to the Larmor frequency, but it is fast when compared to T_2 even in solids.

⁴The expression is given in cgs units. SI units are obtained by multiplication with $\mu_0/4\pi = 10^{-7}$.

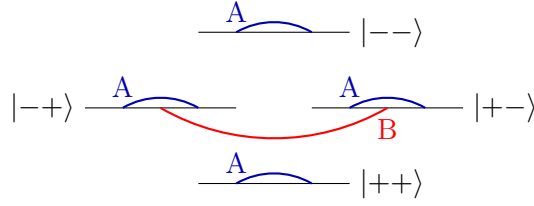


Figure 2.2.: Energy levels of a two spin system (Zeeman interaction) and contributions to the dipolar Hamiltonian that connect the corresponding states. Adapted from [9].

with A, \dots, F expressed in polar coordinates:

$$\begin{aligned}
 A_{jk} &= I_{jz} I_{kz} (1 - 3 \cos^2 \theta_{jk}), \\
 B_{jk} &= -\frac{1}{4} (I_j^+ I_k^- + I_j^- I_k^+) (1 - 3 \cos^2 \theta_{jk}), \\
 C_{jk} &= -\frac{3}{2} (I_j^+ I_{kz} + I_{jz} I_k^+) \sin \theta_{jk} \cos \theta_{jk} e^{-i\phi_{jk}}, \\
 D_{jk} &= -\frac{3}{2} (I_j^- + I_{kz} + I_{jz} I_k^-) \sin \theta_{jk} \cos \theta_{jk} e^{i\phi_{jk}}, \\
 E_{jk} &= -\frac{3}{4} I_j^+ I_k^+ \sin^2 \theta_{jk} e^{-2i\phi_{jk}}, \\
 F_{jk} &= -\frac{3}{4} I_j^- I_k^- \sin^2 \theta_{jk} e^{2i\phi_{jk}}.
 \end{aligned} \tag{2.13}$$

While A is clearly diagonal in the Zeeman basis, B is the so called flip-flop term: It simultaneously flips one spin up and one spin down. In the Zeeman basis it therefore generates off-diagonal elements joining degenerate states. The terms C, \dots, F correspond to weak transitions at zero and twice the Larmor frequency. Since they do not commute with the Zeeman interaction, they are neglected in the secular approximation.⁵ The relevant Hamiltonian is thus truncated:

$$\begin{aligned}
 \mathcal{H}_{\text{dip}}^{\text{trunc}} &= \frac{\gamma_n^2 \hbar^2}{2} \sum_{j,k,j \neq k}^N \frac{1}{r_{jk}^3} [A_{jk} + B_{jk}] \\
 &= \frac{\gamma_n^2 \hbar^2}{4} \sum_{j,k,j \neq k}^N \frac{1}{r_{jk}^3} (3I_{jz} I_{kz} - \mathbf{I}_j \cdot \mathbf{I}_k) (1 - 3 \cos^2 \theta_{jk}),
 \end{aligned} \tag{2.14}$$

and the full Hamiltonian is the sum of the Zeeman interaction and the dipolar interaction,

$$\mathcal{H} = -\gamma \hbar B_0 \sum_j^N I_{jz} + \mathcal{H}_{\text{dip}}^{\text{trunc}}. \tag{2.15}$$

Clearly, for a macroscopic sample this Hamiltonian poses a serious many-body problem that to date has not been solved (and is unlikely to ever be solved, see [10]). Experimental and theoretical works thus focus on either the short-time behavior or the long-time behavior

⁵Albeit their small intensities, due to the large difference in frequency, it is important to drop C, \dots, F for a correct calculation of moments; this was pointed out by Van Vleck, see [13]

of the NMR signal. For the long-time behavior two very different theories try to predict the signal. While one is based on a memory function approach and predicts a single exponential decay mode [14,15], Fine’s theory (mentioned above) is based on microscopic chaos: Classically, the spins can be thought of as vectors with their tips diffusing on a spherical surface. By solving the diffusion equation on such a surface, a set of exponential decay modes rather than a single mode is obtained. In chapter 6 we will present a study of these eigenmodes in the long-time behavior of fluorine spins in CaF_2 . By boosting the signal-to-noise ratio by two orders of magnitude compared to what was published so far, we obtain strong evidence for Fine’s theory.

In fact, CaF_2 is an ideal system for such an investigation not only due to the simple geometric arrangement of the spins, but also due to the availability of clean crystals with spin-lattice relaxation times of minutes and more. Therefore one is left with only one relevant time-scale set by the dipolar interaction. Quite to the contrary, in pulsed magnetic fields, there is not much time to polarize the sample. Then, for many applications it is crucial to *reduce* the spin-lattice relaxation time. This is frequently done by exploiting the paramagnetic relaxation enhancement effect which we discuss in the next section.

2.3. Spin-lattice Relaxation

The spin-lattice relaxation time T_1 describes how the nuclear magnetization equilibrates in an external field. The equilibrium magnetization is given by the Curie law, but in order to be established, there has to be some energy exchange between the spin system and a surrounding bath (called lattice). While, e.g., CaF_2 forms a well isolated spin system as mentioned above, other systems may equilibrate much faster through a variety of mechanisms. A common way to *enhance* the relaxation rate $1/T_1$ is to add paramagnetic ions to the sample. Then the motion of the electronic moments that are in equilibrium with the “lattice” causes nuclear transitions via dipole dipole interaction.

This effect was first studied by Bloembergen, Purcell and Pound (BPP) in their classic paper [16]. Depending on the effective magnetic moment μ_{eff} , the viscosity η of the solution and the gyromagnetic ratio γ of the nucleus, the relaxation rate varies linearly with the concentration of ions N and is inversely proportional to the temperature T :

$$1/T_1 = 12\pi^2\gamma^2\eta N\mu_{\text{eff}}^2/5kT \quad (2.16)$$

Herein,⁶ the effective Bohr magneton is

$$\mu_{\text{eff}} = g\mu_B\sqrt{J(J+1)} \quad (2.17)$$

where g is the g-factor, μ_B is the Bohr magneton and J is the total angular momentum

⁶Note that the given expression for $1/T_1$ assumes CGS units; if one uses SI units the expression on the right-hand side has to be multiplied by 10^{-14} to give the relaxation rate in Hz.

of the ion. In this work we will use TEMPO (a small benzene soluble molecule with a nitroxide free radical) which has $J = 1/2$ and Gd^{3+} which has $J = 7/2$.

If both the nuclear and the electron spin are part of *one* molecule, the relaxation rate of the ligands is field dependent and the effect is called paramagnetic relaxation enhancement (PRE). The dependence itself is called an NMR dispersion (NMRD) profile. The relevant interactions for the electron spin are its Zeeman interaction and the spin-orbit coupling leading to the zero-field splitting Hamiltonian \mathcal{H}_{ZFS} . On increasing the magnetic field the Zeeman interaction finally becomes stronger than \mathcal{H}_{ZFS} and the electron spins are quantized in the laboratory frame instead of the molecular frame. Therefore, a general calculation of the *electron* T_1 is very difficult and so is the calculation of the nuclear T_1 that arises through the time-dependent dipole-dipole interaction with the electron.

Due to the importance of the PRE effect, also in applications such as medical imaging (where, e.g., Gd based complexes are used as contrast agents), various attempts have been made to theoretically describe the relaxation rate's dependence on the field [17]. Briefly, it can be said that the most pronounced feature of the theoretical NMRD curves is a maximum in the relaxation rate occurring at rather high fields. In a recent study, Kowalewski et al. [18] tried to observe such a maximum by increasing the field strength to 21 Tesla. However, this field strength was not sufficient for the investigated Ni(II) salt solutions and pulsed magnetic fields may indeed be needed to validate the theoretical curves.

3. The NMR spectrometer and its implementation in the pulsed field lab

In this chapter we will first briefly describe the Hochfeld-Magnetlabor Dresden (HLD). The HLD generates pulsed high magnetic fields by discharging a 50 MJ capacitor bank through resistive coils [19, 20]. We will discuss the properties of these magnetic fields from which one can easily deduce requirements for pulsed field NMR spectrometer and probe. Both the spectrometer and the home-built probe will be described in detail. Finally we will give an account of the spectrometer's performance in terms of sensitivity.

3.1. The Hochfeld-Magnetlabor Dresden

The Hochfeld-Magnetlabor Dresden, located at the Helmholtz-Zentrum Dresden-Rossendorf (HZDR), is built around a capacitor bank (left photograph in Fig. 3.1) that can store up to 50 MJ of electrical energy. The capacitor bank consists of 24 modules that can be combined in various ways depending on the required energy and capacitance. The modules can be charged up to 23 kV and deliver 5 GW of electrical peak power. Fig. 3.1(a) shows a schematic drawing of capacitors and a coil along with photographs; Fig. 3.1(b) shows a more complete drawing of one module with capacitance C attached to a coil L .

By discharging the modules through such resistive coils, high magnetic fields of up to 70 Tesla are routinely generated. The energy stored in the capacitor bank amounts to $\frac{1}{2}CV^2$ where C is the capacitance of the whole capacitor bank and V is the voltage to which it is charged. During the magnetic field pulse (hereafter referred to as “the pulse”), this energy is transformed into field energy $\int B^2/(2\mu_0)dV$ that subsequently is transformed into heat. The coils are immersed in a bath of liquid nitrogen so that they can heat up during a pulse.

Strong Lorentz forces lead to pressures of several GPa and ultimately limit the maximum fields achievable with non-destructive coils. Furthermore, high voltages and thermal shocks turn the design of such coils into a challenging task [21]. By using advanced coil designs such as dual coils, where a small inner coil is pulsed in the vicinity of the maximum field of a pulse from a larger outer coil, maximum fields of more than 90 Tesla are achievable. Following world records of 91.4 Tesla at the HLD (June 22nd, 2011) and 97.4 Tesla at the National High Magnetic Field Laboratory in Los Alamos (August 19th, 2011) the long standing landmark of 100 Tesla was taken on March 22nd, 2012 (100.75 Tesla in Los Alamos). The HLD achieved a new European record of 94.2 Tesla on January 25th, 2012.

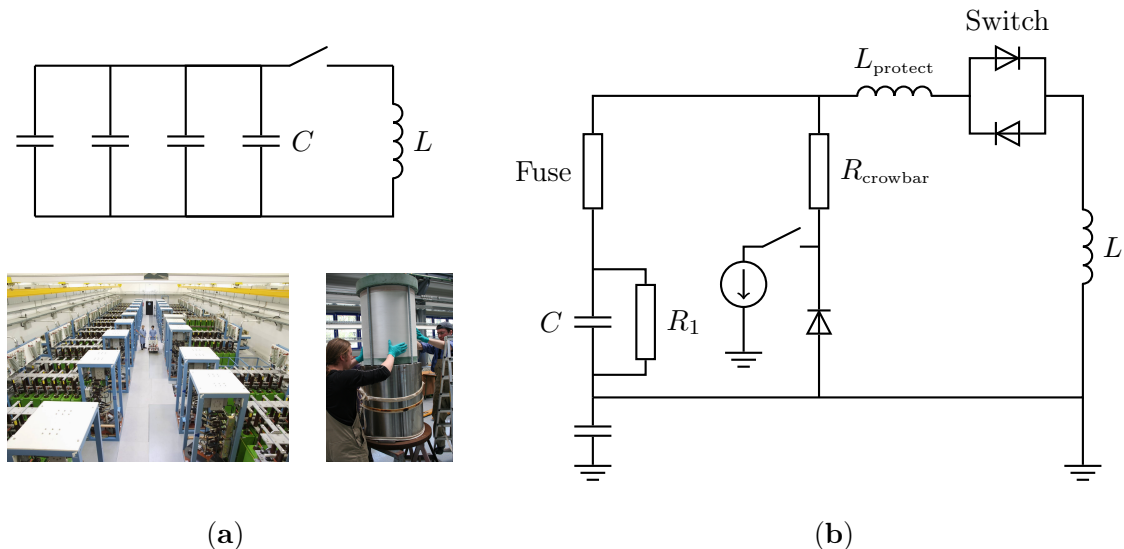


Figure 3.1.: (a) Simplified drawing of capacitors C and coil L , along with photographs of the HLD's capacitor bank and the Long-Pulse coil. (b) A more complete drawing of a single module of the capacitor bank attached to the coil L . The capacitor bank consists of 24 modules which together hold 500 capacitors that can be charged up to 23 kV corresponding to an energy of 50 MJ. After the bank is charged it is disconnected from the voltage source and the LC -circuit is closed using thyristors. A so called crowbar resistance can be used to additionally damp the circuit. A more detailed version is given in [26].

Only one day later, we carried out a first successful NMR experiment in this coil, cf. section 5.2.

The HLD is equipped with various coils to meet the requirements of a variety of experiments addressing resistivity [22], magnetization [23], ultrasound [24], electron spin resonance absorption [25] or specific heat. Since the energy needed is given by $\frac{1}{2\mu_0} \int B^2 dV$, the two small coils available at the HLD require relatively small energies for their rated maximum fields of 53 and 60 Tesla. While NMR experiments are possible and have been performed in such small coils, their low inductance leads to a very short pulse duration (to a first and reasonably good approximation the shape of the pulse is that of a LC -circuit) that seriously hampers NMR experiments beyond simple FID and spin echo sequences. Of course, the rapid time dependence of the inner coil also poses a problem for advanced NMR experiments in dual coils, but signals of metallic samples can readily be obtained so that a precise determination of the maximum field can be given.

Almost all experiments discussed in this work were performed in coils called KS3 rapid cooling (Germ., Kompakt-Spule Typ 3) and LP (Long Pulse) coils. The time dependence and the maximum of the magnetic field pulse for these coils, measured with Hall probes, are shown in Fig. 3.2.¹ In Fig. 3.2 we also plot the time dependence of the magnetic field of a dual coil. The time dependence of the inner coil (the sharp peak of the green line)

¹The data were provided by T. Herrmannsdörfer and E. Kampert.

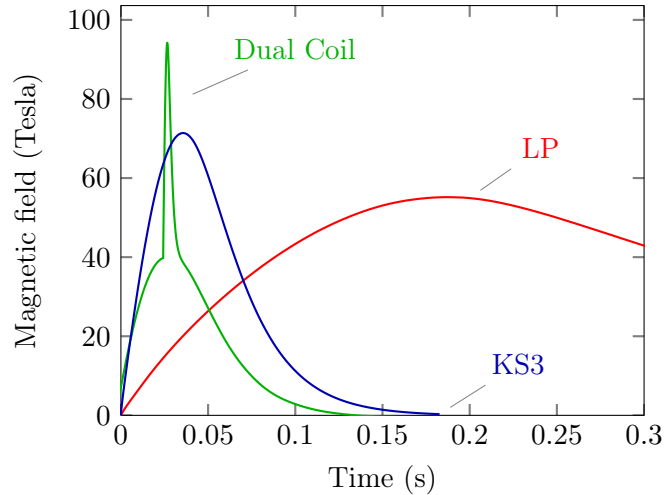


Figure 3.2.: Time dependence of the magnetic field $B(t)$ for three different coils, denoted by LP (long-pulse), KS3 (compact coil 3), and Dual Coil, measured using a Hall probe. The total energy of the LP pulse is 37 MJ, it's maximum is 55.2 Tesla. The KS3 coil has a stronger time dependence but also a higher maximum field of approximately 71.4 Tesla. Even stronger fields can only be achieved with dual coils (green line), see text. More information can be found elsewhere [27].

resembles that of coils used previously by J. Haase in the very first pulsed field NMR experiments at the Leibniz Institute for Solid State and Materials Research Dresden [1].

Since NMR experiments are normally performed in stable, static fields, the LP coil (red curve in Fig. 3.2) seems most suited to perform such experiments in pulsed fields. However, the weak time dependence demands long cooling times of up to 30 hours after a full field pulse. While the coil has yielded a maximum field of 55 Tesla, recommended maximum fields amount to only 50 Tesla.² Therefore, we performed NMR experiments also in the KS3 coil (blue curve in Fig. 3.2). Although this coil has a stronger time dependence, it is sufficiently well suited for NMR experiments: The coil is equipped with cooling channels that reduce the time needed to reach base temperature to only 2 hours and furthermore offers a maximum field of 70 Tesla. It is used routinely up to 63 Tesla; experiments discussed in the next chapter were performed in this coil at fields up to 62 Tesla.

It is important to note that the amplitude as well as the point in time of the field maximum of a magnetic field pulse depend on the coil temperature (i.e., coil resistance) and the charging state of the capacitor bank prior to the pulse. Since these parameters are not perfectly known, the reproducibility of the magnetic field pulse's maximum generally is not better than 1 %.³

Another key property of the coils in terms of NMR experiments is their homogeneity. Clearly, one does not expect to have values better than a few ppm across a reasonable

²The 55 Tesla pulse corresponds to an energy of 37 MJ. In case of a serious coil failure substantial damages on the experimental setup, including the NMR spectrometer, are likely to occur.

³At low fields a significantly better reproducibility of $\sim 1\%$ was observed in a series of experiments addressing the field homogeneity, cf. section 5.1.

sample volume of e.g. 1 mm^3 . Furthermore, the time-dependent fields will induce eddy currents that will further disturb the field's homogeneity. In general one expects larger coils to have better homogeneity for a given sample volume. As we will show in chapter 5, it is possible to achieve homogeneities of up to 20 ppm even in the smaller KS3 coil.

3.2. The spectrometer

3.2.1. Requirements for a pulsed field NMR spectrometer

The properties of the magnetic fields discussed in the previous section immediately determine the requirements a NMR spectrometer has to fulfill to be operated successfully in pulsed magnetic fields: (i) Since the field varies strongly in time and its amplitude is not known prior to the pulse, frequencies will vary by several MHz, thus a real-time bandwidth of at least 10 MHz is necessary for the receiver. (ii) For ^1H and ^{19}F nuclei, the spectrometer has to support resonance frequencies that are much higher than frequencies commonly found in NMR, e.g. 2.6 GHz for ^1H at 60 Tesla. (iii) Due to the rapid change of the field with time, all data points have to be stored on disk; signal averaging is not trivially possible. Thus, compared to standard NMR experiments, larger amounts of data are generated in short times (e.g. 10 MB in 100 ms). (iv) The uncertainty in $B(t)$ also causes the need for strong RF pulses: These pulses, employed to flip the magnetization into the xy -plane need to have a spectral width of ideally a few MHz and thus need to be shorter than a micro second. A first estimate shows that RF powers of up to 1000 W are required, cf. section 3.4.2. Finally, the NMR spectrometer has to be implemented and controlled within the pulsed field facility.

Since commercially available spectrometers invariably fail to meet these requirements, a spectrometer was designed and built according to our specifications by NMR Service, Erfurt, Germany. In what follows, we will discuss its implementation, hardware, and software as well as various extensions performed within this thesis.

3.2.2. Implementation into the pulsed field facility

A schematic layout of the pulsed field facility is shown in Fig. 3.3. The NMR spectrometer is located in a mobile 19 inch rack and can thus be used in various cells. Since the NMR data need to be acquired during the pulse, the spectrometer receives a trigger signal from the main control computer (red background in Fig. 3.3). This signal also triggers an oscilloscope that is used for various other measurements such as voltage drop across a shunt resistor and voltage induced in pick-up coils. The oscilloscope also measures the TTL pulses that unblank the NMR power amplifier so that one can lock the NMR data with the other measurements.

The main control computer of the facility is located in a separate control room and manages charging and discharging of the capacitor bank. Both the oscilloscope and the

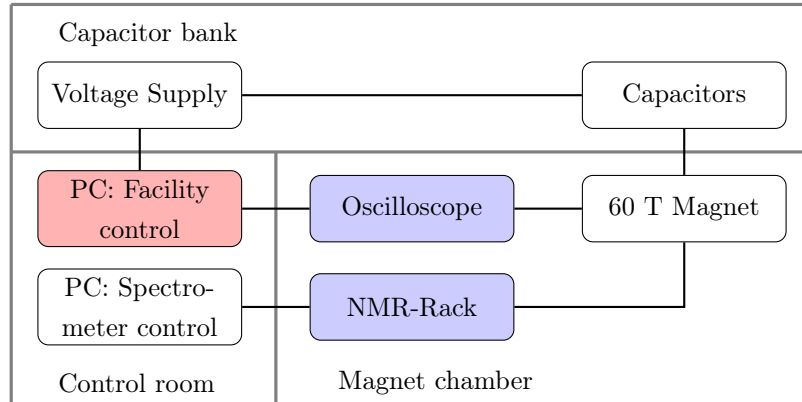


Figure 3.3.: Sketch of the implementation of the NMR system into the pulsed field facility: The central control computer (red) controls charge and discharge of the capacitor bank and triggers the NMR measurement and an oscilloscope (blue). The oscilloscope carries out various control measurements (signals from pick-up coils, voltage drop across a shunt resistor, etc.) Prior to the field pulse the spectrometer is initialized via VNC.

spectrometer are connected to the local area Network (LAN) of the facility and can be accessed from the control room. A virtual network connection (VNC) is used to initialize the NMR spectrometer.

3.2.3. Hardware

The setup of the NMR spectrometer itself is shown in Fig. 3.4. The spectrometer is built around a National Instruments (NI) PXI system that currently hosts two RF signal generators, one RF signal analyzer, a TTL waveform generator and a scope card. The second RF signal generator can be used together with the scope card and a home-built RF downconverter/demodulator to perform “double resonance” experiments in which a probe equipped with two independent resonance circuits is used to measure e.g., the z -dependence of the magnetic field with two NMR circuits. Various Mini-Circuits switches are used to shape the RF pulse and to protect the receiver during the pulse. All components are clocked by the 10 MHz reference clock of the PXI system.⁴ The access to the components is realized via a LabView interface. In what follows we give a more detailed description of the particular components.

RF signal generators

The NI PXI-5651 RF signal generator is a continuous wave generator with a frequency range of 500 kHz to 3.3 GHz. While it offers some advanced features like frequency shift keying, we use it simply to generate continuous RF output at a fixed frequency. The

⁴Note that the common clock should not be confused with a common local oscillator: Each RF device uses its own local oscillator so that the phase lag between two devices is essentially random. However, we find that the phase drift between the various devices during a single magnetic field pulse can be neglected to a good approximation.

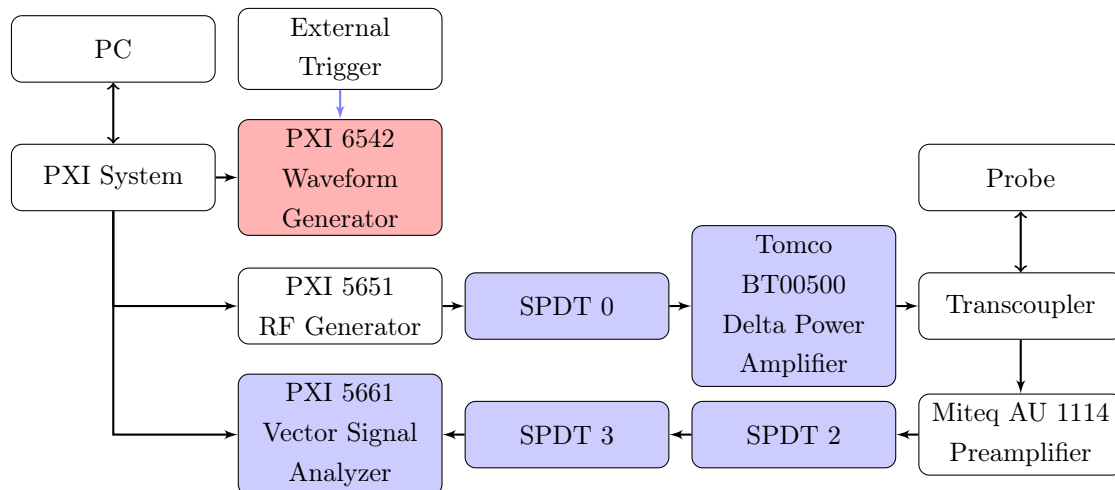


Figure 3.4.: Scheme of the spectrometer: The pulse programmer (red) is triggered externally and itself controls the switches to form the RF pulse (SPDT 0) and to protect the receiver (SPDT 2,3). It also triggers the data acquisition and unblanks the power amplifier (all components connected to the pulse programmer have blue background). The numbers of the various switches correspond to their respective TTL channels, cf. Fig. 3.11. Two additional switches to optionally attenuate the RF pulse are not shown here for clarity.

amplitude can be varied between -100 and $+10$ dBm with a resolution of 0.1 dB and an accuracy of 0.75 dB. The phase noise is specified as -110 dBc/Hz (at a carrier frequency of 1 GHz and an offset of 10 kHz).

The second RF generator is a NI PXI 5650 signal generator. It has the same specifications as the PXI 5651 but a maximum frequency of only 1.3 GHz.

RF signal analyzer

The receiver is a NI PXI-5661 vector signal analyzer. The device uses a 2.7 GHz quadrature digital downconverter to digitize signals between 9 kHz and 2.7 GHz at a real-time bandwidth of 20 MHz.

The downconverter produces intermediate frequencies (IF) between 5 and 25 MHz. The IF is digitized with 100 MS/s. The device is equipped with 256 MB so that signals can be recorded for about 1 s at full bandwidth. The typical noise density is -140 dBm/Hz (the thermal noise density is -174 dBm/Hz at 290 K). The frequency accuracy is given as ± 50 ppb. Signal levels between -130 and $+30$ dBm can be measured with a resolution of 14 bit. The typical phase noise is stated to be below -94 dBc/Hz at a 10 kHz offset.

Waveform generator

We use a NI PXI-6542 waveform generator to control the various switches, the unblanking of the power amplifier and the trigger for the signal analyzer. The device is equipped with 32 channels that can be configured as either in- or output. Additionally, four programmable

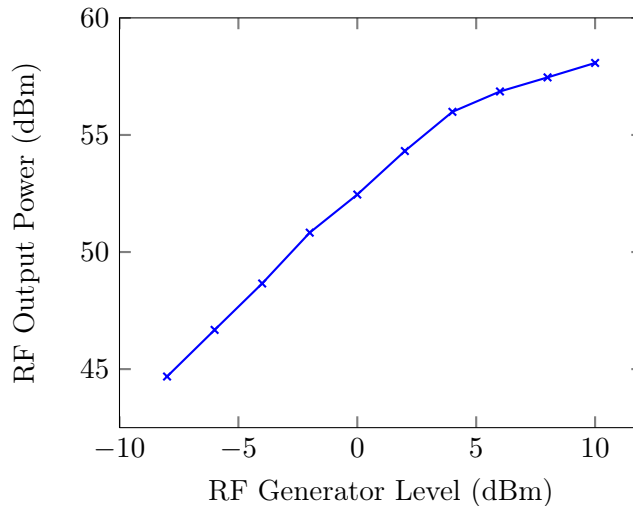


Figure 3.5.: Output level of the power amplifier as function of the specified RF signal generator level measured at a frequency of 407 MHz. When measuring this curve, a total of three TTL switches were installed after the signal generator, one to form the RF pulse and two more switches allowing for a TTL controlled 10 dB attenuation of the RF pulse. Taking into account the insertion losses of the switches, the specified maximum input power of 0 dBm would therefore have been achieved for a RF signal generator level of ~ 3 dBm. However, we found that a level of 57 dBm or 500 W is only achieved for an RF generator level of 8 dBm. The maximum measured power is 58 dBm or 640 W for an RF generator level of 10 dBm (the destruction limit of the amplifier is specified with 10 dBm). The output power was derived from the peak-to-peak voltage of a 400 ns RF pulse measured with a fast oscilloscope after attenuation with 50.7 dB (30 dB + 20 dB attenuators + 0.7 dB cable losses as measured with a network analyzer).

function interface (PFI) channels are available, one of which is used as input and receives the trigger signal from the capacitor bank. The device is compatible with 1.8, 2.5, 3.3 and 5 V logic; we use the 5 V TTL logic only. While the device offers a maximum clock rate of 100 MHz, we use it with only 10 MHz, so that the time resolution in the pulse sequence is 100 ns. See section 3.2.4 for details on the programming of the various channels.

RF switches

All switches are PIN diode single-pole-double-throw (SPDT) switches of type ZASWA-2-50DR+ by Mini-Circuits. These have built-in TTL drivers, a fast switching time of 10 ns and a high isolation of at least 70 dB for frequencies below 3 GHz. The insertion loss increases linearly from about 1 dB at 50 MHz to 2 dB at 3 GHz. Hence these switches not only are suitable to form the rf pulse but also to protect the receiver. For the applications shown in Fig. 3.4 one connection is terminated by a 50 Ohm resistor. Additionally, two switches may be used together with Mini-Circuits attenuators to produce RF pulses with variable amplitudes.

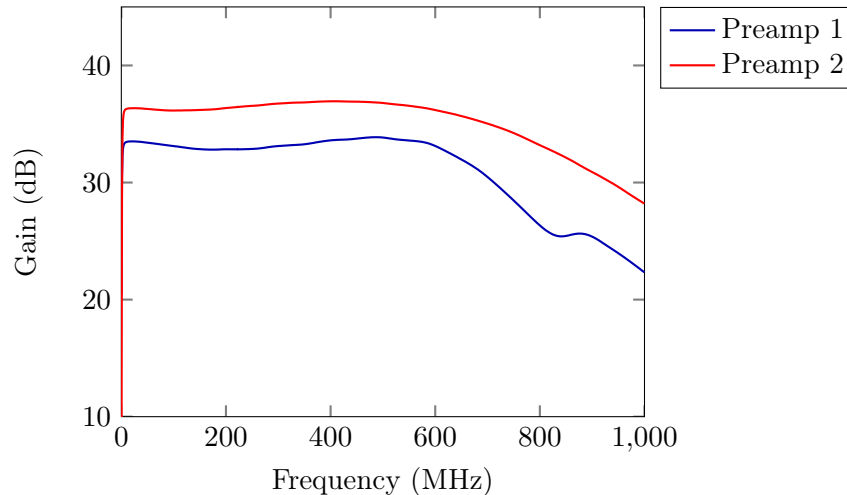


Figure 3.6.: Gain of the preamplifiers. The output of the network analyzer (port S_1) was attenuated with a 30 dB attenuator and the baseline was measured (port S_2) with 0 dBm output power. Then, the preamps were connected after the attenuator and the corresponding curves (blue and red) were measured. The recently purchased Preamp 2 offers both higher gain and higher gain flatness and in addition can be used at higher frequencies.

Power amplifier

We use a Tomco BT00500-Delta pulse amplifier with a nominal frequency range of 200 to 600 MHz. The amplification of this Class AB MOSFET device is 57 dB corresponding to a maximum power of 500 W for the maximum input level of 0 dBm, cf. Fig 3.5. The falling edge of the RF, measured from falling edge of the gate pulse to 10 % RF output voltage is specified as 50 ns. The typical rise time of the RF is specified as 100 ns. The values were checked by measuring the output of the amplifier with a fast oscilloscope. A pre-gate pulse of 5 μ s prior to the RF pulse was necessary to achieve the specified rise time. The output noise for the blanked case is stated to be below 10 dB above the thermal level (sufficiently low so that the crossed diodes separate the power amplifier from the receiver). At frequencies below 200 MHz, the device produces strong 2nd and 3rd harmonics which become less pronounced at higher frequencies. The harmonics are suppressed by various filters in the duplexers, see section 3.2.3.

In order to monitor the output of the amplifier and additionally check the matching of the probe an EME 7020/30A bidirectional coupler is used.

Preamplifier

We use two different preamplifiers, both Miteq AU1114. Preamp 1 was purchased in 2008, preamp 2 in 2012. In Fig. 3.6 we show the gain of both preamps measured between 0 and 1000 MHz. Clearly, the second preamplifier has higher gain as well as higher gain flatness and in addition is usable at frequencies much above the rated stop frequency of 500 MHz.

The noise figure of the amplifiers is given as 1.0 dB for frequencies below 200 MHz and

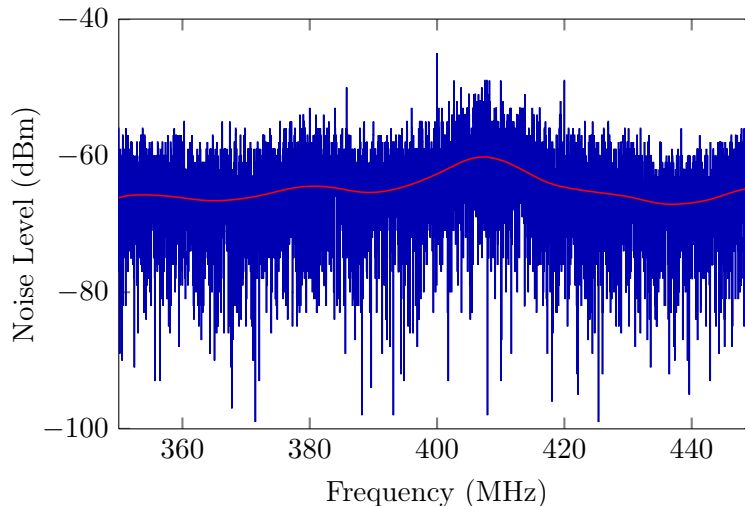


Figure 3.7.: Noise level of the NMR setup as measured with the RF signal analyzer in spectrum analyzer mode. The red curve shows the same data smoothed with a locally weighted regression (LOESS) using a Gaussian kernel of $\sigma = 1$ MHz. The smoothed curve has a maximum of -60.2 dB at the probe’s resonance frequency of 407 MHz

from there on increases approximately linearly to 1.4 dB at 500 MHz. Lacking a calibrated noise source, we could not perform a precise measurement of the noise figure for higher frequencies. The recovery time is specified as 1 μ s in good agreement with experimentally observed values.

It may be tempting to use both preamplifiers in series so that the noise level at the output of the second amplifier is much higher than that of the signal analyzer. However, the high bandwidth of the first preamplifier leads to an output power level beyond the specified maximum input of the second preamp. The device therefore does not operate linearly anymore and the output power is below the expected power level. This can be seen in Fig. 3.7 where we show the noise power of both preamplifiers connected to a probe tuned to 407 MHz. The power levels were measured with the RF signal analyzer in spectrum analyzer mode with an IF bandwidth of 1 MHz. The expected noise power for an amplification of 69.9 dB at room temperature and a bandwidth of 1 MHz is -44.1 dBm in contrast to the observed power level of only -60.2 dBm. For the time being, we therefore resort to the use of one preamp only.

Duplexer

We use custom-built duplexer from NMR Service, Erfurt, Germany. These (often also referred to as transcouplers) are three port devices which act as switches connecting either the transmitter or the receiver to the probe.⁵ Typically they are built using crossed diodes

⁵In RF terminology, a duplexer often is referred to as a device which uses simple filters to avoid crosstalk between transmitter and receiver. Of course this is only possible, if transmitter and receiver work on (at least slightly) different frequencies.

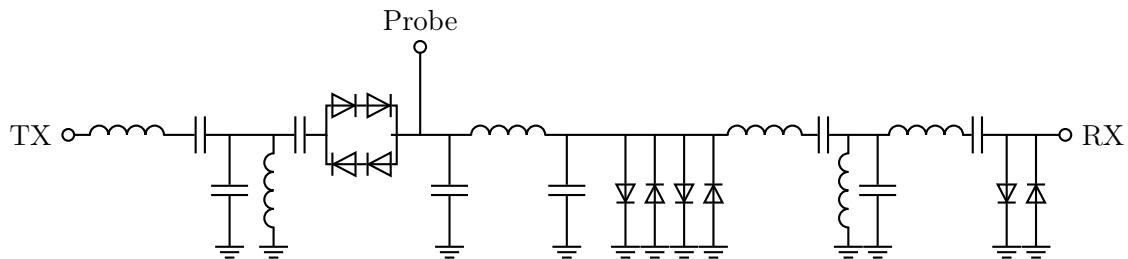


Figure 3.8.: Sketch of a typical NMR duplexer used in the pulsed field NMR setup. A filter is used to remove higher harmonics from the TX pulse. While transmitting, the diodes are opened and the RF pulse can travel to the probe (matched to 50 Ohm). In this example, the $\lambda/4$ cable is replaced by a Π network (between the probe and the four diodes towards ground). For high power levels, the diodes conduct and the impedance at the output of the Π network is $Z = 0$. The remaining capacitor and inductor form a parallel resonant circuit with a resonance frequency close to the operating frequency (leading to a large impedance / large reflection coefficient). An additional Chebyshev bandpass behind the diodes as well as another pair of diodes are built in to additionally protect the receiver.

and a $\lambda/4$ cable (or network) that acts as impedance transformer. During the strong RF pulse, the diodes at the end of the $\lambda/4$ cable are opened ($Z = 0$).

The voltage reflection coefficient, defined as [28]

$$\Gamma = \frac{Z - Z_0}{Z + Z_0} \quad (3.1)$$

therefore yields $\Gamma = -1$, so that the RF is reflected changing its phase by π .⁶ If the power amplifier is blanked, the diodes are closed and thus the amplifier is effectively disconnected from the circuit. While $\lambda/4$ cables are used in some duplexers of the pulsed field NMR spectrometer, for lower frequencies the switching is achieved through an impedance network as shown in Fig. 3.8.⁷ In addition to the switching capability, the custom built duplexers are equipped with filters to, e.g., remove the higher harmonics of the used power amplifier.

Note that if the preamplifier is cooled for better SNR, then also the duplexer (between sample and preamplifier) needs to be cooled. In this case, usually GaAs diodes with a smaller band-gap are used. When using micro-coils, smaller power levels are sufficient and one can use active switches combined with cryogenic duplexers [29]. Active switches have also been used previously for NMR in pulsed fields at frequencies above 2 GHz [3].

3.2.4. Software

The software discussed here is used only to acquire the data, all post-processing is done using Matlab or Python.⁸ Since the National Instruments devices are delivered only with

⁶For passive circuits the voltage reflection coefficient is a complex number $\Gamma = |\Gamma|e^{i\phi}$ with $0 \leq |\Gamma| \leq 1$.

When plotting Γ in polar coordinates, one obtains the Smith chart, cf. sec. 3.3.

⁷The duplexer shown in Fig. 3.8 was analyzed by H. Voigt.

⁸Initially, we relied only on Matlab. As a free, modern object-oriented programming language with an easy syntax and well developed libraries for scientific work, Python has several benefits compared to Matlab;



Figure 3.9.: Front panel of the LabView VI used to control the spectrometer. Here we measured spin echoes at 62 Tesla using a $\pi/2$ pulse of 800 ns and a refocussing pulse of 1.2 μ s, reflecting a compromise between optimal pulse length and spectral breadth. In this example, the second channel was not used; its settings can be ignored. Immediately after the experiment, the full trace of the signal analyzer is visualized in a simple plot. All post-processing is done with Matlab or Python.

LabView drivers, LabView was used to program the spectrometer. Besides initializing all the hardware, the software has to program a train of TTL/RF pulses, cf. Fig 3.11. The parameters of these pulses are entered via the graphical user interface shown in Fig. 3.9. Usually one wants to perform a pulse sequence several times, e.g., one might want to trigger an FID 40 times. Then it is sufficient to program the sequence once and repeat it 40 times with the “Number of Scans” parameter. Furthermore, one has to specify the RF frequency of the system, the output power of the RF signal generator, the sample rate (inverse dwell time) and the sensitivity of the receiver. A second channel can be programmed independently using the same waveform generator and a second RF generator. It is also possible to use the settings from the first channel (e.g., if one wants to perform equivalent experiments with two tank circuits at different positions). For testing purposes, one can disable the external trigger, data acquisition is then started by a software trigger. If the external trigger is enabled, the program always saves the experimental parameters and the

the author thus has continuously shifted towards working with Python. We have also performed some calculations/fitting with Mathematica.

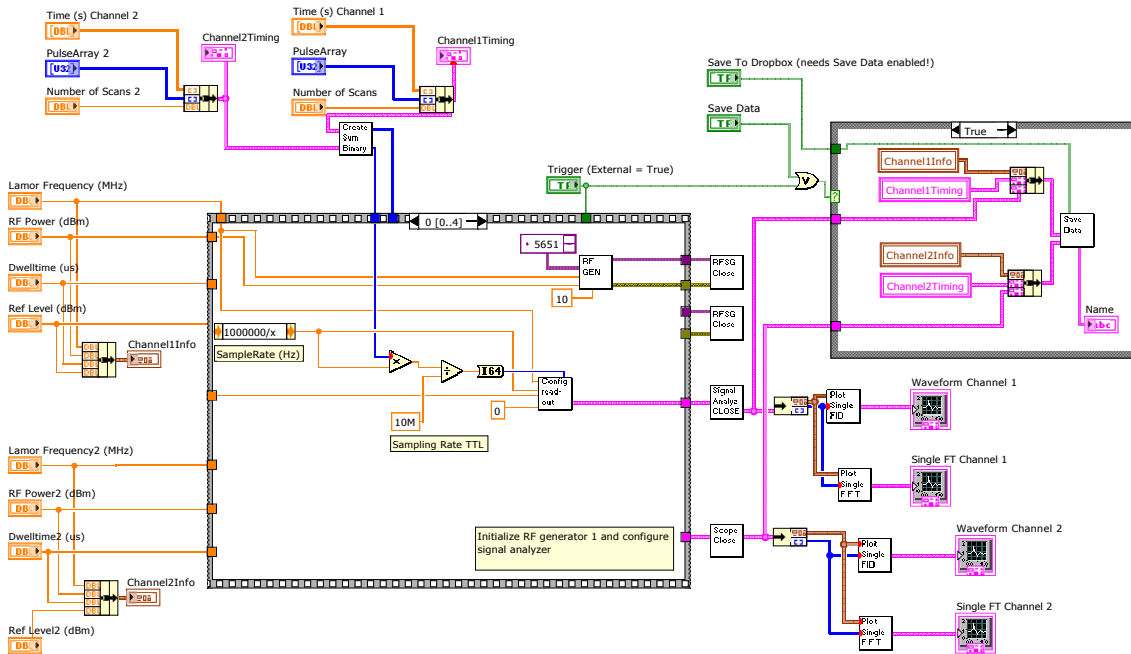


Figure 3.10.: The so called block diagram (corresponding to the front panel shown in Fig. 3.9) of the software used to control the spectrometer. All experimental settings are fed into a sequence that initializes the various components. Upon receiving a trigger, the data acquisition starts. Then, the instrument handles the data and the data are transferred to outside of the sequence. The handles are closed and the data is saved and visualized, see text.

obtained data. As an option, the data can be stored in a Dropbox folder for convenient synchronisation and post processing.

Albte we obtained the spectrometer with a working NMR program developed by NMR Service, this was completely reprogrammed by the author. The old version of the software did not use subprograms (called Virtual Instruments or VIs in LabView), so that all commands were written in a single VI making adjustments in the software practically impossible. When printed as .pdf, this VI spanned across 40 pages; in striking contrast to the “rule” that a VI should fit on a screen for clarity.

The back-end or block diagram of the new software is shown in Fig. 3.10. While the details of the plot are unimportant here, one can see that the software is organized around a central sequence (gray framed area in Fig. 3.10 with inputs on the left and outputs on the right).⁹ The sequence performs the following tasks: (i) initialize the first RF signal generator and the RF signal analyzer, (ii) initialize the second RF signal generator, (iii) initialize the scope card, (iv) wait 1 ms and (v) initialize the waveform generator and wait for the trigger. After the trigger is received, the waveform generator waits a specified time (Waiting Time in Fig. 3.9), triggers the signal analyzer and the scope and produces all

⁹In contrast to other programming languages such as Matlab or Python, the graphical programming mode of LabView leads to some ambiguity with respect to the order in which programming commands are executed. A sequence is LabViews control structure to transparently determine the order of execution.

		Time	5 μ s	800 ns	1 μ s	250 μ s
Channel 0	RF					
Channel 1	Unblanking					
Channel 2	Protect 1					
Channel 3	Protect 2					
Channel 5	RF High Power					
Channel 6	RF High Power					
Configuration (binary)			001110	111111	001000	00000
Configuration (decimal)			14	111	8	0
Configuration (name)			Unblank	RF High	Ringdown	Digitize

Figure 3.11.: Computation of values for the TTL waveform generator. During the unblanking period (first 5 μ s), the TTL signal is high on channels 1, 2, and 3. The configuration is hence $2^1 + 2^2 + 2^3 = 14$. Corresponding to the TTL sample rate of 10 MS/s, the value of 14 is written into the TTL array 50 times. Next, the value of 111 is appended to the TTL array 8 times, etc. In this example, channels 5 and 6 are both on. Then, the RF signal is simply forwarded to the power amplifier. In another configuration (named RF low, not shown here), channels 5 and 6 are off. In this case, the signal passes a 20 dB attenuator. Thus, pulses of equal spectral width with different flipping angles can be realized. The various configurations can be set conveniently in the user interface using their respective names.

the RF pulses and other TTL signals as specified by the drop down list under each time interval in Fig. 3.9, cf. Fig. 3.11. The data and experimental parameters are then saved on disk for post processing.¹⁰

3.3. Probe

The NMR probe for pulsed fields is a rather crucial element that has to be designed with great care. At least one robust, tuned and matched circuit has to be implemented; additionally the probe needs to be equipped with heating resistors and temperature sensors if experiments at room temperature need to be performed.¹¹ Eddy currents that arise through the change of the pulsed field with time have to be considered; closed loops of conducting material have to be avoided. All these requirements have to be met within a

¹⁰The trace of the signal analyzer is saved as a binary file, the experimental parameters are saved in XML files.

¹¹The HLD offers a bath and a flow cryostat. Although the flow cryostat should in principle work up to room temperature, the heating resistor of the cryostat was damaged two times. Then the cryostat needs to be exchanged, but this is only possible after the coil has reached room temperature. Therefore, such an exchange takes at least one full day. Taking into account that usually one is given only ten days for measurements every half a year, an exchange of the cryostat should be avoided. Thus, for room temperature measurements we now use only the bath cryostat and manage the sample heating locally.

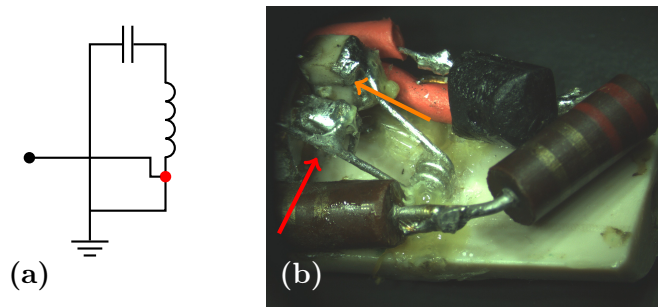


Figure 3.12.: Scheme (a) and photograph (b) of the resonance circuit. The parallel LC resonance circuit is matched to the line (50 Ohm) by tapping the coil (red point in (a), red arrow in (b)). In the microscope photograph we used two capacitors of 10 and 1 pF in parallel (indicated by the orange arrow). With three turns, the coil's diameter and length were 1.1 and 1.8 mm, respectively. The coil's legs are comparatively long (reducing the sensitivity). In (b), the sample cannot be seen since it is covered with glue. Also shown are the heating resistors and the temperature sensor.

small diameter of typically 13 mm, much less than what is available in designs for static fields. Furthermore, taking into account the rather large inhomogeneity of the pulsed field coils, the sample has to be positioned with a precision significantly better than 1 mm.

In what follows, we describe in more detail the probe built within this thesis. It meets the above requirements and furthermore is equipped with a second semi-rigid cable if double resonance experiments with two receiving channels are to be performed. Our probe consists of two semi-rigid 50 Ohm cables (Huber+Suhner EZ250 TP M17 and Huber+Suhner EZ 141 TP M17). The NMR LC -resonance circuit is soldered and matched to 50 Ohm by tapping the coil (indicated by the red arrow in Fig. 3.12). The coil was wound manually, e.g., by taking a drill bit as support. We have been using insulated silver wire or tinned copper wire. Coil diameters ranged between 500 μm and 2 mm. With 3 to 6 turns the length of the coils was typically 1 to 2 mm. Tuning capacities of 1 to 10 pF were used giving resonance frequencies between 200 and 700 MHz.

We use a linear stage to adjust the z position of our sample. The accuracy of the positioning is better than 100 μm . This is sufficient even for an accurate positioning of microcoils [30] and has been exploited in position dependent linewidth measurements, cf. section 5.1.

Additionally, the probe is equipped with two pick-up-coils that measure the time derivative of the horizontal and vertical components of the magnetic field as well as two non-magnetic heating resistors and a Philips KTY81 temperature sensor.

Clearly, the matching of the probe is crucial for optimal SNR. While in static fields both tuning and matching are achieved *inside* the magnet with variable elements (e.g., with variable tuning and matching capacitor) spatial limitations do not allow for such variable elements in our probe that additionally has to withstand high electrical powers. However, we find that once the probe is matched outside the magnet, good matching is

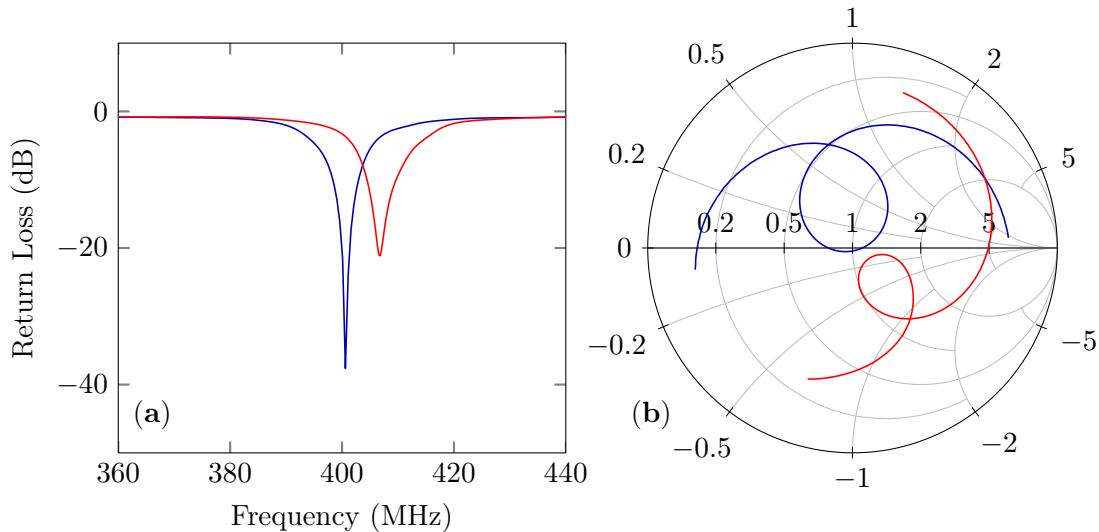


Figure 3.13.: (a) Return loss spectrum of the resonance circuit shown in Fig. 3.12 outside (blue curve) and inside the magnet. The resonance frequency is shifted from 400.6 MHz outside to 406.7 MHz inside the magnet. The measured 7 dB isolated quality factor [31] was 65 outside the magnet and 57.7 inside. Also from (a) one can determine the cable losses between network analyzer and circuit to amount to 0.8 dB/2. The Smith chart (normalized to 50 Ohms) (b) of the same two curves further illustrates the 50 Ohm matching. The normalized radial distance to the center gives the (sufficiently small) voltage reflection coefficient Γ defined by (3.1). For (b) the data points between 391 and 411 MHz (blue curve) and those between 396 and 416 MHz (red curve) have been taken into account.

preserved also inside the magnet. This is illustrated in Fig. 3.13 where we show a return loss spectrum and a Smith chart of the impedance as measured outside (blue curve) and inside (red curve) the magnet. While the matching is nearly perfect outside the magnet (return loss -37.6 dB at resonance), it is still accurate enough inside (return loss -21.1 dB or $|\Gamma| < 0.15$).

3.4. Performance

Since NMR is an intrinsically insensitive method, it is important to demonstrate that the apparatus has optimal sensitivity. In this section we will therefore compare signal- and noise levels as measured on the level of the receiver with the theoretically expected ones. We will discuss the signal-to-noise ratio of the NMR experiment based on the principle of reciprocity as demonstrated by Hoult and Richards in [32]. The NMR receiver has been reviewed by Hoult in [33].

Simplified, the principle of reciprocity states that the B_1 field generated per unit current in the coil not only describes the efficiency of the transmitter, but also that of the receiver (i.e., if a small current produces a strong B_1 field at a given point, then a precessing magnetic moment will induce a correspondingly large voltage). In essence this approach relates the nutation experiment to the sensitivity of the tank circuit.

The overall sensitivity of the apparatus of course is less, since the signal-to-noise ratio is degraded, e.g., by the preamplifier. Here, we thus follow an example given in Pozar's book on microwave engineering [28]: From the thermal noise of the coil we derive the noise power at the receiver.

The signal power at the receiver can then be computed from Curie's law and the principle of reciprocity, the signal power at the receiver being given by the gain and losses of the apparatus. In our treatment we neglect losses of noise and signal power due to impedance mismatches. We also note that the Q -factor of the tank circuit only indirectly enters the equations via the resistance of the coil: For given ω and L a high value of $Q = \omega L/r$ is associated with a low coil resistance and correspondingly the signal power for a given induced voltage V^2/r is higher. Thus an increase of a factor of 2 in the Q value leads to an increase of a factor of two in the signal power or a factor of $\sqrt{2}$ in the signal voltage across a given load. Therefore, the measured signal voltage scales with \sqrt{Q} while the noise power at the resonance frequency is independent of Q (However, the tank circuit is a filter and thus the measured noise power at off-resonant frequencies will be lower, cf. Fig. 3.7) .

3.4.1. Noise

In an ideal system, the measured noise is set only by the thermal Johnson noise, explained by Nyquist [34]. The noise is generated in the resistance of the coil of the NMR tank circuit. Depending on temperature T , bandwidth Δf and resistance of the coil R (typically 1 Ohm) the noise voltage across a resistor R is given by

$$V_n = \sqrt{4k_B T \Delta f R}. \quad (3.2)$$

The maximum noise power that is available to a load R_L is obtained if the load resistance is also given by $R_L = R$. The power into the load then is

$$P_n = I^2 R = \left(\frac{V_n}{2R} \right)^2 R = \frac{V_n^2}{4R} = k_B T \Delta f, \quad (3.3)$$

i.e., it is independent of the coil resistance. In a next step the coil's impedance is transformed to power match the transmitter. Typically, this is done with capacitors and if the leads are sufficiently short the transformation can be considered as lossless.

Now if the preamplifier had an input impedance of 50 Ohm real, the input resistance alone would contribute another 3 dB to the noise level, i.e., the noise figure would have a poor value of greater than 3 dB. The 50 Ohm are therefore transformed to an impedance much greater than 50 Ohm prior to amplification (~ 1 kOhm), i.e., the amplifier is noise matched. Subsequently the noise power is amplified by the gain of the preamp.

The output noise power can be computed using noise temperatures (see e.g. Pozar)¹² From Fig. 3.6, the first preamp has a gain of 33.6 dB or $G = 2291$, the noise figure is

¹²Since our sample is at the same temperature as the preamplifier, the noise power can as well be computed to be $k_B T \Delta f G L$. This is not true, however, if the sample is, e.g., at liquid nitrogen temperature.

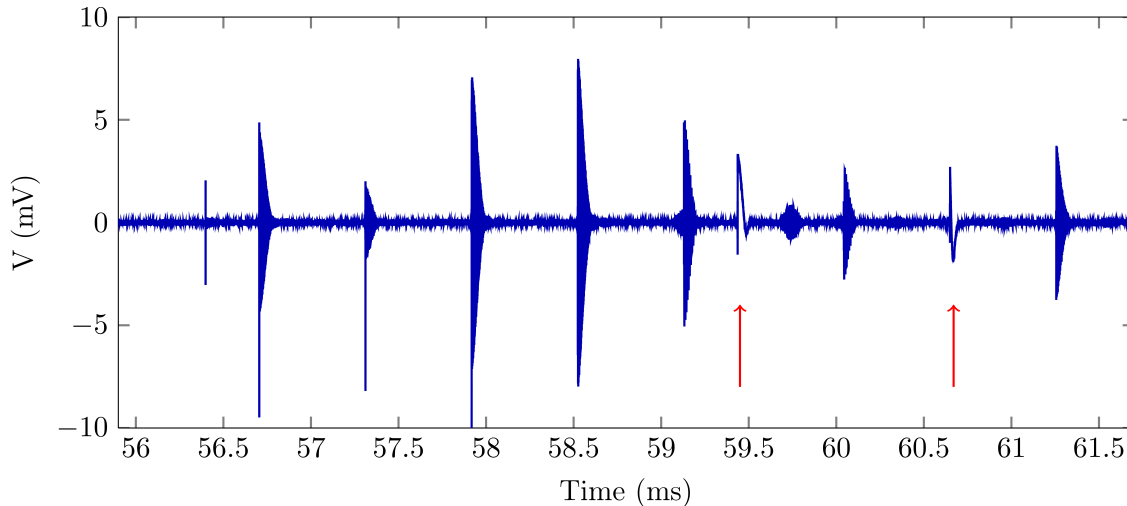


Figure 3.14.: NMR signals of ^1H at room temperature obtained with a Carr-Purcell sequence with one $\pi/2$ pulse (e.g., shortly after 59 ms) and four refocussing π pulses. The sample is H_2O with GdCl_3 to shorten T_1 . The carrier frequency was 407.4 MHz corresponding to 9.6 Tesla. From the data shown here, the noise voltage V_{no} is calculated as the standard deviation of the values between 55.9 ms and 61.3 ms. The used π -pulses have quite correct length as can be seen from the small signal with the small resonance offset (indicated with red arrows) as well as the strong echo signal. The maximum voltage measured corresponds to 8 mV. The spikes due to the RF switches (seen at times before 59 ms) have been removed at times after 59 ms for clarity.

1.3 dB or $F = 1.35$. Then, the equivalent noise temperature T_e of the system (being itself at temperature T_0) is

$$T_e = (F - 1)T_0 = (0.35)290 \text{ K} = 101.5 \text{ K}. \quad (3.4)$$

The two switches following the amplifier cause 1.2 dB losses each, along with cable losses we can estimate losses with -3 dB or $L = 0.50$. For a coil temperature of $T = 290$ K and a bandwidth of 7 MHz (cf. Fig 3.13) the output noise power P_{no} is given as

$$P_{no} = k_B(T + T_e)\Delta fGL = 43 \text{ pW} = \frac{(47 \mu\text{V})^2}{50 \text{ Ohm}}. \quad (3.5)$$

Experimentally, the observed noise level is measured as the standard deviation of the voltages of a recorded signal as the one shown in Fig. 3.14. For this signal, the noise level, determined between 55.9 ms and 56.3 ms, corresponds to $58 \mu\text{V}$, i.e. the noise voltage is 23 % above the expected level or the noise power is 51 % or 1.8 dB above the expected level.

The source of the additional noise is the signal analyzer itself, for its internal noise level of typically -140 dBm/Hz is precisely 34 dB above the thermal level at room temperature. The new preamp, due to its higher gain, reduces this problem, so that the noise performance may become acceptable at room temperature, but for future low temperature experiments a higher gain prior to the signal analyzer needs to be established. The experiments described

here indicate that the cheapest solution would be to use both preamplifiers with a 16 dB attenuator in between, cf. section 3.2.3.

In the next section we will turn our attention to the efficiency of the NMR circuit, i.e., we will compare the experimental “nutation” data with the theoretically expected one.

3.4.2. Excitation

For many NMR experiments in pulsed fields, it is important to have a good estimate of the $\pi/2$ pulse duration prior to the first experiment, especially, if another magnet to calibrate the circuit is not available. The theoretical length of the $\pi/2$ pulse is readily derived using the fact that the *peak* energy stored in the inductor equals the peak energy stored in the magnetic field produced by the coil. As discussed by Slichter [9],

$$\frac{1}{2}Li^2 = \frac{1}{2\mu_0}B_{\text{RF}}^2 V. \quad (3.6)$$

Herein, i is the amplitude of the current and B_{RF} is the amplitude of the *linearly* polarized field, cf. Eq. (2.6). Note that we have assumed the field B_{RF} to be uniform across the volume V .

Since the current is sinusoidal the average power dissipated in the circuit is

$$P = \left(\frac{i}{\sqrt{2}}\right)^2 r = \frac{i^2}{2}r \quad (3.7)$$

where r is the resistance of the coil. The average dissipated power equals the power of the transmitter as soon as the resonance circuit is in steady-state. Substituting i^2 from Eq. (3.7) into Eq. (3.6) we obtain

$$L\frac{2P}{r} = \frac{1}{\mu_0}B_{\text{RF}}^2 V. \quad (3.8)$$

Solving for the circularly polarized $B_1 = \frac{1}{2}B_{\text{RF}}$ yields

$$B_1 = \frac{1}{2}B_{\text{RF}} = \frac{1}{2}\sqrt{\frac{\mu_0 L 2P}{rV}} = \frac{1}{2}\sqrt{\frac{2\mu_0 PQ}{\omega_0 V}} = \sqrt{\frac{\mu_0 QP}{2\omega_0 V}} \quad (3.9)$$

where we have used the relation $Q = \omega_0 L/r$. In practice the field will be distributed across a volume V which is larger than the coil volume V_c to an extent that depends on the coil geometry.

Neglecting a possible resonance offset, B_1 is applied along an axis which is fixed in the Larmor rotating frame. Thus in the rotating frame, the magnetization precesses about B_1 with frequency

$$\omega_1 = \gamma B_1, \quad (3.10)$$

and the length of a $\pi/2$ pulse is given by

$$\tau_{\pi/2} = \frac{\pi}{2\omega_1} = \frac{\pi}{2\gamma B_1}. \quad (3.11)$$

In the exemplary data shown in Fig. 3.14, we have been using pulse length of 200 ns and 400 ns for the $\pi/2$ and π pulses, respectively. It can be seen from the small amplitude of the on-resonant FIDs following the π pulses at 59.5 ms and 60.5 ms, that a perfect π pulse is approximated reasonably well on resonance.

The RF power level of the signal generator was set to 6 dBm corresponding to an RF power of 56.9 dBm or 490 W, cf. Fig. 3.5. With a measured Q of 51 and a Larmor frequency of $2\pi 407.4$ MHz, the calculated B_1 field in a cylindrical coil of 2.5 mm length and 1.1 mm diameter is 51 mT. From Eq. (3.11) the $\pi/2$ pulse duration hence is 115 ns.

The discrepancy of a factor of two compared to the experimental value is rather expected if one takes into account that the B_1 field of the coil (four turns) is rather inhomogeneous and that the legs contribute significantly to the coil volume V .

3.4.3. Signal

The equilibrium magnetization of the sample is given by Curie's law. If we take half of the sample volume to be filled with water, then the magnetization of the hydrogen spins $I = 1/2$ at 9.6 Tesla and 290 K equals

$$M_0 = n \frac{\gamma_n^2 \hbar^2 B_0 I(I+1)}{3k_B T} \approx 16 \times 10^{-3} \text{ A/m.} \quad (3.12)$$

Thus, the estimated voltage induced in the coil with $N = 4$ turns is

$$V = \mu_0 M N A \omega_0 = 48.5 \text{ } \mu\text{V.} \quad (3.13)$$

Now we know from the excitation that we lose a factor of four in power, so by reciprocity we lose also a factor of $\xi = 2$ in the signal voltage, i.e., we have

$$V_{\text{ind}} = V/\xi = 24.5 \text{ } \mu\text{V.} \quad (3.14)$$

In order to convert this to a signal power we need to know the resistance of the coil. The resistance can be obtained from the quality factor if the inductance is known, and the latter can be estimated from the resonance frequency, if the capacitance is known. From our capacitance of 11 pF we determine an inductance of

$$L = \frac{1}{\omega^2 C} = 14 \text{ nH.} \quad (3.15)$$

Thus, the resistance of the coil is $r = \frac{\omega L}{Q} = 0.7 \text{ Ohm}$. The signal power after the preamp hence is

$$P_{so} = \frac{V_{\text{ind}}^2}{r} GL = \frac{(7 \text{ mV})^2}{50 \text{ Ohm}} \quad (3.16)$$

in agreement with the observed voltages of 5 to 8 mV in Fig. 3.14.¹³

¹³Note, however, that we have neglected that the time between pulses is only $\sim T_1$, i.e., we might see only part of the full equilibrium magnetization. The interplay between T_1 , offset and signal intensity will be elucidated in chapter 5.

3.5. Discussion

The probe developed within this thesis is well understood in terms of sensitivity and, due to the linear stage, is also equipped for future NMR experiments using microcoils.

The custom-built spectrometer described in this chapter has proven to be a valuable and reliable tool in the pulsed field laboratory. Both noise and signal levels of the apparatus can be derived from first principles with reasonable accuracy. Clearly, for future designs one would require that the various PXI components share one local oscillator, so that they are phase locked to each other. With preamp 1 the noise voltage is 25 % above its expected level. Even though the recently purchased preamp 2 will reduce this voltage excess due to its higher gain, a more sensitive receiver seems desirable for future experiments.

4. NMR and the time dependence of pulsed magnetic fields

The standard NMR experiment is performed in a static magnetic field.¹ If it were varying strongly with time, this would pose a serious problem for all kinds of applications. Therefore, pulsed magnets do not seem to provide a friendly environment for NMR.

In a constant magnetic field B the nuclear precession proceeds at a constant rate $\omega = \gamma B$, where ω is the Larmor frequency. This leads to a phase that is linear in time, $\phi(t) = \omega t$.

In a time-dependent field $B(t)$ the phase of the precessing magnetization is given by the time-integral of the field,

$$\phi(t) \sim \gamma \int B(t) dt. \quad (4.1)$$

The fundamental question for a pulsed magnet, apart from a sufficiently high reproducibility of the field pulse, is the actual time dependence of the field. If it is not “good” or smooth enough, we cannot discern changes in the phase due to interesting spin interactions from those due to unpredictable changes of the field. In the worst case this could cause NMR to be useless in pulsed fields.

In this chapter we investigate the intrinsic time dependence of the field using the most simple assumption of a quadratic or cubic local model for $B(t)$ in the vicinity of the field maximum to fit the time dependence of the field to the experimental phase data. To our surprise we find that the magnetic field can be determined with sub-ppm accuracy over the entire time interval during which we can observe NMR signals. This implies that the time dependence can in fact be removed from the data making signal-averaging possible as if the field were constant and stable with sub-ppm precision during that time interval. Within this thesis, the work described in the current chapter forms a central achievement for NMR in pulsed magnets. The work was published in the *Journal of Magnetic Resonance* [5], recently, and was chosen as cover article for the May issue in 2011.

4.1. Experimental

Our very first experiments aimed at testing the spectrometer, in particular in connection with the control computer of the capacitor bank that stores the energy for the magnetic field pulses, and searching for test resonances (NMR experiments on ^1H and ^{63}Cu at up to

¹Small fluctuations on the ppb level are taken into account using a lock channel.

33 Tesla with a small magnet coil were performed on a metal organic framework material and Cu metal, respectively).

After the completion of those experiments we moved to the LP magnet that had been built for long pulses, cf. Fig. 3.2. We started again searching for the ^1H NMR at low fields, which means small amounts of energy are deposited per field pulse in the magnet coil so that various pulses can be initiated before a substantial heating occurs. Once the resonances were found, we were able to predict the maximum field based on the capacitor bank's charging voltage with a high enough accuracy (about 0.5%) to reliably observe NMR signals during every field pulse. Subsequently, we began a more detailed study of the field's time dependence also at higher fields. Later, we moved to the magnet coil KS3 where the same procedure for measuring $B(t)$ was repeated up to the maximum field strength of 62 Tesla.

In this chapter we describe experiments at 7.77 and 44 Tesla performed in the LP coil as well as an experiment at 62 Tesla performed in the KS3 coil. The shape of the corresponding field pulses can be approximated by simply rescaling the curves shown in Fig. 3.2.

The NMR probe head used for the experiments did not yet have a linear stage for accurate adjustment of the z -position in the magnet coil and cryostat. The sample temperature was measured with a Pt-100 thermometer. However, tuning and matching of the circuit were performed precisely as described in chapter 3. We used ^1H and ^2H NMR for experiments at low (7.77 Tesla) and high fields (44 Tesla and 62.2 Tesla), respectively. While ^2H NMR is not as sensitive as ^1H NMR, its lower gyromagnetic ratio enables us to track a correspondingly larger interval of the magnetic field ΔB within the bandwidth of our setup Δf (i.e., $\Delta f = \gamma\Delta B/2\pi$).

For the experiment at low field (7.77 Tesla) we used a solution of H_2O (2.5 ml) with GdCl_3 (52 mg) so that the ^1H spin lattice relaxation time as measured in static field was about 0.7 ms. For the experiment at higher fields (above 40 Tesla) we used D_2O (2 ml) with 1 g of GdCl_3 giving a ^2H T_1 of 0.5 ms (cf. 2.3). The solution was filled into a glass capillary of 1 mm diameter, which was sealed with glue and inserted into the RF coil. The measured Q values were about 40.

4.2. Estimate of $B(t)$ at low field

First, we report our results obtained at rather low pulsed field, slightly above 7.7 Tesla. A train of 25 identical, equidistant (delay 1 ms) RF pulses (duration $\tau = 0.3 \mu\text{s}$) was derived from a single, stable RF carrier source running at a chosen frequency ω_0 . The 25 excited FIDs of the ^1H magnetization of the liquid test sample ($T_1 \sim 0.7 \text{ms}$) were recorded in-between the RF pulses. After the experiment the receiver trace was dissected at times $t = t_j$, where t_j equals the time at the end of the RF pulse plus $3 \mu\text{s}$, cf. Fig. 4.1 and Fig. 3.11. The resulting set of 25 FIDs was Fourier transformed and the magnitude spectra are plotted as a function of the time $t = t_j$ in Fig. 4.2. The 2nd axis in Fig. 4.2 represents

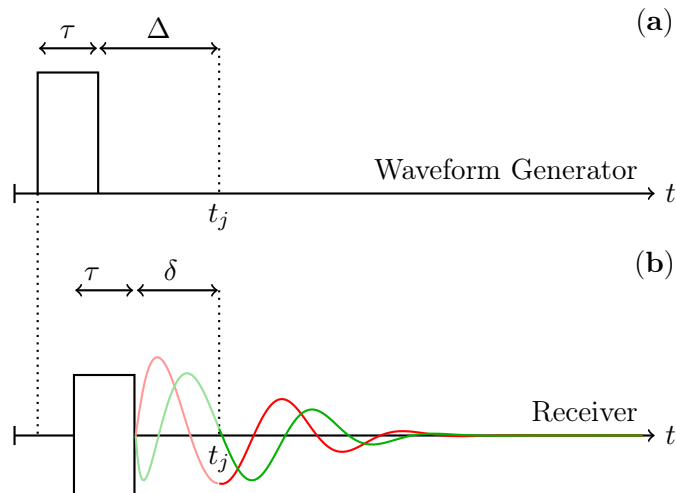


Figure 4.1.: Timing variables used in this chapter. (a) τ , Δ , t_j are defined within the software that controls the waveform generator. After the j -th RF pulse of duration τ we wait the dead time $\Delta = 3 \mu\text{s}$ before the receiver is turned on. (b) Due to delays during transmission and receiving of the FIDs the pulse and the signal appear shifted in time so that the effective dead time is now $\delta < \Delta$. The red and green curve are a sketch of the NMR signal (IQ data)

the frequency or resonance offset $\Delta\omega/2\pi = (\omega - \omega_0)/2\pi$. One notices from Fig. 4.2 that we were able to record spectra with similar intensities after each RF pulse over the entire time interval of about 25 ms during which the magnetic field varied continuously. Also shown in Fig. 4.2 (full red line) is $B_{\text{fit}}(t)$ as determined from the maxima of the spectra in the following way: We describe $B(t)$ with a minimal set of parameters in the vicinity of its maximum ($t \sim t_{\text{max}}$) where we expect a quadratic or cubic dependence on time to hold, i.e.,

$$B_{\text{fit}}(t) = B_{\text{max}} \left(1 - \alpha (t - t_{\text{max}})^2 + \beta (t - t_{\text{max}})^3 \right), \quad (4.2)$$

where α and β are positive constants, and B_{max} is the field maximum that occurs at $t = t_{\text{max}}$.

A nonlinear least-squares fit is performed using Matlab's implementation of the Levenberg-Marquardt algorithm [35, 36] in order to obtain B_{max} , t_{max} , α and β from the maxima of the magnitude spectra. The algorithm returns the coefficient estimates, the residuals, the Jacobian and a covariance matrix for the fitted coefficients. For each parameter the 95% confidence interval as specified in Tab. 6.2 is obtained as $a \pm ts$ where t is derived from Student's t Distribution using the degrees of freedom and the required confidence and s denotes the standard error, i.e. the square root of the given diagonal entry of the covariance matrix. The obtained values are shown in the first row of Tab. 6.2.

Clearly, using the maxima of the (not demodulated) magnitude spectra for the determination of $B(t)$ will give us not more than rough estimates for the parameters in (4.2). The main problem with the above approach is the assignment of a spectral property (given by a

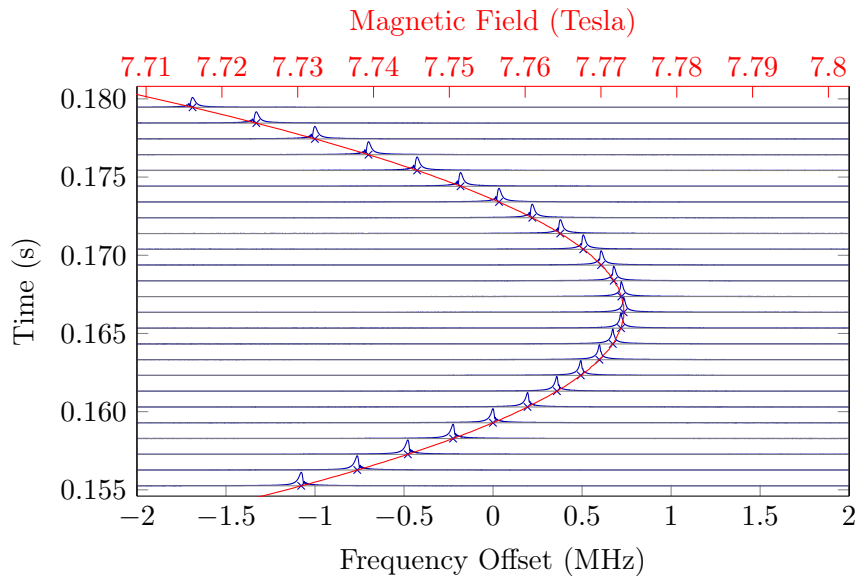


Figure 4.2.: Magnitude Fourier transform spectra of all 25 FIDs vertically offset by the time when acquisition started. The crosses show a projection of the maxima to the baseline of a given spectrum. With the carrier frequency at about 330 MHz each maximum is interpreted as a measure of B at time t_j . The full line shows a fit of the maxima of the spectra to $B_{\text{fit}}(t)$ from Eq. (4.2).

time integral) to a single moment in time. Within the above fitting procedure, the Fourier transform averages the Larmor frequency over the entire FID (exponentially weighted with the inhomogeneous decay rate $1/T_2^*$) and assigns the averaged value to the beginning of the FID. Thereby the field values are slightly overestimated during the rise time and slightly underestimated during the fall time of the magnetic field pulse.

A rather simple approach to correct for this issue is to remove the time dependence from the data (referred to as demodulation, explained in detail below) and determine the field again from the corrected data. However, demodulating the data requires one to know the correct field. In order to solve for this problem, we tried to iterate the demodulation/fitting scheme to find out if the estimated parameters would converge towards a certain value. However, convergence was not observed but rather the algorithm proved unstable and resulted in completely wrong estimates. (Looking back, this is not entirely unexpected since an error in the estimate of the field can shift the data to any frequency causing a correspondingly large error in the next iteration step.)

However, the solution to the problem is straightforward and will be given in the next section.

Coil	Fit	B_{\max} (Tesla)	t_{\max} (s)	α (s ⁻²)	β (s ⁻³)	ϕ_0 (rad)
LP	FT	7.773 012(9)	0.166 403(3)	43.54(2)	46(2)	-
LP	ϕ	7.772 982 3(2)	0.166 441 53(6)	43.5710(4)	41.88(6)	1.66
LP	FT	43.9869(3)	0.172 88(1)	38.8(3)	-	-
KS3	FT	62.164(1)	0.048 446(4)	91(5)	-	-
KS3	ϕ	62.164 67(5)	0.048 460 5(2)	91.6(2)	-	-0.79

Table 4.1.: Results from fitting the maxima of the magnitude spectra, 1st, 3rd and 4th row, to Eq. (4.2), and fitting the experimental time evolution of the phase, 2nd and 5th row, to Eq. (4.4) by varying the parameters of Eq. (4.2). The experiments with the LP coil were performed at 7.77 and 44 Tesla, the experiment in the KS3 magnet was performed at about 62.2 Tesla. The change of $B(t)$ during each FID is not taken into account by the Fourier Transform fitting procedure leading to systematic deviations of α and β from their values as obtained by the phase fitting procedure.

4.3. Time and Phase

We note that the detection yields a set of $j = 1, \dots, N$ complex valued (I/Q) FIDs $G_{\text{exp},j}(t) = I_j(t) + iQ_j(t)$. We can think of each individual FID as

$$G_j(t) = G_{0,j} e^{-(t-t_j)/T_2^*} e^{+i\phi_j(t)}. \quad (4.3)$$

The initial amplitude $G_{0,j}$ is given by the j -th RF pulse (including the probe properties), and the longitudinal magnetization before the pulse (the dependence on the actual frequency $\omega_j = \gamma B(t_j)$ can be neglected). The observed amplitudes of the FIDs are within the limits of our expectations based on the number of resonant nuclei in the sample (cf. section 3.4.3). The apparent decay time of $T_2^* \sim 30 \mu\text{s}$ is shorter than what one estimates from the measured T_1 of 0.7 ms. The FIDs far away from $t = t_{\max}$ are dominated by a modulated phase from the strong time dependence of the field. Near the field maximum, however, the decays remained rather short probably due to the inhomogeneity of the field across our small samples. Recent Carr-Purcell spin-echo experiments (discussed in the following chapter) show clear echoes even at times of up to 2 ms after the initial pulse pointing indeed to inhomogeneous broadening. Note, that the maximum field cannot be predicted from one field pulse to another with a high accuracy. Together with the low repetition of field pulses, the investigation of the field distribution as a function of probe position is a lengthy task. First experiments addressing this issue will be described in the following chapter. Here, we focus on the time dependence of the magnetic field, that also contributes to the linewidths due to the modulation of the signal's average phase.

The (time-dependent) phase $\phi_j(t)$ of the j -th FID in the rotating frame (ω_0) can be

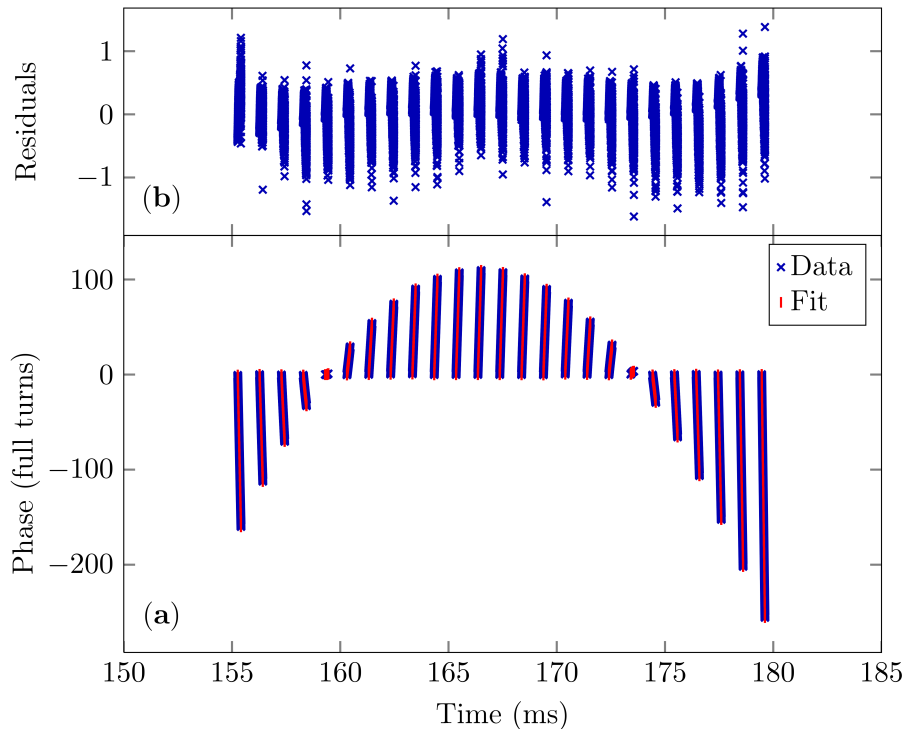


Figure 4.3.: (a) Experimental phase (blue crosses) and fitted values (red vertical bars) for the 25 FIDs measured at 7.77 Tesla. As expected the phase decreases if the resonance offset is negative and increases if it is positive. In (b) we show the difference between experimental and fitted values. Even if the magnetization performs 100 cycles, the deviations between fit and experimental data are not much larger than one turn.

written as, cf. Fig. 4.1,

$$\phi_j(t) = \phi_0 + \phi_{\tau,j} + \int_{t_j-\delta}^t [\gamma B(t') - \omega_0] dt'. \quad (4.4)$$

Strictly speaking, this is only true if transmitter and receiver are phase-locked. A trivial way to achieve such a phase lock is to use the same local oscillator for both transmitter and receiver. Unfortunately, this is not possible with the PXI components of our spectrometer described in the previous chapter (the common clock synchronizes the frequencies but not the phases). In our setup, the phase lag between transmitter and receiver is therefore essentially random. However, the phase lag between transmitter and receiver varies only slowly in time (changes are of the order of π in 100 ms). Thus, we can take ϕ_0 to be constant for a set of FIDs taken during a single magnetic field pulse.

4.3.1. Offset excitation

The second term in Eq. (4.4) describes the action of the very short RF pulse during which we can assume the field to be constant ($B(t) = B(t_j)$). $\phi_{\tau,j}$ follows from an effective Hamiltonian

$$\mathcal{H}_{\tau,j} = \hbar\Delta\omega_j I_z + \hbar\omega_{\text{RF}} I_x, \quad (4.5)$$

cf. section 2.1. For the Hamiltonian given in Eq. (4.5), $\phi_{\tau,j}$ is calculated as follows (see also [12]): The on-resonant nutation frequency ω_{RF} can be determined simply from $\omega_{\text{RF}} = \gamma B_1$ or from the flip angle φ of the pulse of duration τ , i.e.,

$$\omega_{\text{RF}} = \varphi/\tau. \quad (4.6)$$

For an off-resonant pulse, the effective field B_{eff} , as defined in Fig. 2.1 is tilted out of the xy plane, the angle between B_{eff} and B_1 is given as

$$\theta_j = \arctan\left(\frac{\Delta\omega_j}{\omega_{\text{RF}}}\right), \quad (4.7)$$

and the amplitude of the effective field is

$$B_{\text{eff},j} = \sqrt{B_1^2 + \Delta\omega_j^2/\gamma^2}. \quad (4.8)$$

Of course, the magnetization precesses about the effective field with frequency $\omega_{\text{eff},j} = \gamma B_{\text{eff},j}$ and hence the flip angle is

$$\Phi_j = \omega_{\text{eff}}\tau \quad (4.9)$$

Thus a pulse with resonance offset $\Delta\omega_j$ will lead to a rotation of Φ about the effective field $\mathbf{B}_{\text{eff},j} \propto (\cos\theta_j, 0, \sin\theta_j)$. For any initial magnetization \mathbf{M}_j , the orientation of the magnetization after the pulse can be obtained as

$$\mathbf{M}'_j = \mathcal{R}_j \mathbf{M}_j = \mathcal{R}_{y''}(-(\pi/2 - \theta)) \mathcal{R}_{z'}(\Phi) \mathcal{R}_y(\pi/2 - \theta) \mathbf{M}_j \quad (4.10)$$

where $\mathcal{R}_y, \mathcal{R}_z$ are the basic rotations about the given axis, i.e.,²

$$\mathcal{R} = \begin{pmatrix} \cos^2\theta + \sin^2\theta \cos\Phi & -\sin\theta \sin\Phi & \cos\theta \sin\theta(\cos\Phi - 1) \\ \sin\theta \sin\Phi & \cos\Phi & \cos\theta \sin\Phi \\ \cos\theta \sin\theta(\cos\Phi - 1) & -\cos\theta \sin\Phi & \cos^2\theta \cos\Phi + \sin^2\theta \end{pmatrix} \quad (4.11)$$

is the rotation matrix for a rotation of Φ about B_{eff} .

If the initial magnetization lies along z , i.e., $\mathbf{M} = (0, 0, M_z)$, then after the pulse we have

$$\mathbf{M}' = \mathcal{R} \mathbf{M} = M_z \begin{pmatrix} \cos\theta \sin\theta(\cos\Phi - 1) \\ \cos\theta \sin\Phi \\ \cos^2\theta \cos\Phi + \sin^2\theta \end{pmatrix}. \quad (4.12)$$

From this expression we can determine the phase of the transversal magnetization due to the excitation as

$$\phi_{\tau,j} = \text{atan2}(y, x) = \text{atan2}(\cos\theta_j \sin\Phi_j, \cos\theta_j \sin\theta_j(\cos\Phi_j - 1)), \quad (4.13)$$

the definition of the atan2 function will be given below.

²Using the zyz convention, the Euler angles of the rotation are $\alpha = \pi/2 - \theta$, $\beta = \Phi$ and $\gamma = -(\pi/2 - \theta)$. The index j is omitted for clarity. A detailed description can be found in [12].

4.3.2. Offset precession

For the evolution of the phase after the RF pulse the time-dependent field occurs in the integral of (4.4). Note that the time t_j only has a precise meaning within the pulse-generation sequence as it does not include phase changes during transmitting and receiving, cf. Fig. 4.1. At a given carrier frequency (ω_0), this difference in time is set by the hardware and gives rise to the phase difference ϕ_0 in (4.4). However, since each FID $G_j(t)$ in (4.3) has a varying frequency offset, it will acquire another phase difference during the time interval δ between the end of the pulse and t_j , cf. Fig. 4.1. This phase lag is taken into account by using $t_j - \delta$ as the lower bound for the integral in (4.4).

From our experimental data $G_{\text{exp},j}(t) = I_j(t) + iQ_j(t)$ we can obtain the time-dependent phase of each FID using the atan2 function.³ The atan2 is a generalization of the arctan function that maps a complex number to the interval $(-\pi, \pi]$, i.e., the full circle. The atan2 function is implemented in both Matlab and Python and can be called via the command `angle(z)`, where $z = x + iy$ is a complex number.

Consider now as an example an FID with a fixed, positive resonance offset $\Delta\omega$ and amplitude $f(t)$:

$$F(t) = f(t) \exp(i(\Delta\omega t + \phi_0)) \quad (4.15)$$

According to our above definition, the phase of the FID is

$$\phi(t) = \phi_0 + \Delta\omega t. \quad (4.16)$$

Hence, the phase is a continuous function of time, whereas the atan2 is a sawtooth-like, discontinuous function. In order to compare our experimentally obtained values with the theoretical ones predicted from Eq. (4.4), we need to “unwrap” the output of the atan2 function. This is readily achieved by iterating over the experimental phase and minimizing the difference between adjacent data points through the addition or subtraction of $n2\pi$, where n is an integer. Again, both Python and Matlab provide a corresponding unwrap function.

The experimental phase information is therefore obtained as

$$\phi_{\text{exp},j}(t) = \text{unwrap}(\text{angle}(I_j(t) + iQ_j(t))) \quad (4.17)$$

³The atan2 function is defined as

$$\text{atan2}(Q, I) = \begin{cases} \text{atan}(Q/I) & I > 0 \\ \text{arctan}(Q/I) + \pi & I < 0, Q \geq 0 \\ \text{arctan}(Q/I) - \pi & I < 0, Q < 0 \\ \pi/2 & I = 0, Q > 0 \\ -\pi/2 & I = 0, Q < 0 \\ 0 & I = Q = 0 \end{cases}. \quad (4.14)$$

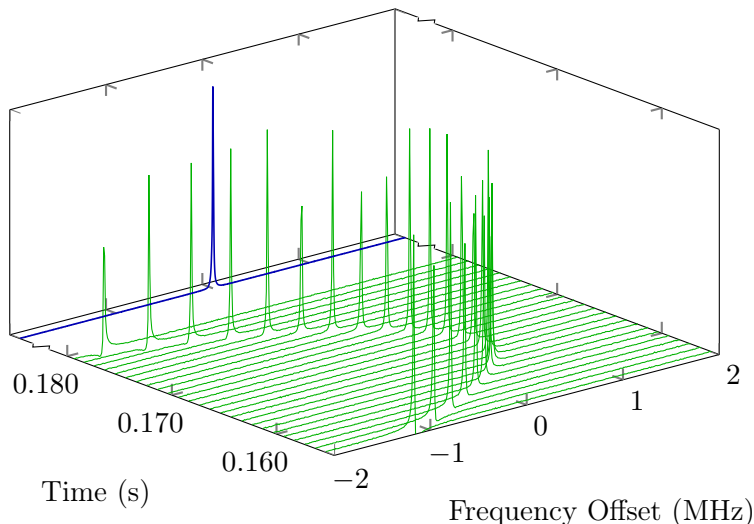


Figure 4.4.: 7.77 Tesla experiment; real parts (green lines) of Fourier transform spectra of the 25 FIDs demodulated using (4.19) plotted as a function of the time t_j . Note that the adjustable phase ϕ_0 in (4.4) is the same for all spectra. The blue line shows the real part of the averaged spectrum, i.e. the Fourier transform of (4.18).

Of course the unwrapping becomes error-prone as soon as the phase begins to fluctuate due to thermal noise. Likewise, a problem occurs if the resonance offset approaches the bandwidth at which the data were taken.

The experimental phases of our 25 FIDs, determined during the first 150 μs (where the signal amplitude is clearly above the noise), are shown in Fig. 4.3.

4.3.3. Fit results

Now we again use (4.2) with the parameters determined earlier as starting values for fitting $\phi_j(t)$ to $\phi_{\text{exp},j}(t)$ using the same algorithm as described above. We used a $\pi/2$ pulse and varied ϕ_0 and δ manually minimizing the deviation of $\phi_j(t_j)$ from $\phi_{\text{exp},j}(t_j)$, see Tab. 6.2. As expected, this fitting protocol results in more accurate estimates of the coefficients in (4.2), the main result being a decrease of the error in B_{max} down to 0.03 ppm.

Confer the second row of Tab. 6.2 for all estimates. Such a high precision suggests that we can use (4.2) with the parameters from Tab. 6.2 and demodulate and phase-correct all FIDs at once.

4.3.4. Demodulation

We note that we can use (4.4) in order to remove the effect of the time-dependent resonance frequency from $\phi_{\text{exp},j}(t)$ and the thus transformed FIDs should all be identical (no dependence on j), i.e.,

$$G_{\text{exp}}(t) = \frac{1}{N} \sum_{j=1}^N G_{\text{exp},j}(t) \exp(-i\phi_j(t)) \sim G_{\text{exp},k}(t) \exp(-i\phi_k(t)) \quad (4.18)$$

for any k in $1, \dots, N$.

In order to plot the FIDs as a function of the field's deviation from $B(t_j)$ we simply modify our experimentally obtained FIDs according to

$$\tilde{G}_{\text{exp},j}(t) = G_{\text{exp},j}(t) \exp \left(-i\phi_j(t_j) - i\gamma \int_{t_j}^t [B(t') - B(t_j)] dt' \right). \quad (4.19)$$

The real parts of the Fourier transforms following from (4.19) (with an additional 5 kHz exponential line broadening) are displayed in Fig. 4.4. All frequency modulations have disappeared, the linewidths are the same and the spectra appear to be almost perfectly in phase (the small phase drift is attributed to the phase drift between signal generator and signal analyzer).

Also shown in Fig. 4.4 (the blue spectrum to the far left) is the Fourier transform of $G_{\text{exp}}(t)$ as defined in Eq. (4.18). Obviously, this spectrum is very similar to the individual ones and has nearly the same intensity. We find an increase in the experimental signal-to-noise ratio of 4.7, close to the theoretical value of $\sqrt{25}$.

We think these are very encouraging results. While it was shown earlier that a single FID could be demodulated successfully at low pulsed-field strength [37], we here demodulate *and* phase-correct a set of 25 FIDs with two adjustable parameters ϕ_0 and δ . This means that by monitoring the field with a reference sample one can obtain highly precise knowledge of the field over a large period of time and one is able to predict all initial signal phases. By simultaneously measuring a 2nd signal (with a double-resonance probe) one could perform signal averaging and shift measurements with high precision. In essence, the presented results show that one can remove the time dependence of the field so that all signals appear to be taken in a magnet at a stable, constant field.

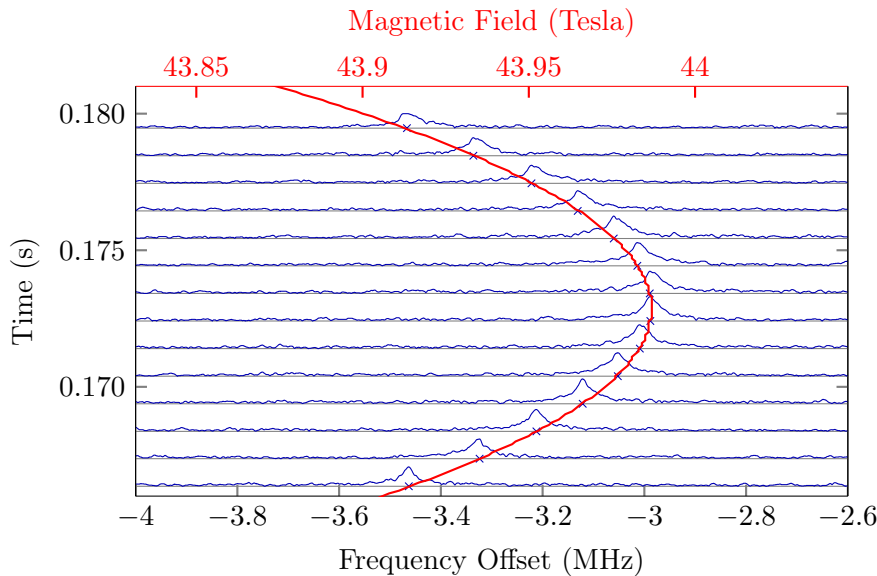


Figure 4.5.: Experiment at 44 Tesla; The magnitude spectra (blue lines) of 14 FIDs are shifted vertically by the time when acquisition started. With the carrier frequency of 290.48 MHz each spectrum is taken again as a measure of the applied magnetic field at the time of the corresponding RF pulse (cf. Fig. 4.2). The (red) thick line indicates a fit according to Eq. (4.2). Note that all spectra show a rather large negative resonance offset, i.e., the field was about 1 % lower than expected prior to the pulse. While the sinc function, which approximates the excitation spectrum of the short RF pulses, crosses zero at -2 MHz, its magnitude increases to about 20 % of its maximum value at the offset of -3 MHz (Likewise, the amplitude of the signal can be computed from Eq. (4.12) below, leading to the same result).

4.4. Field measurement at 44 Tesla

Now, the obvious question arises whether such a procedure also works at much higher fields that cannot be reached with ordinary magnets. For completeness, we show in Fig. 4.5 an experiment performed in the LP coil at 44 Tesla. As can be seen from the rather large resonance offset, the field was lower (by 1 %) than estimated prior to the field pulse. While the large offset demonstrates the high bandwidth of the spectrometer, the efficiency of the rf pulses is reduced by a factor of five leading to equally lower signal intensities. Furthermore, the large resonance offset of more than 3 MHz at a sample rate of 10 MHz causes the phase to change significantly for two adjacent data points. Therefore, the unwrapping procedure described in the previous section fails already shortly after the beginning of the FID.

The large resonance offset of the data shown in Fig. 4.5 hampers an analysis in terms of the signal's phase. Since it took already three shots to obtain the discussed set of signals, and since each such shot takes a full day for cooling the coil, we decided not to try a further optimization of our data. Instead, we wanted to pursue the question whether or not the phase analysis described for the low field experiment would also be possible in the KS3 magnet. This magnet would also offer both higher maximum field and shorter cooling

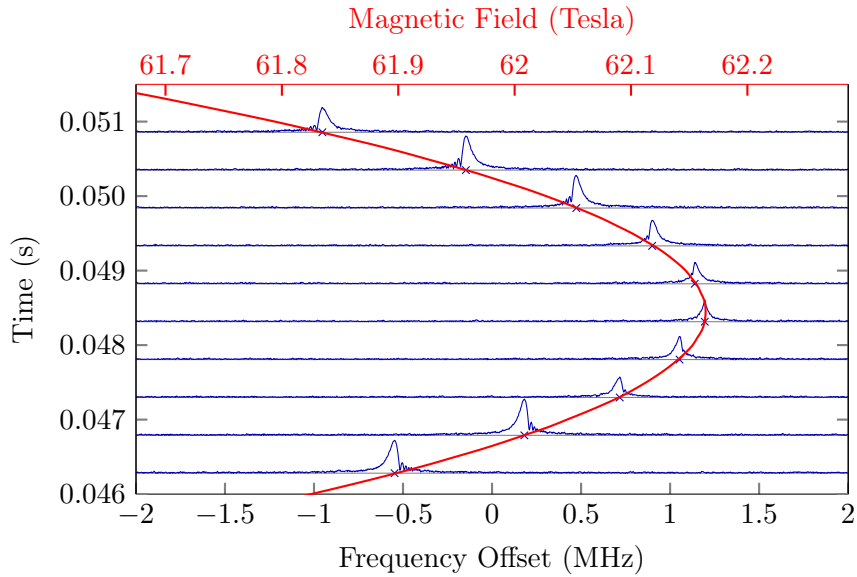


Figure 4.6.: Magnitude Fourier transform spectra of all 10 ^2H FIDs obtained during a single field pulse in the KS3 magnet at 62 Tesla vertically offset by the time when acquisition started. The crosses show a projection of the maxima to the baseline of a given spectrum. Due to the stronger time dependence frequency-modulation effects are clearly visible in the spectra away from the field maximum. The full red line shows a fit of the maxima of the spectra to $B_{\text{fit}}(t)$ from Eq. (4.2), see text.

time. The shorter cooling time is especially helpful since it enables one to perform several experiments in a row, increasing the probability that data with a small resonance offset in the vicinity of the field maximum will be available.

4.5. Field measurement at 62 Tesla

Indeed similar results as those at 7.77 Tesla were found. One experiment at 62 Tesla is described in more detail below.

Here, a train of 10 RF pulses ($\tau = 0.5 \mu\text{s}$, delay 0.5 ms) derived from the RF carrier running at about 405.1 MHz was used to excite ^2H NMR FIDs of a D_2O sample in magnet KS3. The signals were recorded in-between pulses and the receiver trace was again dissected at times t_j as described earlier. The magnitude spectra, presented similar to Fig. 4.2, can be found in Fig. 4.6.

The spectra taken on the steeper slope of the field, i.e., away from the field maximum, clearly show modulation features from the time-dependent field during signal decay (note that the duration of the field pulse in magnet KS3 is shorter, cf. Fig. 3.2, so that the modulation is easier to see in comparison to Fig. 4.2). We also observe a somewhat stronger variation of the signal intensities in Fig. 4.6 compared to Fig. 4.2. The reason for the variation is probably the relatively longer T_1 of the sample compared to the RF pulse distance. The overall lower signal-to-noise ratio is due to a smaller number of ^2H

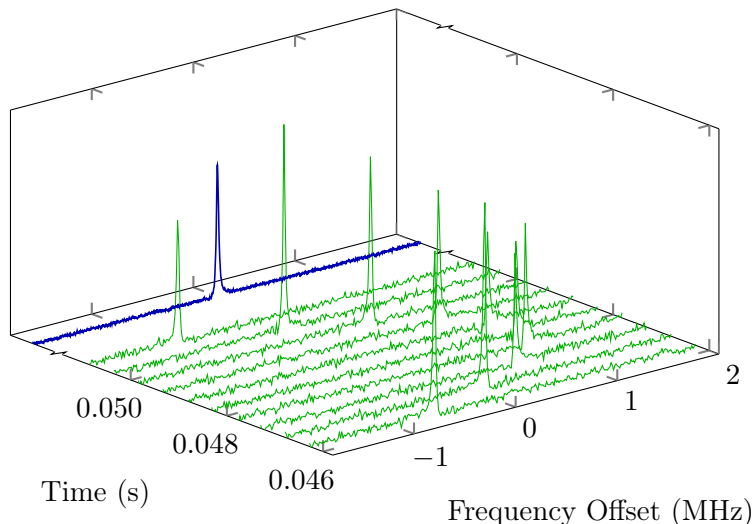


Figure 4.7.: 62 Tesla experiment; real parts (green lines) of Fourier transform spectra of the 10 FIDs demodulated using (4.19) plotted as a function of the time t_j . Note that the adjustable phase ϕ_0 in (4.4) is the same for all spectra. The blue line is again the real part of the averaged spectrum, i.e. the Fourier transform of (4.18)). The improvement in the signal-to-noise ratio is clearly visible.

in the sample. Also shown in Fig. 4.6 is $B(t)$ as derived from the peak frequencies of the magnitude spectra and their fit to the magnetic field time dependence according to (4.2). The fitted parameters are displayed in Tab. 6.2. Note that the cubic term is absent, i.e. $\beta = 0$, since we stay closer to the field maximum (the data spread across a smaller bandwidth).

From our 10 experimental FIDs, $G_{\text{exp},j}(t)$, we again calculate a set of experimental phases $\phi_{\text{exp},j}(t)$ and their evolution with time. We then use the just described parameters that are displayed in the 4th row of Tab. 6.2 and fit $\phi_j(t)$ from (4.4) to $\phi_{\text{exp},j}(t)$ by varying the parameters of (4.2) in order to obtain new values for the parameters that describe the time dependence of the field more accurately. They are presented in the 5th row of Tab. 6.2. Also shown is the manually fitted overall phase ϕ_0 and dead-time δ (in fact, since there was no time to measure the flip angle of the pulse precisely at such high field, we determined it with the fit, as well, and found 2.1 rad instead of the estimated 1.57 rad). Remarkably, the precision of the fit to the magnetic field is very good, albeit not as good as that at low field where 25 FIDs were available. Since probe and spectrometer hardware remained essentially the same when moving over to the KS3 magnet (only a small difference in frequency), we are not surprised to find the same dead-time δ . The change in ϕ_0 is expected since the RF signal generator is turned on long (typically one minute) before the actual field pulse and has a random phase with respect to the signal analyzer, cf. section 4.3. However, the phase is stable enough for the duration of most experiments.

In a next step, we use the determined $B_{\text{fit}}(t)$ and demodulate and phase-correct the experimental FIDs $G_{\text{exp},j}(t)$ according to (4.19). The result, the real parts of the Fourier

transforms of the individual spectra (additional exponential broadening of 10 kHz) as a function of field are displayed in Fig. 4.7 (green lines), together with the sum of the real parts of the Fourier transforms (same additional broadening) of the FIDs demodulated according to (4.18) divided by the factor 10 (blue spectrum to the far left). The improvement in the signal-to-noise ratio is 3.0 and close to what we expect from averaging 10 FIDs. Thus the procedure of demodulating and phase-correcting also works well at high fields. The knowledge of the field after the experiment is rather precise so that simultaneous shift measurements on an unknown sample should be possible.

4.6. Discussion

According to our findings the time dependence of the field in the investigated pulsed magnets does not pose a serious problem for NMR measurements at the HLD. While it is not possible to predict neither the point in time of the occurrence of the field maximum nor its amplitude with sufficient accuracy before the experiment, after the experiment, we know the field with very high precision over a large period of time. Variations in the charging voltage of the capacitor bank (that always has a slight leakage), small differences in the magnet base temperature (or its temperature distribution), and perhaps a range of other factors seem to prevent us from improving sufficiently on the prediction of the actual field such that we can reach chemical-shift precision. On the other hand, the knowledge of the field obtained after the field pulse seems to be limited only indirectly by the homogeneity of the field across the sample, at least at the current level of already very high accuracy.

With the ability to remove the time dependence of the magnetic field from our data we can address further questions such as measurements of the field homogeneity, Knight- and chemical shifts or T_1 and T_2 relaxation times in the next chapter.

5. Advanced NMR experiments in pulsed fields

We will now use the concepts of the previous chapter and discuss advanced NMR experiments addressing measurements of (i) field homogeneity, (ii) field amplitude of a dual coil, (iii) chemical shift σ , (iv) Knight shift K , (v) T_2 , and (vi) T_1 . While our treatment of these problems is not as rigorous as that of the time dependence, we still claim that the measurements of NMR parameters σ , K , T_2 and T_1 are the first such measurements performed in pulsed fields (of course spin echo measurements published by Kozlov et al. [3] and Zheng et al. [38] establish a small lower bound for T_2).

5.1. Exploratory measurements of the field homogeneity

As pointed out in the previous chapter, the reproducibility of the field pulse's maximum is rather poor and therefore the field homogeneity cannot be measured by simply measuring the position dependence of the Larmor frequency as one would do in static fields. The most suitable approach to measure the spatial field distribution would probably be to use an array of microcoils (cf. [39]) (e.g., five microcoils for the longitudinal dependence and another four microcoils for the radial dependence) and a spectrometer with a correspondingly large number of channels. Such experiments, although being planned, are beyond the scope of this thesis.

In a first attempt by S. Greiser, a tank circuit with two NMR coils separated by 1 cm in the z direction was used to estimate the field distribution of the LP coil, cf. Fig. 3.2. While such an approach yields an estimate of $B(z)$ as described in his diploma thesis [40] it's main drawback is that the resonances can not be distinguished if the samples approach positions which experience the same local field. In addition, the probe used for these measurements was not equipped with a linear stage leading to an error in z of the order of 1 mm (The z -position was measured using a laser balance that projected a streak of 1 mm height on a ruler which was fixed on the probe).

In a later attempt, we tried to use our home-built probe (equipped with a linear stage and two RF channels) and a home-built RF downconverter¹ to record the signals from two coils with two independent channels. However, at the time of these experiments, the LP coil was not available anymore so that the experiment had to be performed in the

¹The RF downconverter was developed by H. Voigt.

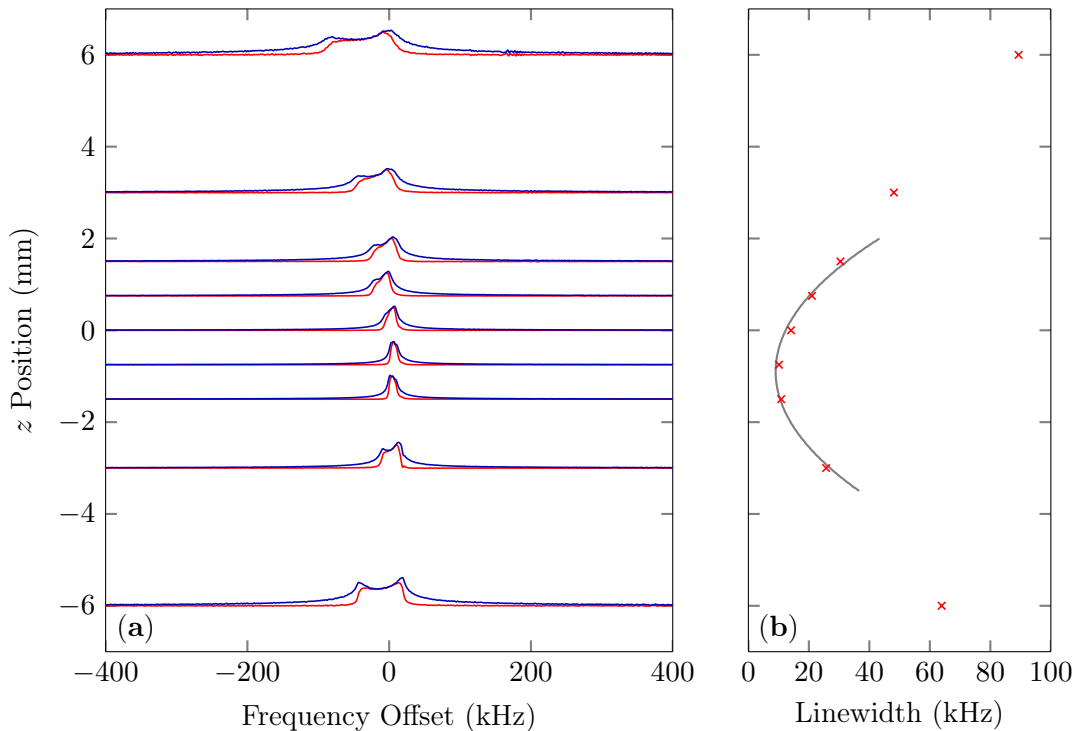


Figure 5.1.: Dependence of the linewidth on the z -position. In (a) we show real (red) and magnitude (blue) spectra normalized with respect to their peak intensity and vertically offset by the z -position at which a given spectrum was measured. All spectra were demodulated using either a simple field fit based on the maximum of the magnitude spectra or a complete phase fit. In (b) we show the obtained full width at half maximum values of the real part of the spectra plotted in (a). The gray line is a guide to the eye assuming a field curvature of 5 ppm/mm^2 centered at -0.9 mm .

(less homogeneous) KS3 coil. For this coil, the spacing between the two coils (2 cm) was much too large, so that the resonance line of (at least) one coil was too broad for a precise determination of the field.

The relevant figure of merit for most NMR experiments of course is the dependence of the linewidth of a given sample volume on the sample's position. In what follows, we describe a position dependent measurement of the NMR linewidth of a water sample in greater detail.

5.1.1. Experimental

For our experiment we used water with GdCl_3 (estimated $T_1 \approx 0.7 \text{ ms}$, cf. 4.1). The probe's tank circuit was the one described in section 3.4. The sample diameter was 1 mm and the sample length was 2 mm corresponding to a sample volume of $1.6 \mu\text{l}$. A slightly different Q value of 61 was measured. The pulse length was set to 200 ns at an RF generator power of 8 dBm (cf. 3.5). With the carrier frequency at 408 MHz, a free induction decay was excited every $500 \mu\text{s}$.

First, the probe was rotated in steps of 90° to control whether the probe axis was

concentric with respect to the magnet.² Subsequently, the sample's z position was varied using the linear stage of the probe. The step size was 0.75 mm in the vicinity of the estimated field maximum and 1.5 mm or 3 mm at positions further apart.

5.1.2. Results

We did not find a significant change in the linewidth when rotating the probe and therefore assume the probe to be concentric within our resolution.

In order to determine the inhomogeneous linewidth, the broadening due to the field's change with time has to be removed from the data, i.e., the data has to be demodulated. As discussed in the previous chapter, this requires one to know the field's time dependence with sufficient precision. However, we found that it is not possible to fit the phase information of the NMR data taken at positions further apart from the field center due to the rapid decay of the FID. Hence, we use the phase fitting procedure for positions close to the center of the magnet and the FT procedure for positions further apart. When using the phase fitting procedure, the first 100 μ s of each FID were taken into account. The total number of FIDs relevant to the fit was typically 8. The obtained coefficients for the fit to $B(t)$ according to Eq. (4.2) (with $\beta = 0$) are given in Tab. 5.1.

While the error estimates of the fit parameters (given in parenthesis in Tab. 5.1) have to be treated with care for inhomogeneous lines, no modulations can be seen in the demodulated spectra shown in Fig. 5.1(a). For each spectrum we have plotted the linewidth (i.e., the full width at half maximum of the real part of the spectrum) in Fig. 5.1(b).

In what follows we analyze the linewidth in terms of a local model for the field's dependence on z , i.e.

$$B(z) = B_{\max} (1 - \kappa(z - z_{\max})^2). \quad (5.1)$$

Likewise, the resonance frequency is position dependent, i.e.

$$f(z) = f_0 (1 - \kappa(z - z_{\max})^2), \quad (5.2)$$

where f_0 is the Larmor frequency.

Neglecting the exact shape of our sample and taking into account only the z -gradient,³ we can estimate our linewidth as

$$\Delta f = f(z + r) - f(z - r) + f_c = 2f_0\kappa((z - z_{\max})^2 + r^2) + f_c, \quad (5.3)$$

where r is the sample diameter. Here, we have included the heuristic term f_c to take into account a constant contribution to the linewidth that cannot be understood in terms of

²This is not guaranteed since the outer diameter of the cryostat is about 1 mm smaller than the inner diameter of the coil. Furthermore, most of the cryostat tails are slightly bend due to the stressing insertion procedure (The cryostats are inserted into the coil using a crane. If one does not hit the inner bore of the coil, the full weight of the cryostat bears on its tail).

³This simplification gives some insight into the NMR lineshape that is worth mentioning.

z (mm)	Fit	B_{\max} (Tesla)	t_{\max} (ms)	α (s ⁻²)	Δf (kHz)
-6.00	FT	9.5750(4)	9.82(1)	858(13)	63.9
-3.00	FT	9.5798(1)	9.930(4)	861(6)	25.7
-1.50	ϕ	9.580 487(5)	10.0911(1)	855.2(2)	10.8
-0.75	ϕ	9.580 608(5)	10.1109(2)	856.5(2)	10.1
0.00	ϕ	9.581 965(5)	9.7507(2)	857.5(2)	14.1
0.75	ϕ	9.581 50(1)	8.3708(4)	854.8(5)	21.0
1.50	FT	9.5790(1)	9.832(4)	857(5)	30.4
3.00	FT	9.5783(3)	10.064(6)	860(6)	48.1
6.00	FT	9.5788(2)	10.139(4)	857(4)	89.3

Table 5.1.: Results of fits to $B(t)$ as described in the previous chapter. If possible a phase fit was performed (indicated by the symbol ϕ). After demodulating the data using Eq. (4.17) and the coefficients given here, the spectra in Fig. 6.4 are obtained. The linewidth (FWHM of the real part) was determined from the demodulated data (last column).

$B(z)$. Of course at the center of the field $f(z_{\max} + r) = f(z_{\max} - r)$, the two expressions cancel. This effect can be compensated for by replacing $f(z + r) - f(z - r)$ with $f(r)$ if the latter is larger than the former. However, as we will shortly see, $f_c \gg f(r)$ and the effect can be neglected.

The gray dashed line in Fig. 6.4(b) is a plot of Eq. (5.3) with $f_c = 8$ kHz, $a = 5$ ppm/mm² and $z_{\max} = -0.9$ mm.

We conclude from this drawing that the field center is 0.9 mm below the previously expected value. The constant contribution f_c equals 20 ppm and has to be addressed in future experiments, especially if a higher spectral resolution is required. The term f_c cannot be understood in terms of the curvature of the field alone. We also note here that the T_2 is of the order of at least 1 ms (cf. section 5.5) and can not account for f_c . Another possible source of inhomogeneous broadening are eddy currents. Anyway, we did not find a significant dependence of the linewidth on $B(t)$ (at the maximum, the derivative of $B(t)$ vanishes and so do the eddy currents). At the time of this writing we can not give a solid explanation for f_c . We hope, however, that experiments with microcoils scheduled for summer 2012 will give additional insight.

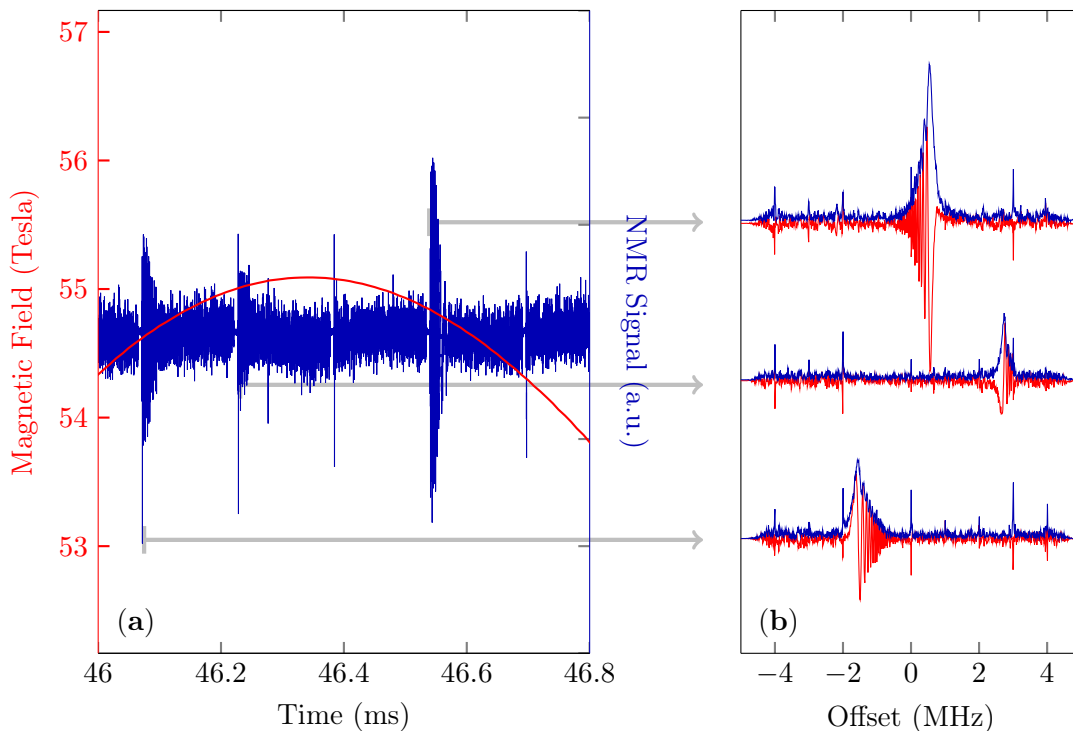


Figure 5.2.: NMR measurements in a dual coil. In (a) we show a series of five FID measurements in the vicinity of the field maximum. The red curve in (a) shows a rescaled field measurement that was done using a pick-up coil. The NMR data is centered at the resonance frequency of the probe divided by the gyromagnetic ratio of ^{63}Cu . Close to resonance an FID is obtained after each pulse; the corresponding spectra are shown in (b). As expected, the spectra show strong modulation features due to the strong time dependence of the field. The spikes in (b) are probably caused by some noise that is picked up from the pulsed field facility.

5.2. Measurements in a dual coil

As discussed in chapter 3, fields generated with single coils have a limited maximum field of about 70 Tesla. While this is a sufficient value for many experiments, some measurements (e.g. certain quantum oscillation experiments) demand even higher fields. Given the very strong time dependence of the inner coil (a field-profile of a dual coil is shown in Fig. 3.2), it is true that NMR experiments on e.g. strongly correlated electron systems are not very likely to be successful in the near future.

However, we performed NMR experiments in a dual coil for two reasons: Firstly, NMR is expected to provide a very accurate field calibration even in dual coils. As soon as one observes a resonance, a field value can be determined with a precision of the order of 1 ‰.⁴ Secondly, we can try to apply the ideas of the previous chapter in order to see if they also work if the time dependence is much stronger than so far.

⁴At 50 Tesla a broad line might have a width of 500 kHz. For copper this corresponds to roughly 1 ‰ of the Larmor frequency.

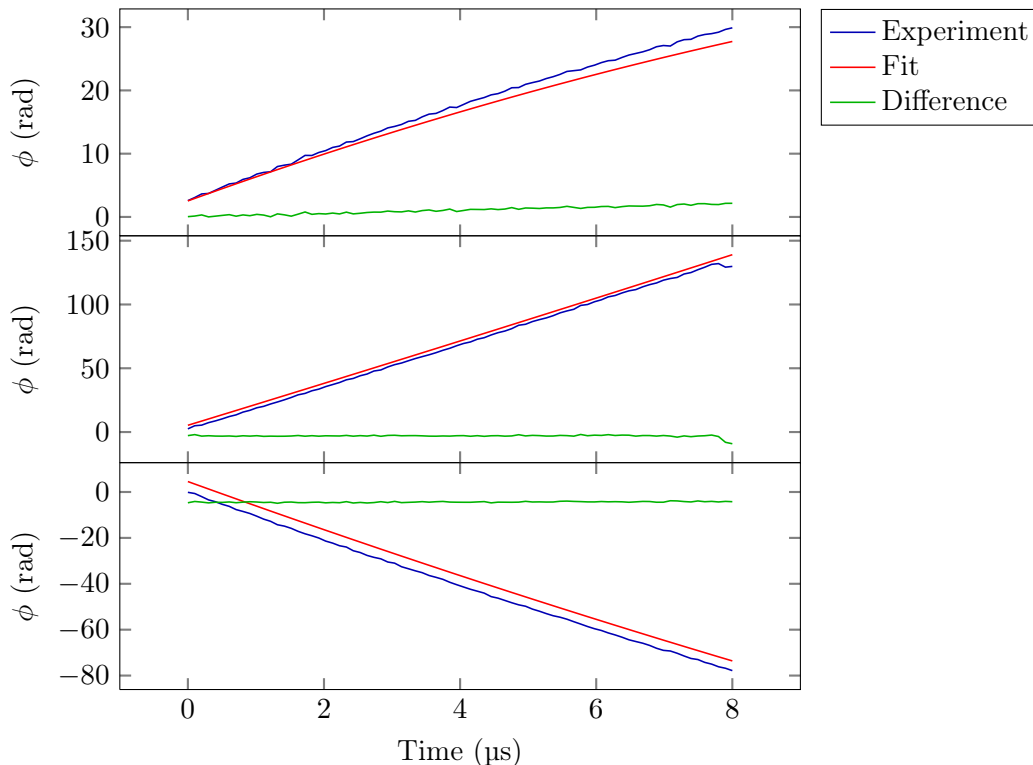


Figure 5.3.: Experimental phase (blue curve) and fit (red curve) of the three FIDs shown in Fig. 5.2. The fit approximates the data with reasonable accuracy. The green curve shows the difference between fit and data; systematic deviations are clearly visible. Note also the kink at the end of the phase information of the second FID; it is an example for an error in the unwrap procedure discussed in the previous chapter.

Clearly, we do not expect to get a precision as high as for the previous measurements where typically 10 FIDs were available to fit the field to the data. However, we will see that the phase fitting procedure discussed in the previous chapter returns reasonable parameter estimates that are successfully tested by demodulating the experimental data.

5.2.1. Experimental

We used a mixture of metallic copper (grain size $< 10\ \mu\text{m}$, purity 99%) in epoxy resin (~ 50 percent by weight). A fraction of diameter 1 mm and length about 2 mm was cut from the material and inserted into the RF coil. Subsequently, the tank circuit was tuned to 620 MHz and matched to 50 Ohm by tapping the coil as discussed in section 3.3. The resonance frequency of 620 MHz reflects the limited rated maximum frequency of the power amplifier of only 500 MHz. The amplifier has sufficient gain for frequencies up to about 600 MHz, but at 700 MHz the output power drops to typically 100 W.

Since the diameter of the dual coil's inner bore is only 16 mm, the probe was inserted into the coil without a cryostat. The sample was therefore immersed in liquid nitrogen. The z -position of the sample was set to the geometric center of the magnet.

The RF power level was 400 W corresponding to an estimated $\pi/2$ pulse duration of

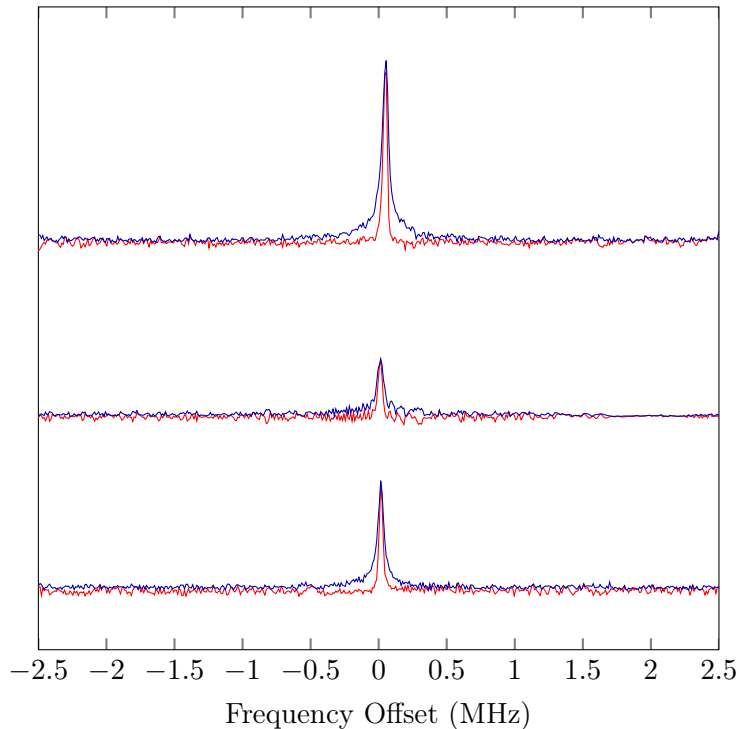


Figure 5.4.: Fourier transforms of the FIDs after demodulation using the fitted field. We show magnitude (blue) and real part (red) of the phased spectra. The phase of each spectrum was adjusted separately (zeroth order only). The effect of the demodulation can be seen from the significant line-narrowing, i.e. the linewidth has decreased by a factor of six when compared to Fig. 5.2. However, some modulations have remained in the second spectrum. Also the position of the spectral maxima does not perfectly coincide with zero, see text.

600 ns. We chose a pulse duration of only 300 ns in order to have sufficient excitation bandwidth. Such a RF pulse was applied every 150 μ s in the vicinity of the expected field maximum.

The dual coil is powered by different modules of the capacitor bank. Three modules in parallel are used to drive the outer coil, one module is used to drive the inner coil. The modules are charged to the same voltage, but the point in time at which they are discharged can be set.

For our experiment all coils were charged to 13.6 kV to give an estimated field of 54.9 Tesla.

5.2.2. Results

The results of our experiment are shown in Fig. 5.2. We obtained three FIDs in the vicinity of the field maximum. The corresponding spectra (with an additional exponential line broadening of 20 kHz) are shown in Fig. 5.2(b). In Fig. 5.2(a) we also show a plot of the field's time dependence obtained from rescaling integrated pick-up coil data that was measured for a capacitor bank voltage of 15.5 kV.

The spectra in 5.2 show strong modulation features with a magnitude linewidth (FWHM) of about 300 kHz. Of course a simple fit of a three parameter model for $B(t)$ using the positions of the maxima of the three spectra cannot give any information about the confidence intervals.⁵ Thus we have tried to perform our phase fit with starting values of $B_{\max} = 55$ T, $t_{\max} = 46.3$ ms and $a = 0.1/\text{ms}^2$. We varied the interval over which the fit was carried out between 2 and 20 μs and obtained good results for 8 μs or 80 points per FID. The fit results are $B_{\max} = 55.0904(5)$ T (10 ppm), $t_{\max} = 46.3418(1)$ ms and $a = 0.117(2)/\text{ms}^2$.

In Fig. 5.3 we plot the experimental phase information (blue curves) together with the values computed from the fit (red curves). The green curves in Fig. 5.3 show the difference between fit and experimental data. While the fit approximates the experimental data rather well, the green curves reveal systematic deviations between fit and the experimental data; therefore the error estimates have to be treated with care. The small kink at the end of the experimental phase of the second plot in Fig. 5.3 is an example of an error in the unwrap procedure described in the previous chapter.

A straight forward test of the fit is to demodulate the experimental data using Eq. (4.3) and Eq. (4.4). If the fit were perfect, after demodulation the spectra would appear without modulations at zero resonance offset. Likewise, if the spectra show a resonance offset after demodulation, we can take this offset as a measure of the error in $B(t)$ during the time of the corresponding FID.

The spectra of the demodulated FIDs are shown in Fig. 5.4. Note that the x axis range is now only half of the range in Fig. 5.2(b). The linewidth of the magnitude spectra (FWHM) ranges between 51 and 57 kHz, i.e. it is reduced by a factor of six (real part: 32 to 38 kHz or 50 ppm). Correspondingly, the increase in signal-to-noise ratio can be seen with the eye.

However, a closer look at the second spectrum reveals small frequency modulations pointing to systematic errors in the fit. The errors can be estimated by checking the position of the peaks of the spectra. Instead of zero offset, the measured offset for the three peaks is 15, 15 and 55 kHz.

As discussed above, the detected offset is a suitable measure for the error in the field determination. The maximum error corresponds to

$$\Delta B = \frac{55 \text{ kHz}}{620 \text{ MHz}} \times 55.0904 \text{ T} = 4.9 \text{ mT} \quad (5.4)$$

or 89 ppm, i.e. the error is about a factor of 10 larger than the error estimate of the maximum value B_{\max} . From the fit itself one would expect a factor of two in the errors due to the error estimates of t_{\max} and a (obtained simply by evaluating $\sum_i |\partial B(t)/\partial x_i| X_i$ where x_i is the i -th coefficient and X_i its error estimate). A possible explanation for the remaining factor of five is the fact that we only fit a rather small fraction of each FID making the fit less representative for the given data. We also note that the field generated

⁵This causes Python's `curve_fit` routine to fail, Matlab's `nlinfit` however returns coefficients and only throws a warning.

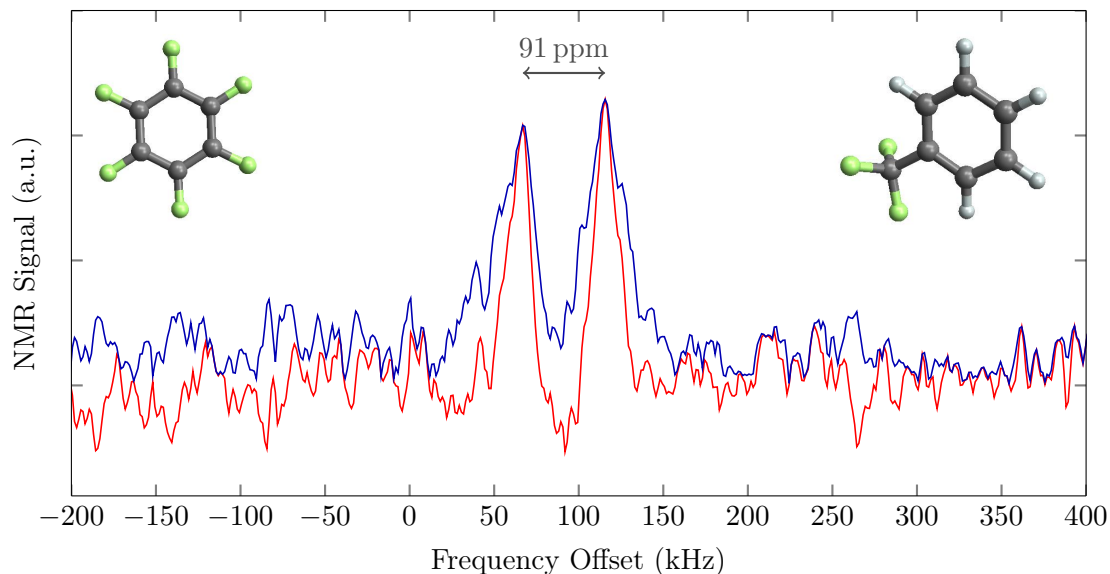


Figure 5.5.: Measurement of ^{19}F chemical shifts using Hexafluorobenzene (C_6F_6 shown in the upper left corner, expected shift -162.2 ppm) and Trifluorotoluene ($\text{C}_6\text{H}_5\text{CF}_3$, shown in the upper right corner, expected shift -63.5 ppm). Based on the shift of the Hexafluorobenzene resonance, the peak to peak distance of the two spectra is 91 ppm, i.e. the deviation between expected and measured shift difference is less than 10 %.

by the outer coil varies during the pulse of the inner coil. If the maxima of the pulses from inner and outer coil do not coincide perfectly, our local model for $B(t)$ will be less suitable.

To obtain the final result, we have to take into account the Knight shift of metallic copper which is 2393 ppm [41]. The Knight shift measures the density of states at the Fermi surface and is therefore itself field dependent. Field-dependent shift measurements (i.e. quantum oscillations) have been performed by Khan [42] and Goodrich [43]. The observed oscillations in the shift were of the order of 1 % of the shift; we thus believe that they can be neglected here also for the case of copper (powder).

Thus, the final result is obtained as

$$B_{\text{max,final}} = \frac{B_{\text{max}}}{1.002393} = 54.959(5) \text{ Tesla}, \quad (5.5)$$

i.e. the error in the determination of the field maximum is 0.1 %.

5.3. Chemical shift

The experiments discussed so far suggest that it is indeed possible to measure chemical shifts in pulsed field NMR, at least if the shift differences are greater than the observed resolution of about 30 ppm. While the light hydrogen nucleus has a smaller shift range of only 10 ppm, other, heavier nuclei have significantly larger shift ranges. We describe here a measurement of ^{19}F chemical shifts with pulsed field NMR performed in the KS3 coil

(described in section 3.1).⁶

5.3.1. Experimental

We used a mixture of 40 μL Hexafluorobenzene (C_6F_6) and 70 μL of Trifluorotoluene ($\text{C}_6\text{H}_5\text{CF}_3$). The fluorine chemical shifts with respect to CFCl_3 for these compounds are -162.2 ppm and -63.5 ppm, respectively [44, 45] (we neglect small couplings between F and H spins in Trifluorotoluene). We added 50 mg TEMPO (a benzene soluble, stable radical) as relaxation agent. All chemicals were purchased from Sigma-Aldrich. Assuming the viscosity of the solution to be given by the mean of the viscosities of Hexafluorobenzene and Trifluorotoluene (their viscosities differ by a factor of five), the estimated value of T_1 based on Eq. (2.16) is 0.37 ms.

A volume of 60 nL was pipetted into a glass capillary of 0.5 mm diameter. The capillary was sealed and fixed in a coil of 0.6 mm diameter with glue. The length of the coil was 2.9 mm. The resonance frequency of the circuit was 511.2 MHz at a Q of 80 leading to an estimated pulse length of 200 ns for the applied RF power of 150 Watt. An RF pulse of this length was applied every 2 ms.

5.3.2. Results

In the vicinity of the field maximum two signals were obtained. The signals cannot be seen in the time-domain (without applying a filter), but the corresponding spectra (with an additional line-broadening of 10 kHz) clearly reveal two peaks.

In Fig. 5.5 we show real part and magnitude of the spectrum with the higher signal-to-noise ratio as red and blue lines, respectively. Lacking a precise knowledge of the field, we have not demodulated the data. However, the chosen spectrum does not show strong modulation features indicating that the signal was measured shortly before or after the field maximum. This assumption is also supported by the observation of two ^1H signals from the TEMPO protons at times symmetric about the time at which the fluorine signal was recorded.⁷

We observe two resolved resonances with linewidths of 15 and 17 kHz (FWHM real part), corresponding to 29 and 33 ppm. The chemical shift difference can be estimated from the separation between the maxima of the resonances (magnitude). The maxima are observed at 68.88 and 115.64 kHz.

If we assign the lower resonance frequency to a shift value of $\delta_1 = -162.2$ ppm, we can calculate the zero shift frequency as

$$\nu_0 = \frac{\nu_1}{\delta_1 + 1} = \frac{511.2 \text{ MHz} + 68.88 \text{ kHz}}{1 - 162.2 \text{ ppm}} = 511.35182 \text{ MHz}. \quad (5.6)$$

⁶We thank Jacob Schaefer, Washington University, St. Louis for proposing this experiment and pointing us to a suitable sample. The experiment was carried out together with J. Kohlrantz.

⁷The observation of these proton resonances actually marks the first time a pulsed field NMR signal was seen “incidentally”.

Then, of course, the shift of the second resonance is

$$\delta_2 = \frac{\nu_2 - \nu_0}{\nu_0} = -71 \text{ ppm.} \quad (5.7)$$

The observed shift difference is 91 ppm which is about 10 % below the expected difference.

While such an error is quite high for many measurements in static fields, the presented data clearly shows that fundamentally measurements of chemical shifts in pulsed fields are feasible.

5.4. Knight shift

The data in the previous section was measured at comparably low fields since the spectrometer currently is not equipped with an RF power amplifier for very high frequencies. While we have not yet performed a chemical shift measurement at high fields we have exploited the relatively small gyromagnetic ratio of ^{27}Al and performed a Knight shift measurement at a field of 60.36 Tesla that we will discuss below.

We note that the Knight shift of Al metal is field dependent and quantum oscillations have been observed by Khan et al. [42] using single crystal NMR. In their experiments they found that the shift varied by less than 1 % depending on the strength of the applied magnetic field.

5.4.1. Experimental

For our experiment we used a solution of 1 g H_2O , 0.9 g AlCl_3 hexahydrate that was saturated with approximately 0.8 g GdCl_3 . A fraction of the sample was pipetted into a glass capillary of 1 mm diameter and approximately 2 mm length. The sample was fixed in a tank circuit with a resonance frequency of 670 MHz. The frequency of 670 MHz is above the specified frequency range of the power amplifier (cf. section 3.2.3), so that the available power was only 300 Watt for an input power of 10 dBm. Due to time-constraints the matching of the RF circuit inside the magnet was poor and the Q could not be determined. (The return loss was only about -10 dB.) We consequently decided to use RF pulses of 500 ns duration every 400 μs such as to have sufficient excitation bandwidth in order to observe both signals simultaneously.

5.4.2. Results

In Fig. 5.6(a) we show a spectrum obtained by a Fourier transform of an FID (using 10 kHz exponential linebroadening). The FID, shown in Fig. 5.6(b) was measured approximately 2 ms prior to the field maximum. The spectrum shows two signals from which the Knight shift can be derived. However, the poor SNR renders a simple frequency comparison inadequate. Moreover, lacking a precise knowledge of the field as function of time, the spectra are not demodulated, and the frequency of their respective maxima may be shifted.

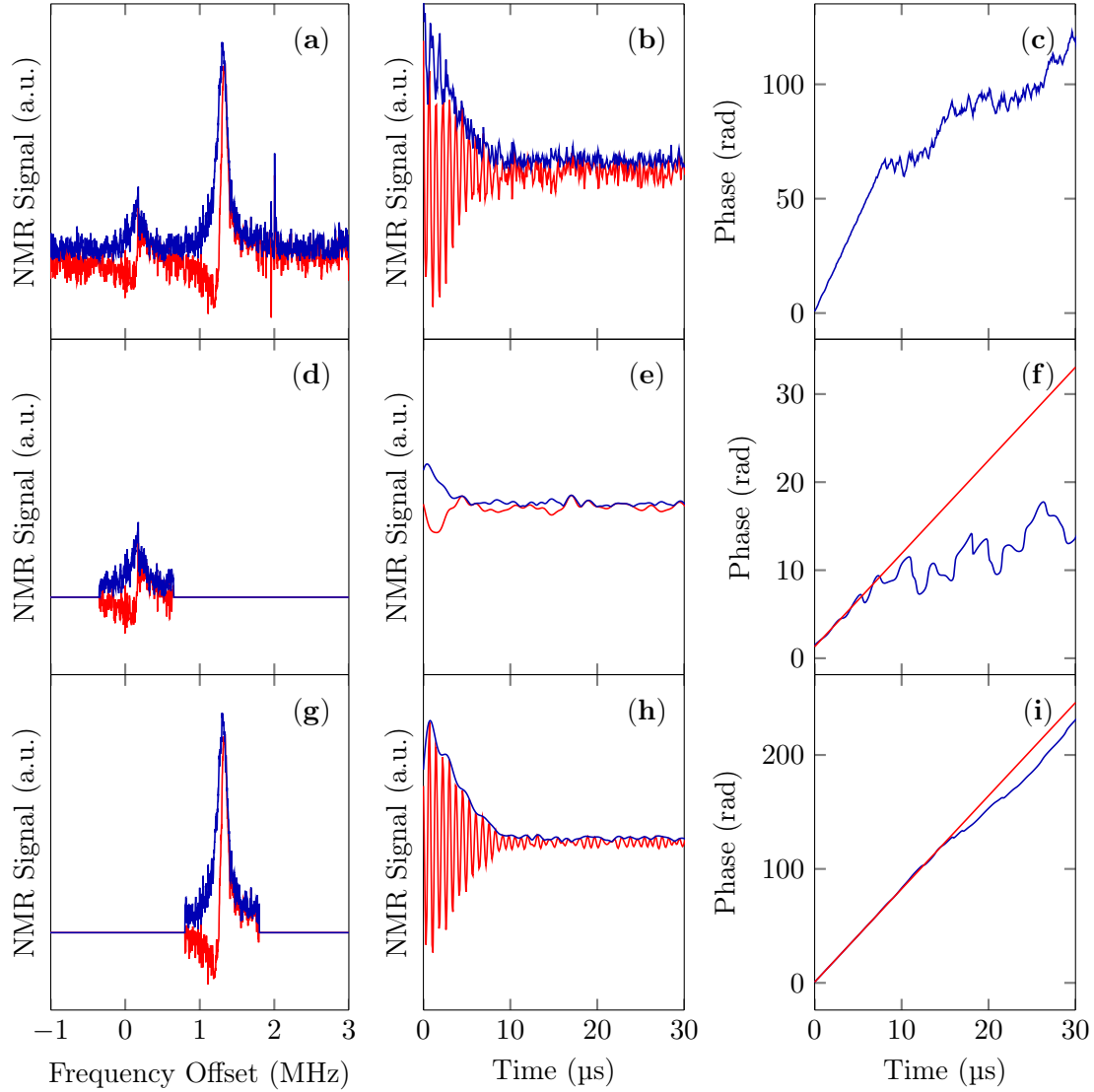


Figure 5.6.: Measurement of Al Knight shift at a field of approximately 60.36 Tesla. In the left column we show a spectrum obtained by a Fourier transform of a free induction decay. With a carrier frequency of 670 MHz, we obtain two resonances. In order to determine the shift with higher precision, the data is filtered in the frequency transform (second and third plot in the first column). The second column shows the corresponding FIDs (the second and third FID are obtained via an inverse Fourier transform). From the filtered FID the resonance offset is determined via a linear phase fit performed in the first $5 \mu\text{s}$.

However, the data can also be analyzed in terms of the phase of the two signals as we will now demonstrate.

5.4.3. Discussion

In order to analyze the data in the time-domain we have to focus on one signal at a time. We accordingly filter the data using an ideal bandpass of width 1 MHz, centered around the frequency of the maximum of a given resonance. The filtered spectra are shown in

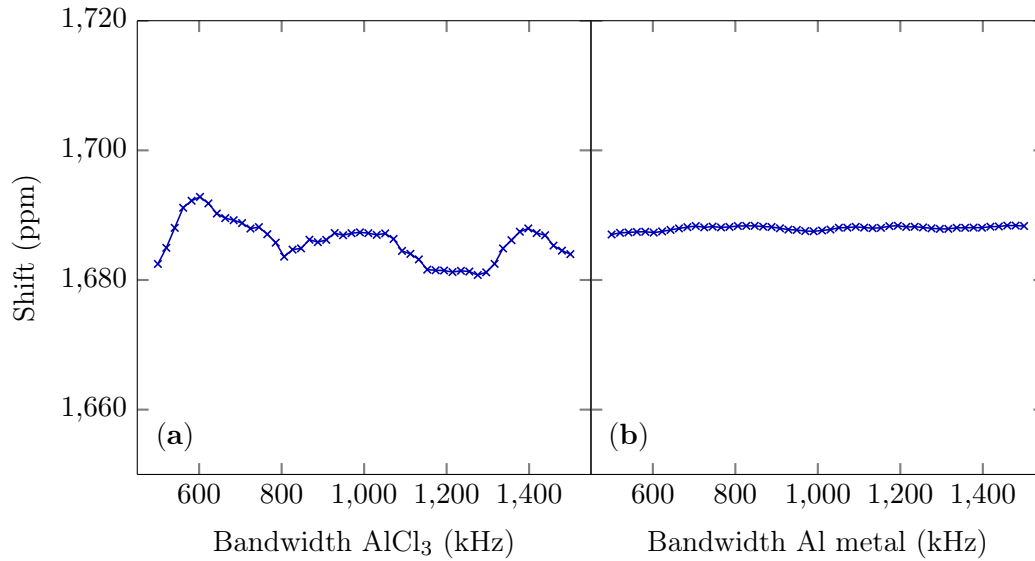


Figure 5.7.: Measured Knight shift as a function of the width of the applied filter. In (a) we keep the aluminum metal filter width constant and vary the width of the AlCl_3 filter between 0.5 and 1.5 MHz. The shift changes by ± 10 ppm depending on the filter width. As can be seen in (b) the shift does not depend strongly on the width of the filter applied to the metallic signal.

Fig. 5.6(d) and (g) for AlCl_3 and Al metal, respectively. For each resonance we can obtain the corresponding FID (plotted in (e) and (h)) by applying an inverse Fourier transform.⁸

For the two filtered FIDs we plot the phase in (f) and (i). Subsequently, we fit the phase during the first $5 \mu\text{s}$ using a linear model, i.e.,

$$\phi(t) = \phi_0 + \Delta\omega t \quad (5.8)$$

The obtained offset $\Delta\omega/2\pi$ yields $\Delta\nu_0 = 168(5)$ kHz for the AlCl_3 resonance and $\Delta\nu_1 =$

⁸We denote the spectrum by $S(f)$ and the filter by $H(f)$. Then, the filtered signal S_f is given as $S_f(f) = S(f)H(f)$. The convolution theorem states that $s_f(t) = (s * h)(t)$, i.e. the inverse FT of the filtered spectrum is given by the convolution of the time-domain data $s(t)$ with the inverse Fourier transform of the filter $H(f)$. In our case we have

$$h(t) = \int_{f_c - b/2}^{f_c + b/2} \exp(2\pi i f t) df = b \exp(2\pi i f_c t) \text{sinc}(\pi b t),$$

where f_c is the center frequency of the filter and b is its bandwidth. If we write the FID as $\exp(i\Delta\omega t - t/T_2)$ for $t > 0$ (and 0 otherwise), then its convolution is

$$\begin{aligned} & \int_{-\infty}^0 b \exp(2\pi i f_c \tau) \text{sinc}(\pi b \tau) \exp(i\Delta\omega(t - \tau)) \exp(-(t - \tau)/T_2) d\tau \\ &= \exp(i\Delta\omega t - t/T_2) \int_{-\infty}^0 b \exp(2\pi i f_c \tau) \text{sinc}(\pi b \tau) \exp(-i\Delta\omega \tau) \exp(\tau/T_2) d\tau, \end{aligned}$$

Hence, the signal is only altered by a constant factor. Since the support of the sinc function is infinite, a numerical convolution in the time-domain leads to ripples in the passband. We may use frequency filtering especially since many related problems (e.g. efficiency, lack of future data points) are irrelevant to our treatment.

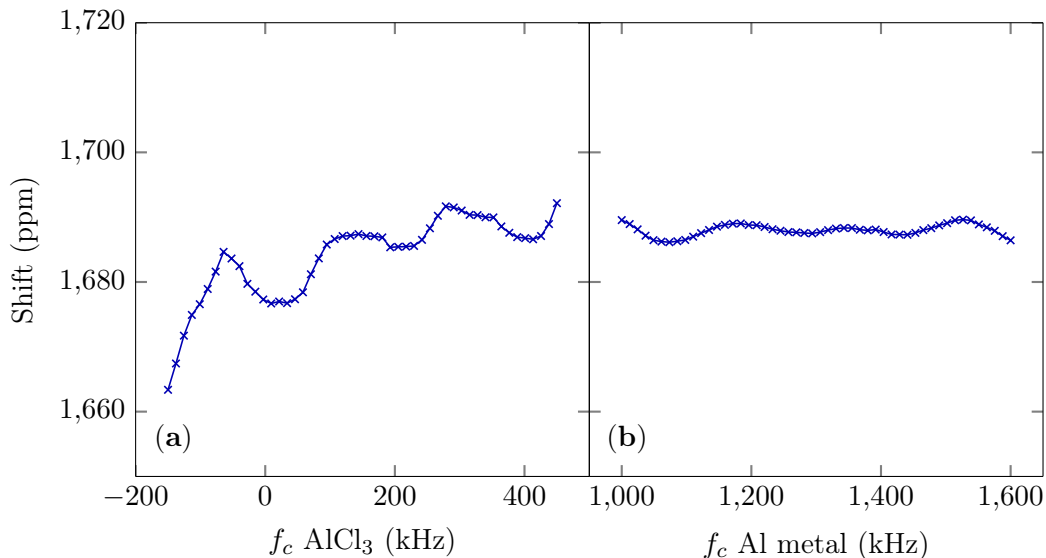


Figure 5.8.: Measured Knight shift as a function of the center frequency of the filter applied to (a) the AlCl_3 resonance and (b) the Al metal signal. In (a) the center frequency of the Al metal filter was fixed at 1.3 MHz, in (b) the center frequency of the AlCl_3 filter was fixed at 150 kHz. Depending on the center frequency of the AlCl_3 filter, the measured shift varies between 1660 and 1690 ppm, the dependence on the position of the AlCl_3 filter is less pronounced.

1301(1) kHz for the Al metal resonance.⁹

From the two resonance offsets and the carrier frequency $\nu = 670$ MHz the shift is readily derived as:

$$K = \frac{\Delta\nu_1 - \Delta\nu_0}{\nu + \Delta\nu_0} = 1691 \text{ ppm.} \quad (5.9)$$

We denote the uncertainty in $\Delta\nu_i$ with $u(\Delta\nu_i)$. Then the error is obtained by error propagation,

$$\Delta K = \sum_i \left| \frac{\partial K}{\partial \Delta\nu_i} \right| u(\Delta\nu_i) = 9 \text{ ppm,} \quad (5.10)$$

so that the final result is

$$K = 1691(9) \text{ ppm.} \quad (5.11)$$

This value has to be compared with a literature value of 1640 ppm [41]. Clearly, the uncertainty in $\Delta\nu_i$ as derived from the fit can not account for the discrepancy. Other possible sources of error are the bandwidth and position of the filters used to generate the two FID. The dependence of the measured shift on position and width of the filters is demonstrated in Figs. 5.7 and 5.8. In either case we keep all parameters but one fixed. In Fig. 5.7 we plot the measured shift as function of (a) the width of the filter applied to the

⁹Although Eq. (5.8) is a linear equation we use again the Levenberg-Marquardt algorithm, error estimates are again computed as described in section 4.2.

AlCl_3 signal and (b) the width of the filter applied to the Al metal signal. The width of the remaining filter is 1 MHz in both cases. As can be seen, the measured shift varies between 1680 and 1690 ppm depending on the width of the filter applied to AlCl_3 , the dependence on the width of the filter applied to the metal signal is less pronounced.

In Fig. 5.8 we keep the width of both filters constant at 1 MHz. In (a) we vary the center frequency f_c of the filter applied to the AlCl_3 signal between -150 and 350 kHz while the filter applied to the aluminum signal is fixed at 1.3 MHz. In (b) we vary f_c of the filter applied to the Al metal signal between 1 and 1.6 MHz. Depending on the position of the AlCl_3 filter the shift varies between 1660 and 1690 ppm. The dependence on the position of the Al metal filter is again much smaller.

To conclude, we have demonstrated a measurement of the Knight shift of metallic aluminum at a field of 60.36 Tesla. In order to measure the shift, we have Fourier transformed the data and applied a frequency filter. Subsequently, an inverse transform is applied and the shift is determined using a phase fit. The measured shift is approximately 50 ppm larger than what is expected based on the literature values. The actual values depend on bandwidth and position of the applied filters. However, the smallest observed shift was 1660 ppm. At this stage, one cannot say whether the observed shift difference is due to a field effect or not, but the data presented here suggest a more thorough investigation of the shift at various field strengths.

5.5. Measurement of the spin-spin relaxation rate

In this section we demonstrate for the first time the use of a Carr-Purcell sequence to estimate values of T_2 using pulsed field NMR. Since the field varies in time, so does the resonance offset and a corresponding correction of the data is necessary. Such a correction requires knowledge of the flip angles of the various pulses.

If multiple spin echoes are obtained, one can use the observed intensity variation to estimate the flipping angle. We demonstrate this with an experiment on water (with added Gadolinium to shorten T_1) using four refocussing pulses. Subsequently, we discuss a Carr-Purcell sequence at 62 Tesla. The latter was performed with two refocussing pulses, only. Hence, no information about the flipping angle can be obtained and the data provide only a lower bound for T_2 .

5.5.1. Experimental

The ^1H experiment on water at low field was used also to discuss the signal-to-noise ratio in section 3.4. To repeat, the carrier frequency was set to 407.4 MHz (corresponding to ≈ 9.6 Tesla) at an RF power of 490 W and a Q of 51. The estimated $\pi/2$ -pulse was followed by a refocussing π -pulse after approximately 300 μs . Three further π -pulses were applied approximately 900, 1500 and 2100 μs after the initial pulse. The sequence defined by these

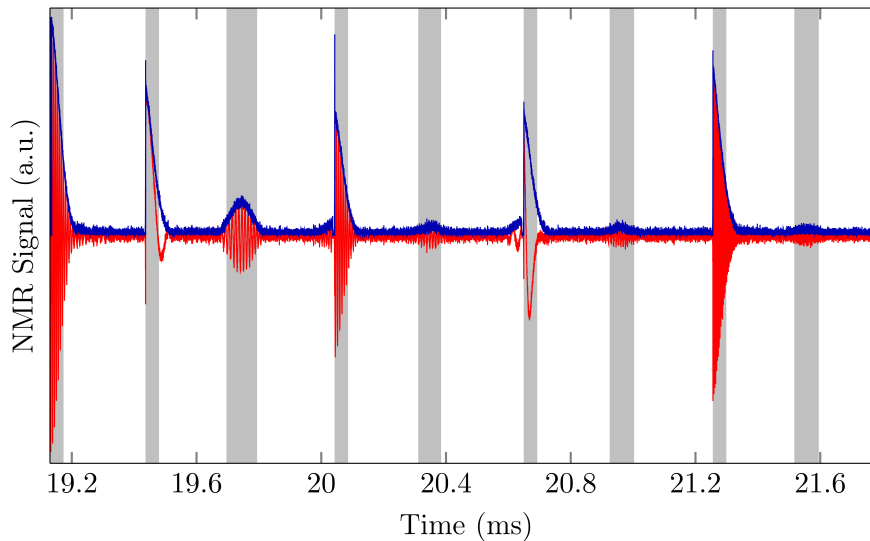


Figure 5.9.: Measurement of T_2 at approximately 9.6 Tesla using a Carr-Purcell sequence. One $\pi/2$ -pulse and four π -pulses are used to generate four spin echoes (Due to pulse imperfections and resonance offsets, an FID is obtained also after each π -pulse). In order to correct the decay for the time-dependent resonance offset, the field has to be determined with sufficient precision. This is done by extracting the phase information from the signal in the areas shaded in gray.

five pulses was repeated 20 times.

5.5.2. Results

The data of the 8-th Carr-Purcell sequence is plotted again in Fig. 5.9. One can see from the echo decay that T_2 is approximately 1 ms. However, even if the pulses were perfectly on resonance, the time-dependent resonance offset leads to imperfect refocussing and thus causes losses in the echo intensities.

5.5.3. Discussion

In order to correct for these losses we first have to determine $B(t)$ with sufficient precision. This is done by extracting the phase information from the NMR signals shown in Fig. 5.9. Due to the imperfections of the π -pulses these are also followed by a free induction decay which can also be used to determine the field. At this point we do not know the initial phase of the spin echoes. We therefore subtract from the phase information of each of the gray shaded regions in Fig. 5.9 the phase at the beginning of the respective region. The obtained phase data in the n -th region is subsequently fitted to

$$\phi(t) = \gamma \int_{t_n}^t B(\tau) d\tau - \omega_c(t - t_n) \quad (5.12)$$

where $B(t)$ is the effective field averaged across the sample volume and t_n is the time at the beginning of the n -th region. The data from all regions are fitted simultaneously. For $B(\tau)$

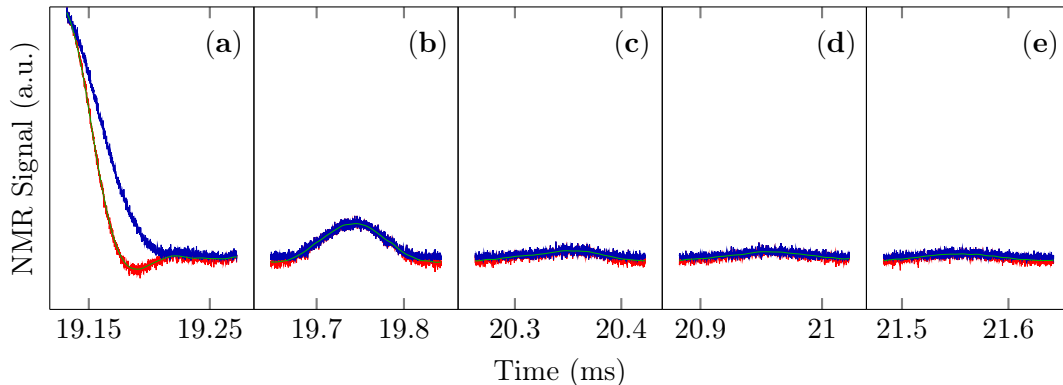


Figure 5.10.: The initial FID (a) and the four spin echoes (b - e) after demodulation. The demodulation is not perfect for the FID that was measured rather far apart from the field maximum. The green curve (fine line within the noisy data) is a local regression (LOESS) of the signal's real part using a Gaussian kernel with a bandwidth of 1 MHz. The maximum intensity of the smoothed regression curves is interpreted as the echo intensity of the respective echo.

we use again a local model, cf. Eq. (4.2). From the fit we obtain $B_{\max} = 9.571\,645(2)$ Tesla, $t_{\max} = 20.0707(2)$ ms, and $\alpha = 845.4(4)$ s⁻². Such a high precision suggests that we can, firstly, remove the time dependence from the data, and secondly, correct for the imperfect refocussing.

The relevant data for a determination of T_2 are the first FID and the four spin echoes. We replot the demodulated FID and echoes in Fig. 5.10. The FID (taken far apart from the field maximum) shows a small remaining resonance offset, but the echoes appear on resonance. The real parts of the signals are smoothed using a local regression with a Gaussian kernel with bandwidth $\sigma = 1$ MHz to reduce the influence of the noise, cf. section 3.2.3. The maximum of each of the smoothed curves is interpreted as the intensity at the given time and plotted as blue crosses on a logarithmic scale in Fig. 5.13.

Offset correction

The refocussing pulses are neither of perfect length, nor are they applied at resonance. Therefore, the echoes are expected to decay even if T_2 were infinite. In order to correct for this effect we use the spin density matrix.¹⁰

In the high-temperature approximation the thermal equilibrium density matrix in the Zeeman basis is given by [12]

$$\rho_{\text{eq}} = \begin{pmatrix} \frac{1}{2} + \frac{1}{4}\mathcal{B} & 0 \\ 0 & \frac{1}{2} - \frac{1}{4}\mathcal{B} \end{pmatrix} \quad (5.13)$$

Herein, $\mathcal{B} = \hbar\omega/k_B T$ is the Boltzmann factor. If one applies a given Hamiltonian \mathcal{H} for a

¹⁰The treatment is analogous to the discussion of the time-dependent phase in the previous chapter. Here, the density matrix formalism is used since it allows to include further interactions in the future.

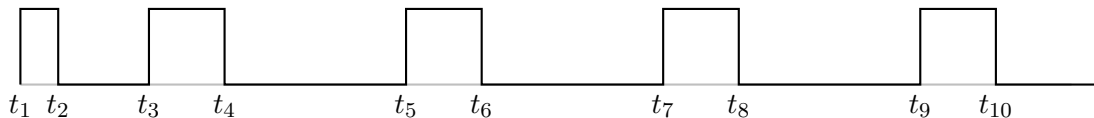


Figure 5.11.: Definition of times in the Carr-Purcell sequence. The length of the first pulse was 200 ns, the duration between first and second pulse is approximately 300 μ s, the duration between the later pulses is twice as long.

time t starting from equilibrium at $t = 0$, the density matrix at time t is given by

$$\rho(t) = e^{i\mathcal{H}t} \rho_{\text{eq}} e^{-i\mathcal{H}t} = U(t)\rho_{\text{eq}}U^\dagger(t), \quad (5.14)$$

where $U(t)$ is called the time-evolution operator.

The NMR signal $G(t)$ corresponds to the expectation value of \hat{I}^+ and can thus be computed as

$$G(t) \propto \text{Tr}\{\rho(t)\hat{I}^+\} \quad (5.15)$$

In our experiment we have two Hamiltonians corresponding to (i) free precession with a time-dependent resonance offset and (ii) excitation of a resonance. Their respective time-evolution operators are

$$U(t_0, t) = \exp \left[i \left(\gamma \int_{t_0}^t B(\tau) d\tau - \omega_c (t_0 - t) \right) \hat{I}_z \right] \quad (5.16)$$

$$P(t, \tau, \alpha) = \exp \left[i \left(\Omega(t) \hat{I}_z \tau + \alpha \hat{I}_x \right) \right]. \quad (5.17)$$

The first operator $U(t_0, t)$ corresponds to the time-evolution described in the previous chapter. Due to the time dependence of the magnetic field, the Hamiltonian becomes time-dependent as well.¹¹ As demonstrated in the previous chapter, the field changes smoothly with time so that we simply integrate the time-dependent Hamiltonian. The second operator $P(t, \tau, \alpha)$ describes the effect of an x -pulse with nutation angle α . The pulse with duration τ is applied at time t . The offset resonance $\Omega(t)$ is assumed to be constant for the duration of the pulse.

Using the two operators defined above, we can calculate the expectation value of \hat{I}^+ at any time by sandwiching the equilibrium density matrix. For example, with the definitions

¹¹Concerning $U(t_0, t)$, at each point in time the Hamiltonian is given by a constant times \hat{I}_z .

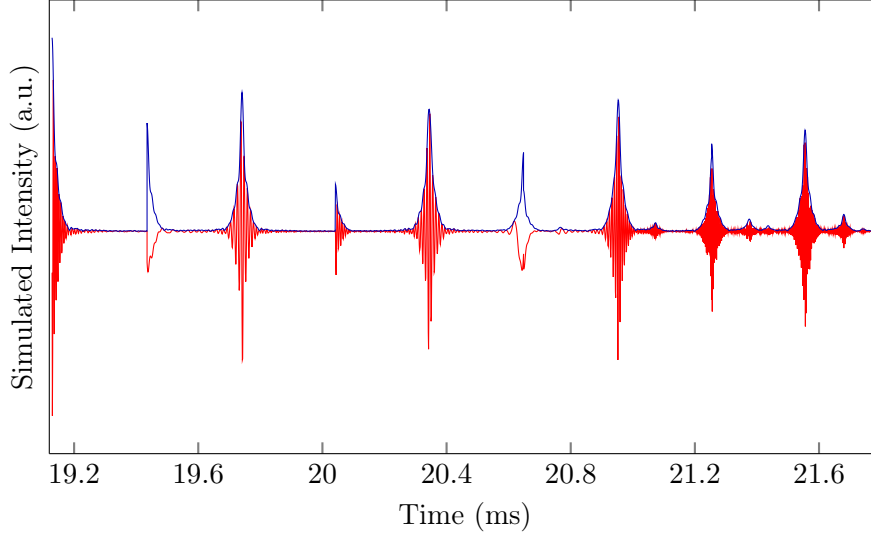


Figure 5.12.: Simulation of the NMR spin echo intensity. We average the time dependence of the density matrix over an ensemble of magnetic fields $B(t)$ that is derived from the demodulated spectrum. From the averaged ensemble the time-dependent NMR signal is obtained using Eq. (5.15).

given in Fig. 5.11, the density matrix after the second pulse or for $t \in (t_4, t_5)$ is given by

$$\begin{aligned}
 \rho(t)_{t \in (t_4, t_5)} &= U(t_4, t) P \left(\frac{t_3 + t_4}{2}, t_4 - t_3, \beta \right) \\
 &\quad \times U(t_2, t_3) P \left(\frac{t_1 + t_2}{2}, t_2 - t_1, \alpha \right) \\
 &\quad \times \rho_{\text{eq}} \\
 &\quad \times P^\dagger \left(\frac{t_1 + t_2}{2}, t_2 - t_1, \alpha \right) U^\dagger(t_2, t_3) \\
 &\quad \times P^\dagger \left(\frac{t_3 + t_4}{2}, t_4 - t_3, \beta \right) U^\dagger(t_4, t)
 \end{aligned} \tag{5.18}$$

Note that we have used flip angles of α and β for the $\pi/2$ and π -pulses, respectively. By varying these, we can tune the time-evolution of Eq. (5.18) to match the experimental data. The flip angles are a measure of the strength of the B_1 field. Since the first pulse has half the length of all the other pulses, we fix $\beta = 2\alpha$ and vary only α .

In order to generate spin echoes by means of Eq. (5.18) we need to introduce some sort of field inhomogeneity. This is done by averaging Eq. (5.18) over an ensemble of time-dependent fields that is calculated from the Fourier transform of the demodulated FID following the first pulse. The weight of each member of the ensemble is determined from the spectral amplitude at the frequency which corresponds to the ensemble member.

A corresponding simulation has been implemented in Python. We found that the measured spin echo intensities can best be understood by using $\alpha = 0.65 \pi/2$. For this angle the simulated intensities (evaluated every 1 μs) are shown in Fig. 5.12. Since the simulation assumed $T_2 = \infty$, we can attribute the losses in the echo intensity to the imperfections of

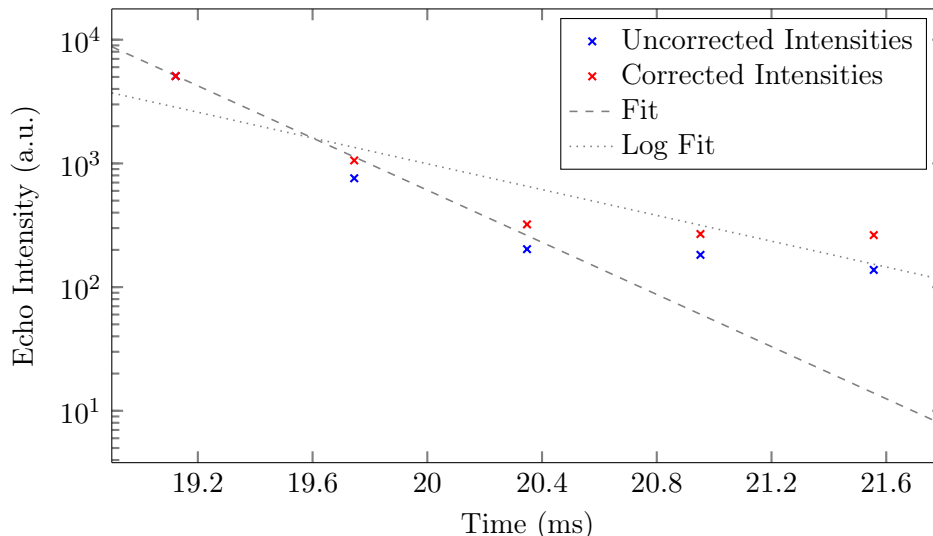


Figure 5.13.: Logarithmic plot of the uncorrected intensities (blue crosses) as obtained from the maxima of the FID and the four spin echoes shown in Fig. 5.10. The intensity decays rapidly towards the second echo; however for greater times the decay rate is much smaller.

the RF pulses.

We can take the imperfections into account by dividing the observed spin echo intensities (shown in Fig. 5.13) by the intensities of their simulated counterparts. The corrected data are shown as red crosses in Fig. 5.13. While even the corrected data do not fit a simple exponential decay $\sim \exp(-t/T_2)$, it can be seen that they increase the lower bound for T_2 . The dashed and dotted lines in Fig. 5.13 represent decays of the form $\exp(-t/T_2)$ with $T_2 = 412 \mu\text{s}$ and $T_2 = 833 \mu\text{s}$, respectively.¹² Although the underlying relaxation mechanism could be more complicated than simple exponential, it is likely that these values constrain the fastest time scale contributing to the relaxation.

5.6. Carr-Purcell sequence at 62 Tesla

Since the previously described experiment was performed at rather low field, the question arises, whether a similar experiment is also possible at the highest available fields. This is indeed the case.

5.6.1. Experimental

For the high-field experiment we used ^2H NMR on D_2O . With a carrier frequency of 407.0 MHz, the target field was approximately 62.3 Tesla. Using an RF power of 640 W, the $\pi/2$ - and π -pulses were approximated with $1 \mu\text{s}$ and $2 \mu\text{s}$, respectively. The duration

¹²The respective values are obtained by fitting (i) the data to $A \exp(-t/T_2)$ and (ii) the logarithm of the data to $A - t/T_2$. Clearly, the deviations between fit and data are both large and systematic so that the usual assumptions for the calculation of confidence intervals do not hold.

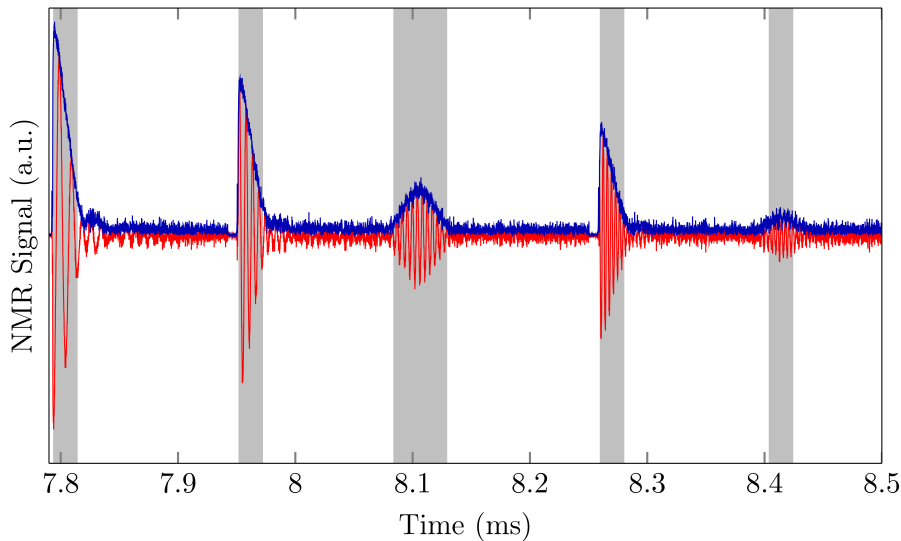


Figure 5.14.: Carr-Purcell sequence with two refocussing pulses at 62.3 Tesla.

between the first two pulses was approximately $150 \mu\text{s}$, the duration between the two π -pulses was $\approx 300 \mu\text{s}$. This sequence was repeated 20 times.

5.6.2. Results

In Fig. 5.14 we show the data obtained during the 9-th sequence. One can see from the echo decay that the lower bound for T_2 is approximately $200 \mu\text{s}$. Since we have recorded only two echoes, it is not possible to estimate the flip angle of the RF pulses.¹³ As we will show, one can still determine the field with sufficient precision to demodulate the data. Therefore, the method introduced in the context of the low field experiment should be applicable for the analysis of future data if more echoes are obtained or if the flip angle is known, e.g., from a calibration at low, static field.

5.6.3. Discussion

In order to determine the magnetic field we proceed as described in the previous section using the phase information from the data shaded in gray in Fig. 5.14. The obtained parameters from the fit are $B_{\text{max}} = 62.3224(2)$ Tesla, $t_{\text{max}} = 8.674(9)$ ms, and $\alpha = 769(11) \text{ s}^{-2}$.¹⁴

The obtained estimates are used again to demodulate the first FID as well as the echo signals. The demodulated signals are shown in Fig. 5.15(a-c). The demodulation works well at high fields; a correction of the echo intensities with respect to pulse imperfections should be possible provided the flip angles of the pulses are known.

Since we do not know the flip angles for the high-field experiment, we can only establish a lower bound for T_2 . The echo intensities determined as the maxima of the smoothed,

¹³In the previous chapter, the flip angle was estimated from the initial phase of all the FIDs. This method works reliably only if enough FIDs are obtained, i.e., at least 10.

¹⁴The shift in t_0 is due to a corresponding shift in the pre-acquisition delay.

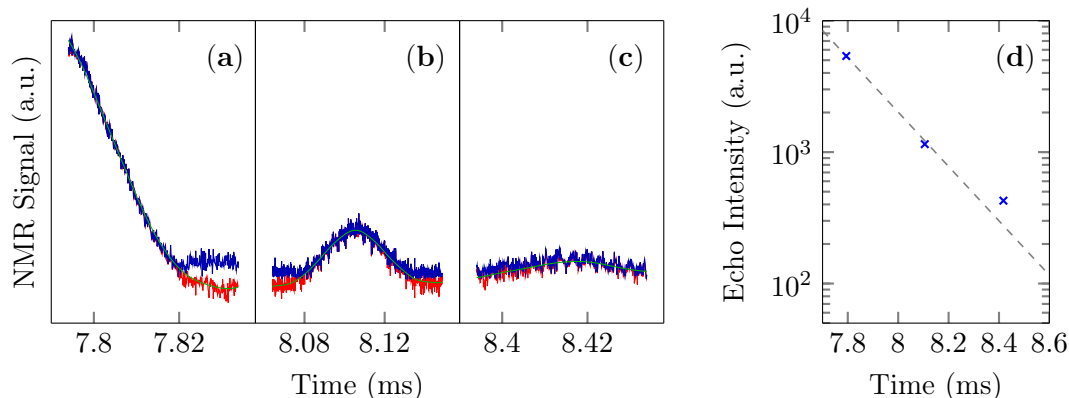


Figure 5.15.: (a - c) The same plot as Fig. 5.10 for the experiment at 62 Tesla. The modulation features have disappeared from the data. In (d) we plot the intensities of the echo signals as extracted from the smoothed curves in (a-c). The data have not been corrected for pulse imperfections and provide only a lower bound for T_2 . The dashed line is a guide to the eye with $T_2 = 210 \mu\text{s}$.

demodulated echoes are shown in a logarithmic plot in Fig. 5.15(d) along with a dashed line representing an exponential decay with $T_2 = 0.21 \text{ ms}$. While this is a relatively small lower bound, it is still more than an order of magnitude larger than the decay constant of the FID, T_2^* .

5.7. Measurement of the spin-lattice relaxation rate

In what follows we demonstrate the first measurement of the spin-lattice relaxation rate $1/T_1$ in a pulsed magnetic field. Such measurements are of basic interest also for the study of the PRE effect introduced in section 2.3. The data are analyzed in terms of a basic model: In a series of equidistant pulses of same length, the signal intensity after a given pulse is determined by the longitudinal magnetization prior to the pulse as well as the resonance offset of the pulse. Between two pulses the magnetization will recover with time constant T_1 . The model is expected to work well if the pulse distance is of the order of T_1 and if $T_2 \ll T_1$.¹⁵

5.7.1. Experimental

For our experiment we used the metal-organic framework (MOF) $\text{Cu}_3(\text{BTC})_2$.¹⁶ This compound has applications in gas storage, separation and catalysis. Moreover, it is possible to synthesize MOF compounds with a wealth of magnetic properties [46–48]. However, here we use the MOF only to demonstrate a first T_1 measurement. With $T_1 \sim 1 \text{ ms}$ and $T_2 \sim 30 \mu\text{s}$ at approximately 77 K, it complies to the above criteria.

¹⁵The condition $T_2 \ll T_1$ suppresses possible spin echoes which would contribute to the signal intensity.

¹⁶The compound was provided by Bettina Jee.

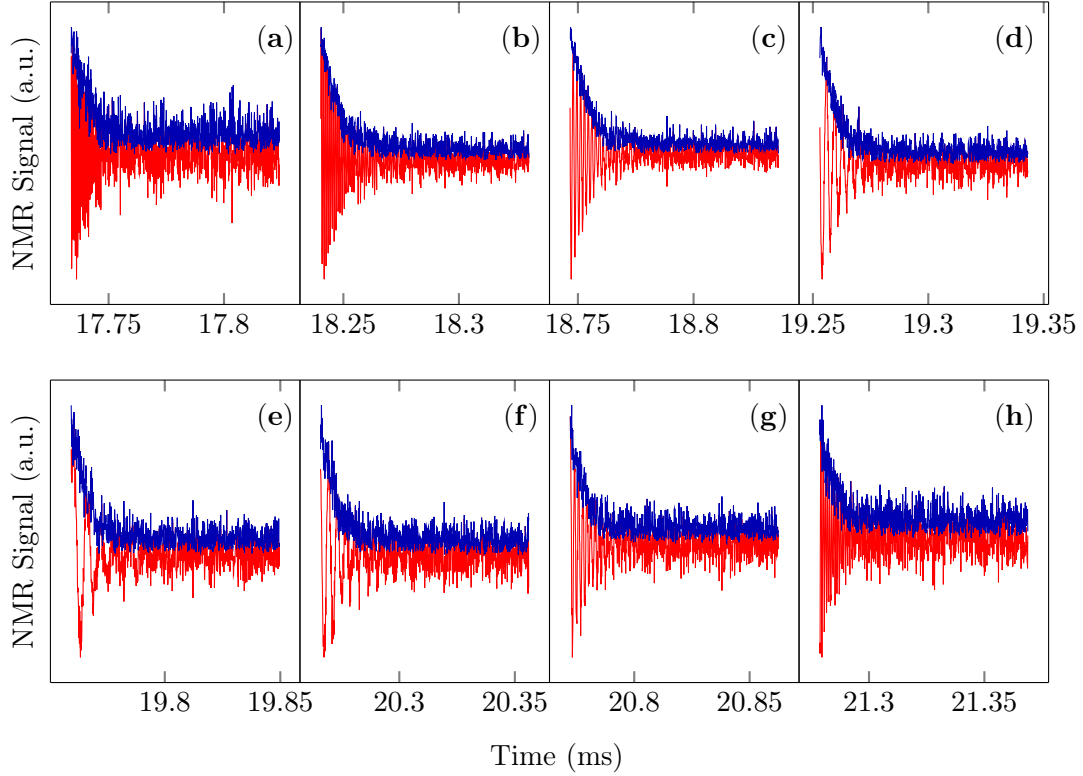


Figure 5.16.: Eight FIDs recorded in the vicinity of the field maximum. Since the signal-to-noise ratio is rather small, we plot each FID individually, from (a) to (h).

The resonance frequency of the circuit at the sample temperature of approximately 77 K was 478 MHz. At that frequency, a 300 ns pulse was applied every 505 μ s.

5.7.2. Results

The obtained data are plotted in Fig. 5.16. We obtained eight FIDs. The signal-to-noise ratio is good enough to fit the phase of the data.

5.7.3. Discussion

We fitted the phase information of the first 10 μ s of each FID. The parameter estimates for $B(t)$ are $B_{\max} = 11.43374(5)$ Tesla, $t_{\max} = 19.808(1)$ ms, and $\alpha = 815(2)$ s $^{-2}$.

The fit is used to demodulate the FIDs according to Eq. (4.19), i.e., only the modulations due to the change of the field during a given FID are removed. An exponential line broadening of 10 kHz is applied and each FID is Fourier transformed. The maximum of each spectrum gives both the intensity of the respective signal as well as the resonance offset at the time of the pulse.

The resonance offsets are plotted in Fig. 5.17(a), the measured intensities are plotted as blue line in Fig. 5.17(b). As can be seen from the plot, the intensity drops monotonically for times greater than 18.5 ms. This effect is due to T_1 , since the intensity losses due to

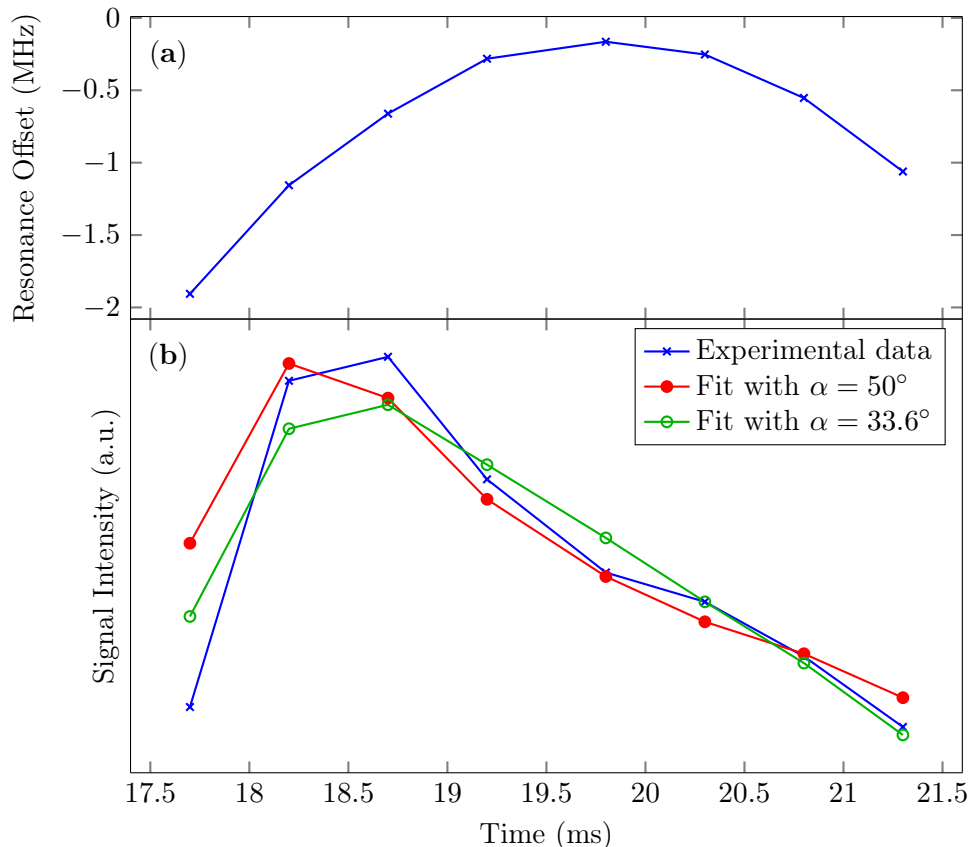


Figure 5.17.: (a) Resonance offset of the various pulses. The offset takes its minimum close to the field maximum. In (b) we show the measured intensities (blue line). We also plot two different fits obtained for two different flip angles α .

the resonance offset only are symmetric about the time of the field maximum.

In order to simulate the intensities, we proceed as follows: (i) For a given (on-resonant) flip angle, calculate the transversal and longitudinal magnetization after the first pulse, given the offset of the first pulse. (ii) Calculate the longitudinal magnetization prior to the next pulse assuming that the *difference* between equilibrium magnetization and magnetization right after the actual pulse recovers with T_1 . (iii) Calculate transverse and longitudinal magnetization after the *next* pulse and set this pulse to be the *actual* pulse. (iv) Continue from (ii) as long as pulses are left.

Note that this algorithm appears to the outside computing environment as a simple function so that least-squares methods can be used to minimize deviations between the output of the algorithm and experimental data. In Fig. 5.17 we also plot two intensity data sets obtained by “fitting” the algorithm to the experimental data assuming flip angles of 50° and 33.6° . The data are shown as green and red curves, respectively. The obtained T_1 values are 2 and 6.6 ms, respectively.

As the experiments with respect to T_1 and T_2 have shown, both quantities can be measured with pulsed field NMR. The precision with which parameters can be estimated

seems to be largely independent of the field amplitude but depends strongly on the accuracy with which the RF amplitude (i.e., the flip angle) is known.

6. Eigenmodes in the long-time behavior of a coupled spin system

In this chapter we set out to test a recent theory by Fine [6, 7], which describes the dynamics of a macroscopically large system of coupled quantum spins based on the notion of microscopic quantum chaos.¹ His challenging theoretical approach aims at establishing relationships that may hopefully help to improve our understanding of chaotic quantum systems, perhaps similar to how critical scaling lead to renormalization-group theory.

Addressing nuclear spins coupled via the magnetic dipole interaction, Fine predicts the long-time behavior of the spin correlation functions to be given by a set of exponentially decaying eigenmodes with *universal* complex exponents λ .

By boosting the available signal-to-noise ratio of the ^{19}F FID of solid calcium fluoride by two orders of magnitude beyond what was published so far, we could gain unique insight into the long-time behavior of a spin system that has served as test bed for the investigation of the dipolar interaction in solids since the beginnings of NMR itself. The increase in signal-to-noise ratio enables us, for the first time, to extract *two* decay modes from the experimental data. We furthermore demonstrate the universality of the first decay mode by a set of solid echo experiments.

Our findings are in support of Fine's theory that has implications beyond solid-state NMR, as we will discuss below.

Most of the work presented in this chapter will appear in Physical Review Letters, soon (expected in the April 20, 2012 issue, it is currently available at arXiv [8]).

6.1. Introduction

The measurement of the free induction decay (FID) is one of the simplest NMR experiments. Yet, a rigorous theory for the shape of the FID is often missing, especially if the number of interacting spins becomes macroscopic. In this case, one often analyzes the initial behavior of the FID using the method of moments [9], but it is not generally possible to derive an analytic expression for the entire FID. A special situation occurs if the FID is limited due to strong couplings between the spins and the surrounding bath (i.e. if its decay rate is given by $1/T_1$). This is often the case in liquids where the nuclear spins are coupled to a large thermal bath of motional degrees of freedom. At the same time, the

¹The work was performed in-between measurement periods at the Hochfeldlabor Dresden.

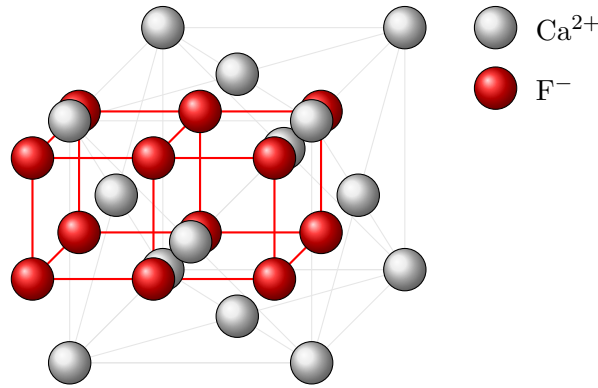


Figure 6.1.: Crystal structure of CaF₂: The calcium atoms (gray) form a face centered lattice; the fluorine atoms (red) are located on a simple cubic lattice.

rapid motion averages the inter-nuclear dipole-dipole interaction to zero so that the decay of the FID is exponential and given by T_1 . The situation can be described in terms of a separation of time-scales meaning that the FID evolves much slower than the underlying microscopic motion in the heat bath. Then a description in terms of a damped oscillator, giving rise to an exponential decay, is appropriate [6].

The situation is quite different in solids where the inter-nuclear dipole-dipole interaction often leads to a rapid decay of the FID although the system is still far away from thermal equilibrium (i.e., $T_2 \ll T_1$). In this case, the FID, as well as other spin coherences, are described by the spin-spin Hamiltonian. On general grounds one does not expect the FID to be exponential. Nevertheless, an exponential decay is often observed also in solids [49–52].

An ideal system for the investigation of the dipole interaction of a macroscopically large number of spins in solids is calcium fluoride, CaF₂. The crystal structure is shown in Fig. 6.1: The spin 1/2 fluorine nuclei are located on a simple cubic lattice, the calcium nuclei sit on a surrounding face centered cubic lattice. The only calcium isotope with spin (⁴³Ca, $I = 7/2$) has an abundance of only 0.1 % and a gyromagnetic ratio that is more than 10 times smaller than that of ¹⁹F enabling one to neglect the calcium nuclei. Clean crystals of CaF₂ are easily available² with a nuclear spin-lattice relaxation time T_1 of minutes, which practically leaves only one relevant time scale set by the dipolar coupling. Given the simple nature of the material and the challenging physics, there has been persistent interest in CaF₂ since the early days of magnetic resonance [9, 11, 13, 49–51, 53].

While most experimental and theoretical work focussed on the short-time behavior of the dynamics [13, 49, 54–56], two different theories have been put forward that treat the *long-time* behavior of NMR signals.

An early theory by Borckmans and Walgraef [14, 15] tries to account for the long-time behavior using a memory function approach. Briefly, in the memory function approach the

²CaF₂ is frequently being used as window material for infrared and ultraviolet light.

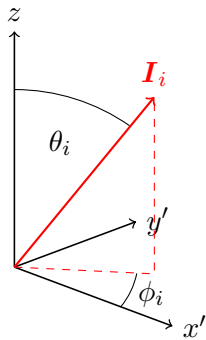


Figure 6.2.: With its tip on the surface of the unit sphere, the i -th spin is described by polar and azimuthal angles ϕ_i and θ_i in the rotating frame, cf. Fig 2.1.

FID $G(t)$ is given by

$$\frac{dG}{dt} = - \int_0^t F(\tau) G(t - \tau) d\tau, \quad (6.1)$$

where $F(t)$ is the memory function. The problem is therefore shifted to the computation of the memory function for which rigorous theory is missing. Only under certain assumptions (e.g., that the memory function is Gaussian), an exponential long-time behavior is obtained.

6.2. Description in terms of chaotic dynamics

Here, we test a very different, recent theory by Fine [6, 7] that associates the long-time behavior of the system with underlying, microscopic quantum chaos. Starting from an ensemble of classical spins, he predicts the final long-time behavior of the FID as well as that of spin echoes to be given by

$$G(t) \simeq e^{-\gamma t} \cos(\omega_1 t + \phi). \quad (6.2)$$

where special cases with $\omega_1 = 0$ may exist. We will now sketch very briefly the derivation of Eq. (6.2), and refer to [6] for more details.

The dynamics of a lattice of *classical* spins can be described by a set of angles $\{\phi_i, \theta_i\}$ where the i -th pair of coordinates describes the orientation of the i -th spin with its tip on the surface of a sphere that has the spin at its center (cf. 6.2). As ϕ_i and θ_i vary in time, a trace on that sphere is obtained. In case of a dipole coupled system the equations of motion controlling the time evolution of the system are nonlinear. For a large number of spins this eventually leads to a phase space that is dominated by chaotic regions. While a Markovian description of such a system is usually applicable only for times much larger than the mean free time, this is not the case for ensemble averaged quantities [57]. The situation is analogous to that of an ensemble of random walkers. If each walker performs a few steps one can calculate with precision only the mean distance $\sqrt{\langle l^2 \rangle}$ traveled by the ensemble of walkers.

An ensemble of spins can therefore be described in terms of Brownian motion as soon as the spin system has lost memory of its initial configuration. Thus, the long-time behavior of the ensemble averaged quantities can be obtained by solving a correlated diffusion equation on the surface of a sphere [6].

This approach is to be contrasted with chaotic dynamics of the magnetization in liquids, studied e.g. in [58, 59]. Here, the local field generated by the distant dipole field as well as the so called radiation damping field may cause a *turbulent* behavior of the macroscopic magnetization.³ While chaotic dynamics in liquids are discussed in an entirely classical picture, the microscopic diffusion concept for solids has been generalized to quantum spins by Fine [6, 7]. Fine predicted a *universal* long-time behavior of the FID and the decay after a spin echo.

We would like to stress that, in contrast to classical systems, no generally accepted definition of quantum chaos is available up to date. Often, quantum systems are associated with chaos if the energy splittings are described by a Wigner distribution.⁴ In Fine's theory, the quantum nature of the problem is taken into account by considering trajectories in the parameter space of the system's density matrix instead of trajectories of the set of angles $\{\phi_i, \theta_i\}$ introduced above.

To summarize Fine's conjecture, for a system of spins 1/2 on any Bravais lattice with the dipolar Hamiltonian

$$\mathcal{H}_{\text{dip}} = \frac{\gamma_n^2 \hbar^2}{2} \sum_{j,k}^N \left[\frac{\mathbf{I}_j \mathbf{I}_k}{r_{jk}^3} - \frac{3(\mathbf{I}_j \cdot \mathbf{r}_{jk})(\mathbf{I}_k \cdot \mathbf{r}_{jk})}{r_{jk}^5} \right], \quad (6.3)$$

in a strong magnetic field (so that only the secular part has to be retained, cf. section 2.2) the long-time behavior is given as a sum of exponentially decaying eigenmodes with exponents $\lambda_\sigma = \gamma_\sigma + i\omega_\sigma$, that is,

$$G(t) \simeq \sum_{\sigma} e^{-\gamma_\sigma t} \cos(\omega_\sigma t + \phi_\sigma). \quad (6.4)$$

Note that this expression reduces to the *final* long-time behavior of Eq. (6.2) after sufficiently long times.

The decay modes in $G(t)$ follow from a set of solutions of a correlated surface diffusion equation $f_\sigma(t, x) = e^{-\lambda_\sigma t} u_{\lambda_\sigma}(x)$, where $\lambda_\sigma = \gamma_\sigma + i\omega_\sigma$ is an in general complex eigenvalue of the integro-differential operator associated with the modified diffusion equation, and $u_\lambda(x)$ denotes its corresponding eigenfunction. In particular, the conjecture proposes that λ_σ does not depend on the initial configuration of the spin system. It was argued by Fine [6]

³The precessing magnetization induces a current in the NMR coil; the corresponding field acts back on the magnetization establishing a possibly powerful positive feedback.

⁴The Wigner distribution

$$\rho(x) = \frac{\pi x}{2} \exp\left(-\frac{x^2}{4\pi}\right)$$

is obtained e.g. for the eigenvalue splittings in large random matrices as they are encountered in random matrix theory, see e.g. [60].

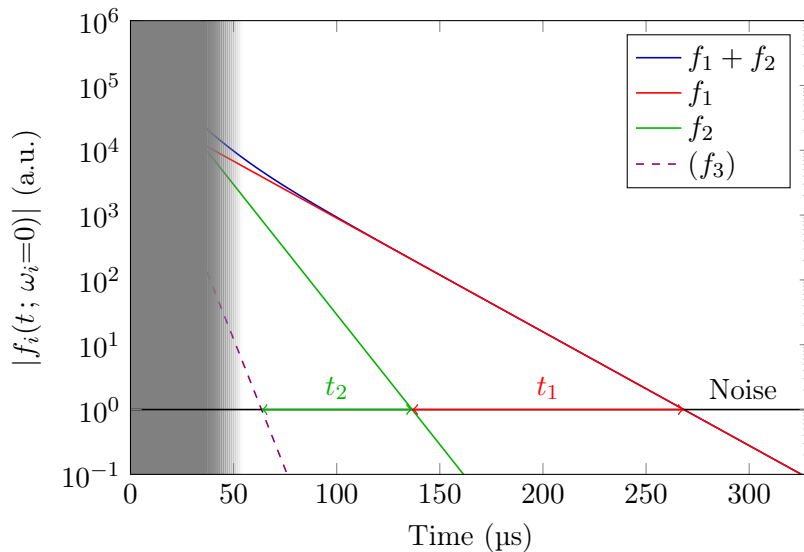


Figure 6.3.: Sketch of the eigenmodes f_i and the sum $G(t)$ in Eq. (6.4). For clarity, we ignore the oscillating part, i.e. $\omega_i = 0$. The plotted modes have amplitude and slope as observed in our experiment for the applied magnetic field parallel to (110). Since the description in terms of eigenmodes is only valid after chaos has developed, we have shaded the first 50 μs ($\sim 3T_{2G}$) with a fading between $2T_{2G}$ and $3T_{2G}$. The dashed line indicates a possible third mode which has a slope of two times that of the second mode and a similar amplitude.

that due to the Markovian nature of ensemble averages [57] one expects not only the decay constant of the slowest mode ($\sigma = 1$) to be of the order of the inverse decay time, i.e., $\gamma_1 \sim 1/\tau$, but also the difference to the second slowest exponent should be of the order of $1/\tau$, i.e., $\gamma_2 \sim 2\gamma_1$. There are no predictions for ω_2 .

In related work, the long-time behavior is referred to as that part of the FID that is determined by the slowest mode only (i.e., given by (6.2)). In the experiment, this description holds after the second slowest mode has disappeared in the noise. Thus the beginning of the long-time behavior would be set by the noise level. In this work we consequently consider the long-time behavior to correspond to that part of the FID where chaos has developed, i.e., the part that is given as the sum of all modes. We refer to the time window t_1 , cf. Fig. 6.3, as *final* long-time behavior. Here, the decay can be described by the slowest mode only. From Fig. 6.3 one can see that the number of *detectable* modes is set again by the signal-to-noise ratio. Note that we have dropped in Fig. 6.3 the cosine function for clarity. We have also hypothesized in Fig. 6.3 on a possible third mode with an amplitude between that of the first and second mode and with a slope that is two times that of the second mode. Clearly, for a frequency ω_3 anywhere close to the values obtained for ω_1 and ω_2 such a mode cannot be detected within our experiment since one needs a time t_n approximately $\omega_n/2\pi$ in order to determine the n -th mode (the values for ω_1 and ω_2 are determined below and summarized in Tab. 6.2 at the end of this chapter).

While the early work of Engelsberg and Lowe [50] is in reasonable agreement with Fine's

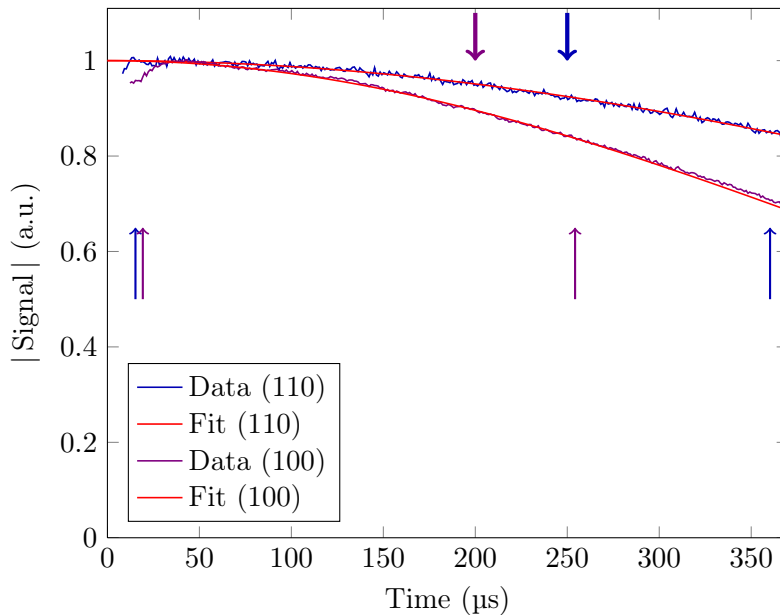


Figure 6.4.: ^{19}F FIDs of C_6F_6 for samples with geometries close to our CaF_2 sample for B parallel (110) and (100), plotted as blue and magenta lines, respectively. Each FID was fitted to a Gaussian in the time windows indicated by the blue and magenta pairs of upward arrows. We found $\sigma = 632(3)\ \mu\text{s}$ for the (110) direction and $426(3)\ \mu\text{s}$ for the (100) direction. The thick downward arrows show the last points in time relevant for the fitting procedure of the calcium fluoride data (discussed below). At these points, the intensity corrections amount to 8 % for the (110) direction and 12 % for the (100) direction.

theory, it is inconclusive with regard to his more concrete predictions discussed above. Therefore, Fine's work triggered new experiments with hyperpolarized polycrystalline solid xenon for better signal-to-noise ratio [52] and CaF_2 [51]. The experiments showed that the final long-time behavior is indeed universal since it does not depend on various initial preparations of the spin system, in agreement with Fine's theory. However, only a single mode λ_1 in the exponential decay was found. In solid xenon, the isotropic averaging over all crystal orientations makes the direct observation of an isolated second mode unlikely [61].

Within this thesis we were able to increase the SNR of the FID by two orders of magnitude over previously reported experiments. As a consequence, it is possible to resolve a second decay mode in agreement with Fine's predictions [6, 7]. Our results thus favor his theory over other theories using a memory function approach [15] since these predict only a single mode. Prior to our discussion of the FID we will give a brief account of spin echo measurements that demonstrate the universality of the first decay mode. Similar experiments with lower SNR have been performed by Sorte et al. [51].

6.3. Experimental

The $5 \times 5 \times 10 \text{ mm}^3$ CaF_2 crystal was obtained from Mateck, Germany. Impurities are stated to be below 2 ppm. The crystal was oriented by X-ray diffraction.⁵ A home-built NMR probe was used in order to align the crystal's axes (110) and (100) parallel to the applied magnetic field (7.06 T), respectively. The probe was set to a resonance frequency of 283.383 MHz and operated at 20 K. The quality factor Q of the resonance circuit was 240, the $\pi/2$ pulse length was 5 μs . The decay was sampled with 1 MS/s. The T_1 at 20 K was determined to be 76 s.

With typically 80 scans our maximum SNR for the FID measurements was about 10^6 . In order to record the signal, various attenuations were used to prevent the preamp from saturating and to allow for an appropriate loading of the 16 bit digitizer. Additionally, the first 20 μs were measured using a spin locking sequence [62]. Finally, the tail of the FID was measured with the variable attenuator set to zero but still in front of the preamp to minimize additional phase shifts. The procedure was first performed for the applied magnetic field B parallel to the (110) direction of the crystal and then repeated for B parallel (100).

We also performed 10 solid echo measurements for B parallel to the (110) direction with pulse separations between 49 to 146 μs . Since the echo data are analyzed only in terms of the slowest mode only, we measured it without attenuation and analyzed only those parts of the signal that did not saturate the digitizer.

In order to determine and remove the influence of the inhomogeneous magnetic field on both, echo decay and FID, we measured a ^{19}F FID on a C_6F_6 sample (intrinsic $T_2 \gg 1 \text{ ms}$, compare also section 5.3) of about the same volume and geometry as the crystal. The data are shown in Fig. 6.4. On the time-scale of the CaF_2 FID the ^{19}F decay could be approximated by a Gaussian with a standard deviation of 632(3) μs and 426(3) μs for (110) and (100) parallel B , respectively. The CaF_2 data were hence multiplied with a rising Gaussian function to remove the inhomogeneous broadening. Although this procedure increases the noise level towards the end of the FID, this is a very minor effect with a correction of only 8 % for the data point at 250 μs .

Since the linewidth hampers a precise determination of the exact resonance frequency by means of a simple Fourier transform, the actual offset was determined by analyzing the time dependence of the phase $\phi(t)$ of the complex valued FID. For B parallel (110) the offset of 700 Hz was removed from both FID and echo data. Phase changes due to the variable attenuator were taken into account.

⁵We thank C.P. Dietrich for performing the XRD measurements.

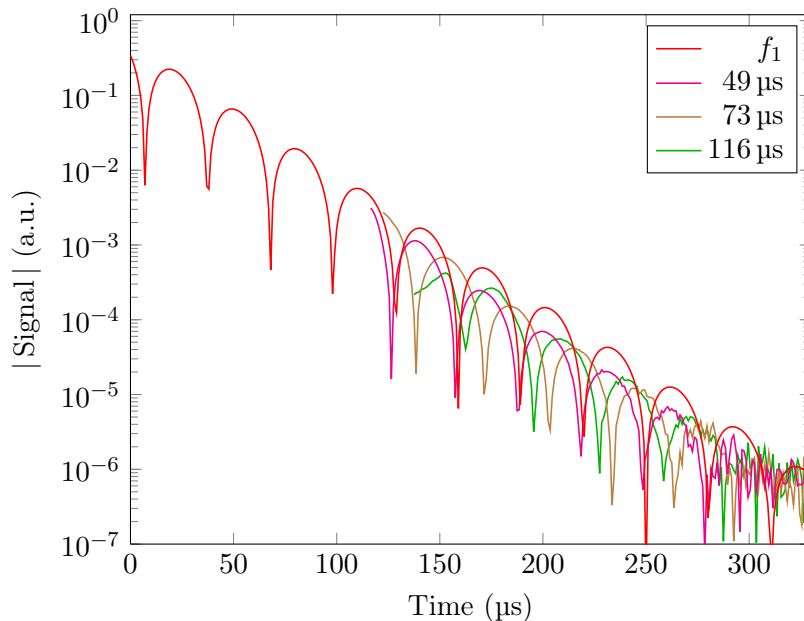


Figure 6.5.: Magnitude of the NMR signal's real part following a solid echo sequence for B parallel (110) for various pulse separations τ , given in the legend. Note that the sharp peaks simply correspond to zero-crossings of the cosine in Eq. (6.2). For short pulse separations the saturated part of the echo is not shown. The red curve f_1 shows the expected long-time behavior calculated with Eq. (6.2). The parameters for λ_1 are those from a fit described in section 6.4.2.

6.4. Results

6.4.1. Solid echoes

We begin with the description of solid echo experiments since the analysis in terms of only the slowest decay mode is a little less involved than that of the FID.

In Fig. 6.5 we show three echoes with pulse separations of $49 \mu\text{s}$, $73 \mu\text{s}$ and $116 \mu\text{s}$. The saturated part of the echoes is not shown. All echoes are corrected for the inhomogeneous decay and a small offset of 700 Hz . After the offset correction, the NMR signal is entirely in the real part, so that we plot the magnitude of the real part only. This reduces the noise in the data and furthermore allows us to fit the real part of the NMR signal to Eq. (6.2) as discussed below. We also plot in Fig. 6.5 the first decay mode with eigenvalue $\lambda_1 = \gamma_1 + i\omega_1 = 40.3 \text{ kHz} + i103.5 \text{ krad/s}$ as determined by a fit to FID data performed in the following section.

The meaning of the universality of the long-time behavior, is as follows: Independent of the preparation of the system (i.e. the pulse distance), the final long-time behavior of the signals is given by Eq. (6.2). It is universal in the sense that $\lambda_1 = \gamma_1 + i\omega_1$ is the same for all echoes, only ϕ_i and the amplitudes may differ.

It can be seen from Fig. 6.6 that the universality of Eq. (6.2) indeed holds. Here, we plot all echoes shifted in time and scaled in amplitude to match the FID. The shifted

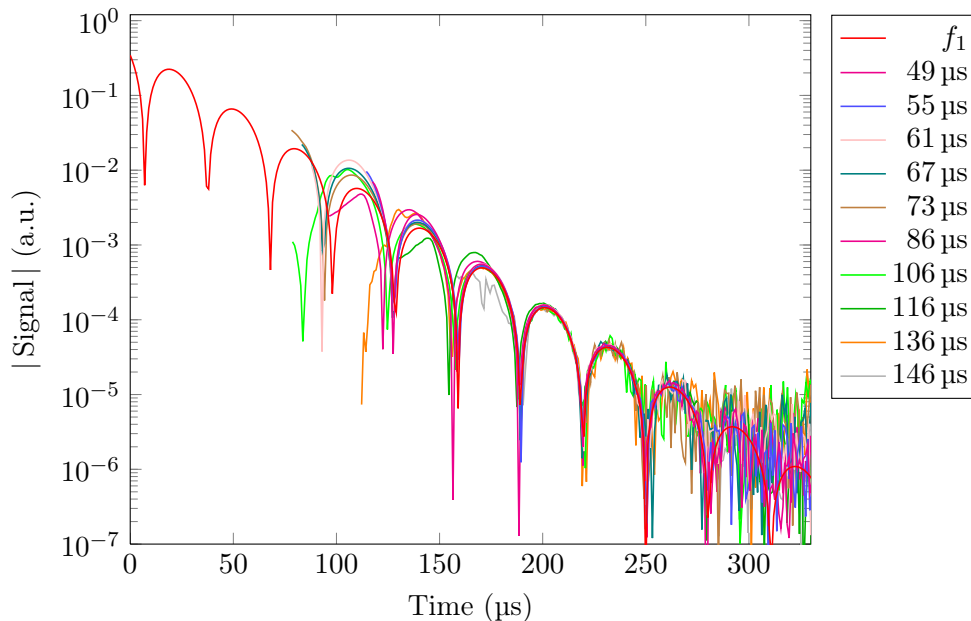


Figure 6.6.: A more complete dataset than in Fig. 6.5. Here, the echoes were shifted in time and rescaled in amplitude to match the decay mode f_1 (red curve).

and rescaled data overlap for times greater than $190 \mu\text{s}$, revealing that the echoes' final long-time behavior is characterized by the same slope (γ_1) and frequency (ω_1). In order to quantify the overlap we separately fitted each shifted echo in the time interval 190 to $250 \mu\text{s}$ (using again the Levenberg-Marquardt algorithm as discussed in section 4.2). From each fit we obtain a value for ω and one for γ . We summarize the data by giving the mean of all ten echoes as a parameter estimate and two standard deviations as an error estimate. The result then is $\omega_1 = 102(7) \text{ krad/s}$ and $\gamma_1 = 39(11) \text{ krad/s}$, i.e., the obtained results overlap closely with those of the FID (λ_1).

While this is the first experimental quantification on the universality of Eq. (6.2) for CaF_2 (Sorte et al. have reported echoes like those in Fig. 6.6 in [51], but they did not fit the echoes independently), the error in ω_1 and γ_1 is quite large. We therefore decided to perform the FID measurements on which we focus in this chapter.

6.4.2. Free induction decay

The obtained FID data, measured with various attenuations as well as a spin-locking sequence, are plotted in Fig. 6.7. Instead of real and imaginary part (IQ data) we plot in Fig. 6.7(a) the magnitude of the real part and in 6.7(b) the phase ($\text{atan2}(Q, I)$, cf. section 4.3). We also plot data for the beginning of the FID obtained using a spin locking sequence as described in [62].

As expected, the NMR signal in Fig. 6.7(a) decreases with increasing attenuation. The phase information in Fig. 6.7(b) furthermore reveals an ascending trend that can be removed from the data by multiplying the signal with $\exp(-i\Delta\omega t)$, where $\Delta\omega$ is the resonance

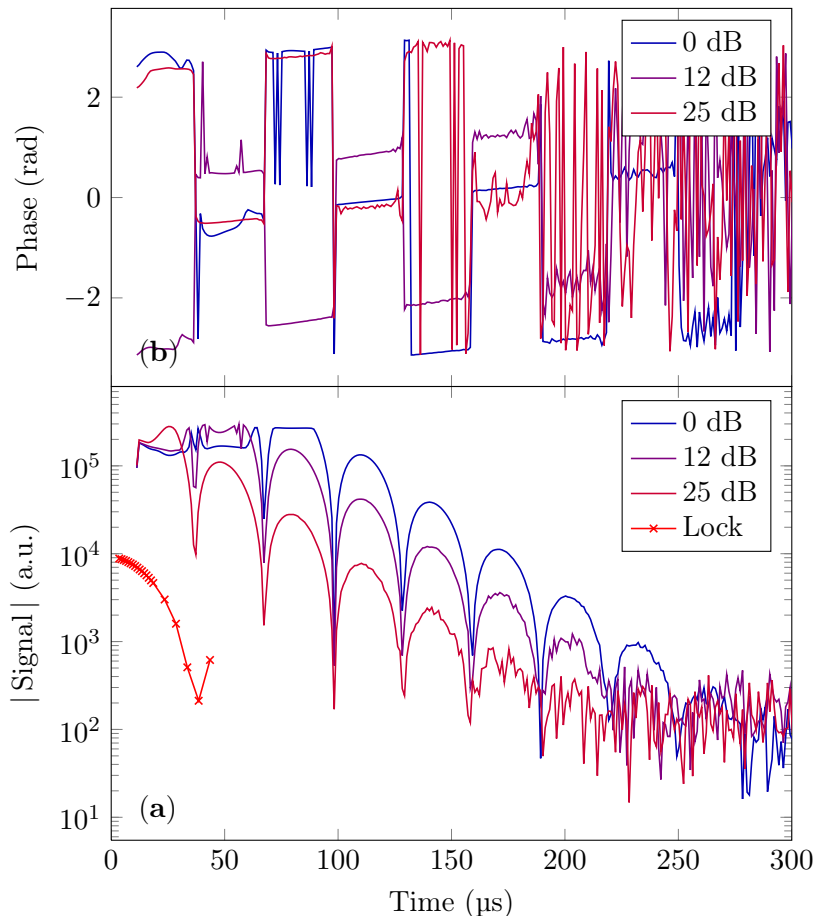


Figure 6.7.: Magnitude (a) and phase (b) of NMR signals recorded with the three attenuator settings given in the legend. Apart from a normalization by the number of scans, no signal conditioning was performed. The lower the attenuation, the earlier the digitizer is overloaded or the preamp is saturated. The ascending trend in the phase information reveals a small remaining offset of 700 Hz.

offset. (The phase is again given by Eq. (4.4). However, here the resonance offset is constant). Note also how the phase starts to fluctuate as soon as the corresponding data reach the noise level.

In order to analyze the FID over several orders of magnitude we need to compile the various datasets into a single FID. This is done as follows:

(i) Amplitude correction. We keep the trace recorded with 0 dB constant and multiply first the trace of the 12 dB signal with a factor A (see A in Tab. 6.4.2). Then we multiply the 25 dB signal and finally the Lock data.

(ii) Offset correction. We multiply the complex valued traces (individual signals) with $\exp(-i\Delta\omega t)$ and manually tune $\Delta\omega$ so that the linear shift in time in Fig. 6.7(b) vanishes. Thus determined values $\Delta\omega$ can be found in Tab. 6.4.2.

(iii) Phase correction. We multiply the various traces with $\exp(-i\phi_0)$ with ϕ_0 determined such that the contributions in the imaginary part of the NMR signal are minimized.

The combined effect of offset correction and phase correction can be seen in Fig. 6.8.

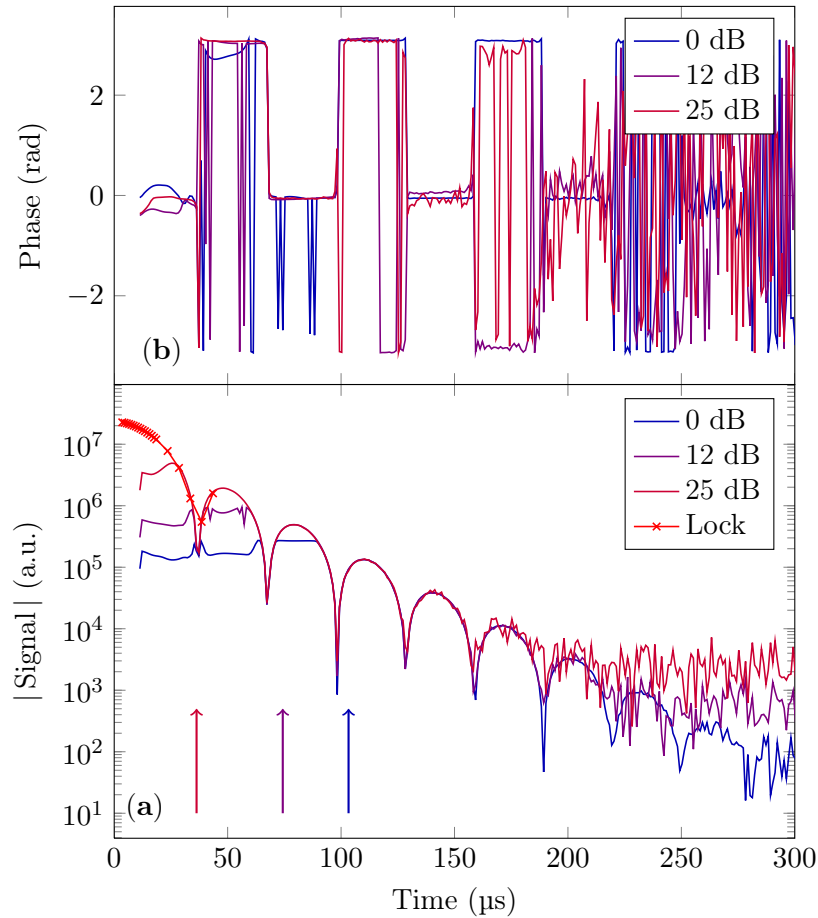


Figure 6.8.: Magnitude (a) and phase (b) of NMR signals shown in Fig. 6.7 after correction for Amplitude, offset and phase. The arrows in (a) indicate the points at which two different datasets are joined for the final FID. Right of the blue arrow we take the blue (0 dB) data, between magenta and blue arrow we take the 12 dB data, etc. The plot of the phase in (b) reveals that the NMR signal is in the real part only since the phase changes between 0 and $\pm\pi$.

The curves measured with different attenuations overlap for about two beats. The phase information shown in Fig. 6.8(b) reveals that the signal is in the real part only. The used values for A , ϕ_0 and $\Delta\omega$ can be found in Tab. 6.4.2 where we also give the numbers for the corrections of the other data set taken for B parallel to the (100) axis of the crystal. From the corrected data a single FID is obtained by slicing the traces at the positions indicated by the upward arrows in Fig. 6.8(a). This single FID is subsequently multiplied with a rising Gaussian to compensate for the field inhomogeneity (as measured in section 6.3) and normalized. The resulting signal is shown in Fig. 6.9.

6.5. Discussion

We first discuss the data in Fig. 6.9. We find good agreement with Engelsberg and Lowe for times accessible within their experiment, i.e., up to 150 μs , cf. gray curve in Fig. 6.9.

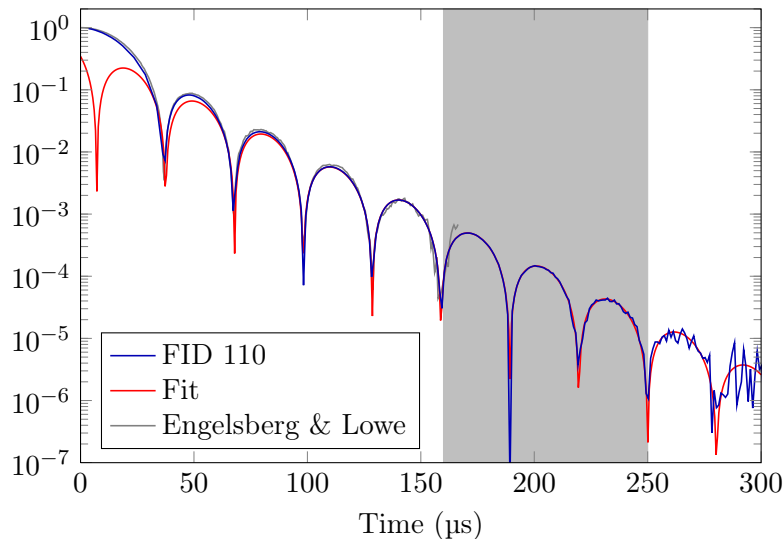


Figure 6.9.: The data is in good agreement with Engelsberg and Lowe’s measurements but has nearly three orders of magnitude better signal-to-noise ratio. Due to the higher signal-to-noise ratio, we were able to fit the FID to Eq. (6.2) in the time frame 160 to 250 μs (shaded in gray).

The red line in Fig. 6.9 is a fit according to Eq. (6.2) based on our decay between 160 and 250 μs using again the Levenberg-Marquardt algorithm as implemented in Matlab, cf. section 4.2. The particular window for the fit was chosen since we may expect a faster second mode, but the algorithm should also not operate in low signal-to-noise ratio. We verified that a slight change in the starting point did not change the obtained fit parameters significantly. The obtained values are given as (110) λ_1 in Tab. 6.2 at the end of the chapter. We find a significant deviation between the real part of our value ($\gamma_1 = 40.3 \text{ ms}^{-1}$) and the ones determined from Engelsberg and Lowe’s data, but also those by Sorte et al.

Orientation	Attenuation (dB)	ν (MHz)	$\Delta\omega/2\pi$ (kHz)	ϕ_0 (rad)	A
(110)	0	282.383	0.7	2.597	17.5122
	12	282.383	0.7	2.497	3.1915
	25	282.383	0.7	3.493	1
	Lock	282.383			2578
(100)	0	282.380	3.6	0.08	18.1484
	12	282.380	2.9	0.255	3.5133
	25	282.380	0	0.355	1
	Lock	282.380			25.5

Table 6.1.: Parameters for the correction of the various traces. We also show the corresponding data for the (100) direction. Small variations in the resonance offset $\Delta\omega/2\pi$ for the (100) orientation are attributed to the temperature dependent susceptibility of the cryostat.

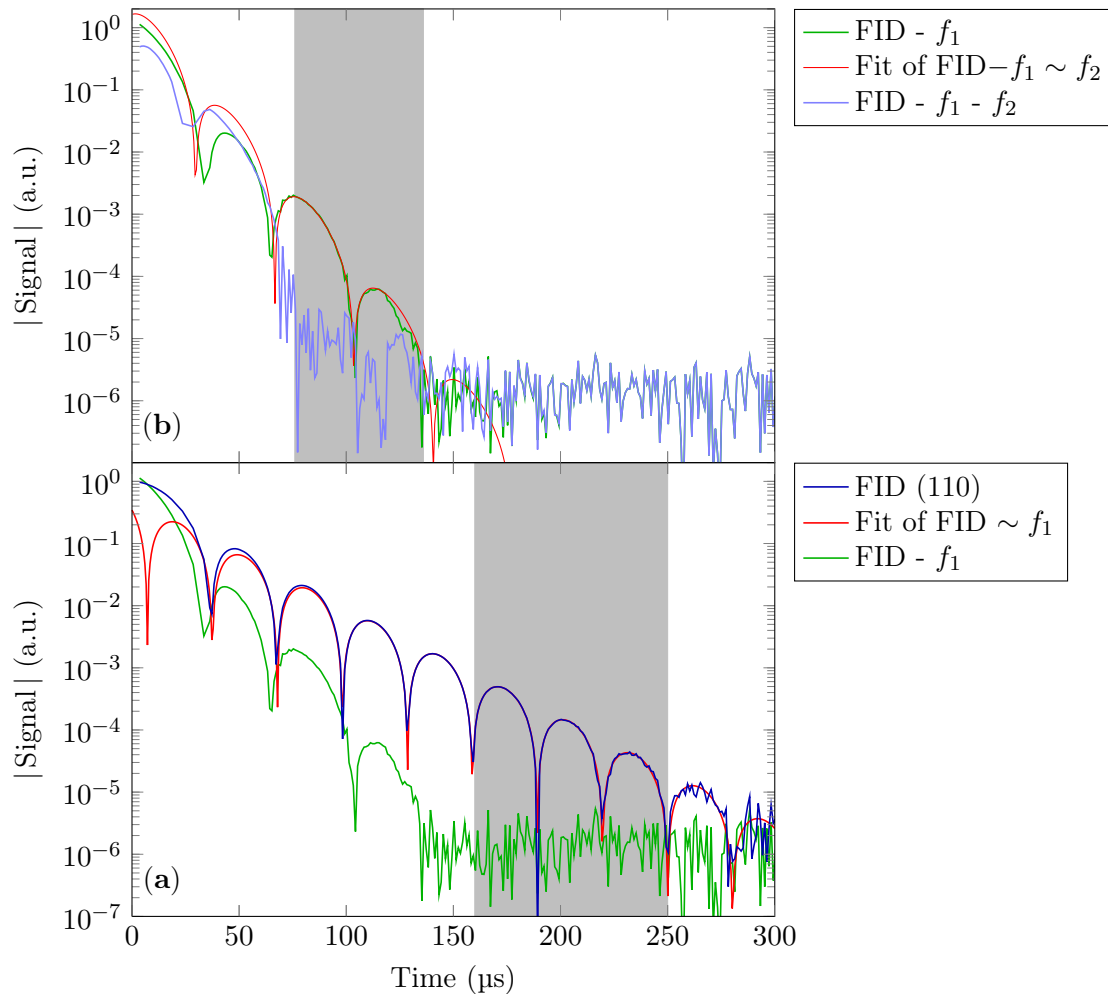


Figure 6.10.: Extraction of two decay modes from the FID for B parallel to (110). (a) After subtracting the fit or first Mode f_1 as determined by fitting the tail of the FID (cf. Fig. 6.9) to Eq. (6.2) in the time interval $160 \mu\text{s}$ to $250 \mu\text{s}$, a second mode f_2 becomes apparent. This mode is replotted in (b) along with a fit according to Eq. (6.2) in the time interval 76 to $136 \mu\text{s}$ (shaded in gray). The fit reveals that the decay constant γ_2 of the second mode is about a factor of two larger as compared to the first mode while the obtained value for ω differs rather slightly from the first mode's one. The light blue line is left after subtracting both modes from the FID and reveals that within experimental resolution the FID is accurately described by $f_1 + f_2$ for times greater than $75 \mu\text{s}$ or for a decay over four orders of magnitude.

($\sim 43 \text{ms}^{-1}$). We also note a substantial difference between the fit (red line) and the data for shorter times. It is precisely this difference between fit and signal that explains the deviation between our value for γ_1 and the values obtained from earlier measurements. The difference can be understood in terms of a second addend or eigenmode in Eq. (6.4) as we will now show.

We replot the FID together with the fit in Fig. 6.10(a). This time, we also plot the difference (green line) between the actual decay and the fit to the long-time decay (first mode f_1). Clearly, the green curve in Fig. 6.10(a) is strong evidence for Fine's second mode

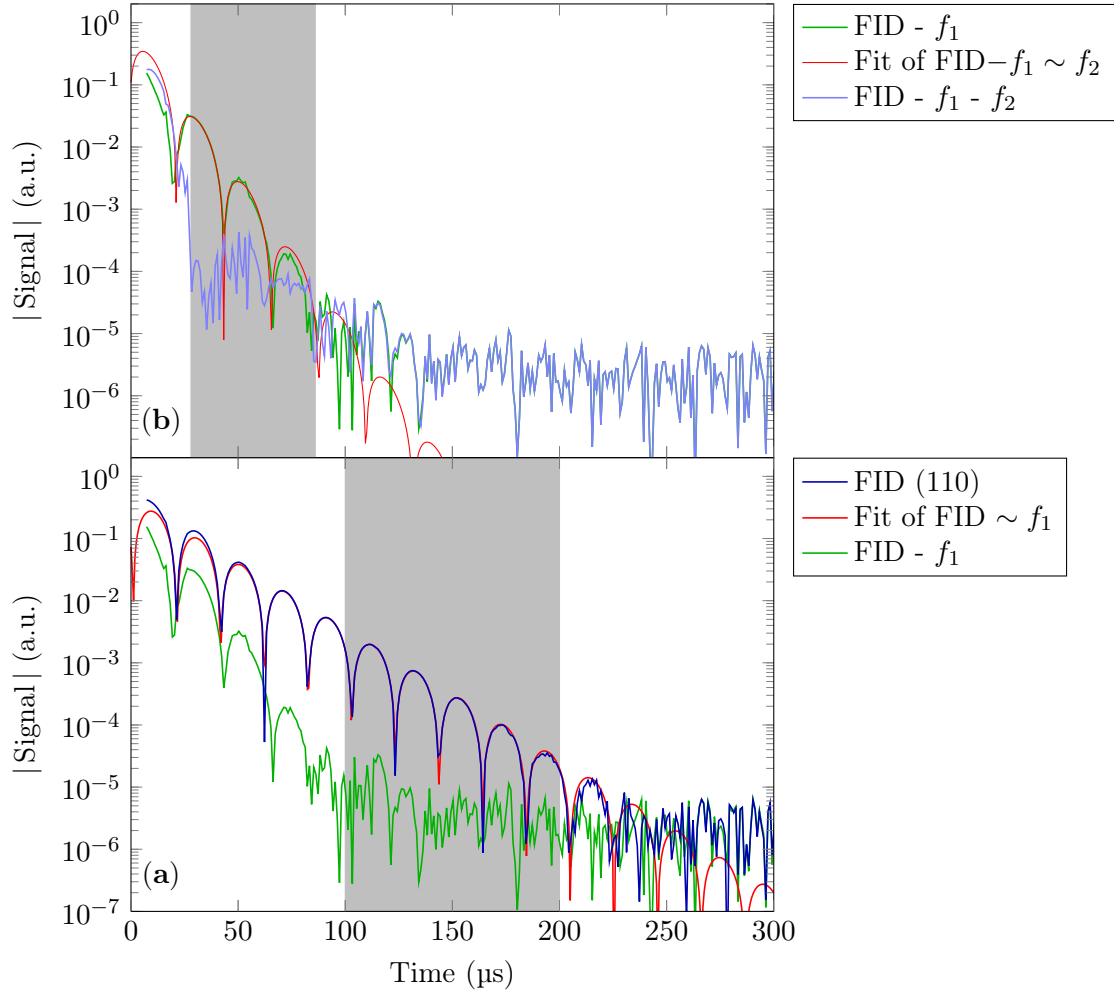


Figure 6.11.: The same plot as in Fig. 6.10 but for B parallel to (100). The FID (a) is again measured with different attenuations; the first 23 μs are measured using a spin locking sequence, the time intervals 24 to 51 μs and 52 to 111 μs are measured with 25 and 12 dB, respectively. A Gaussian line narrowing of 426 μs was applied to remove the influence of the field inhomogeneity. The fit of the first mode f_1 is performed in the time interval 100 to 200 μs . The residue, shown as green line in (a), reveals that in this time interval the data are well described by a single mode and again show oscillatory decaying behavior for earlier times. (b) This oscillatory behavior can well be described in terms of a second mode f_2 , extracted in the time interval 28 to 86 μs .

since it is approximately exponential with a decay rate of roughly $2\gamma_1$ (it disappears in the noise at about 140 μs while the first mode has disappeared at 300 μs). Note that this result could not have been obtained by earlier measurements due to the lower signal-to-noise ratio that did not permit a fit at sufficiently long times.

The parameters of the second mode (green curve) in Fig. 6.10(a) are estimated from a fit to Eq. (6.2) between 75 and 135 μs , shown as red curve in Fig. 6.10(b). The blue curve in Fig. 6.10(b) shows the residuum, revealing that the FID can be described accurately in terms of two modes for times greater than 70 μs . The estimates for the second mode are given as (110) λ_2 in Tab. 6.2.

Orientation	Mode	Data Type	A	ϕ (rad)	ω (krad/s)	γ (kHz)
(110)	λ_1	Engelsberg	–	–	101.9(5)	43.0(1)
	λ_1	Sorte	–	–	106.2(19)	43.3(1)
(110)	λ_1	start values	34537	0.38124	103.372	40.409
	λ_1	fit results	51179(1992)	0.83(2)	103.5(2)	40.3(2)
	λ_2	start values	439596	1.3674	100.298	70
	λ_2	fit results	299333(70630)	5.3(1)	85(1)	92(3)
(100)	λ_1	start values	1000000	0.38124	103.372	50409
	λ_1	fit results	905566(27585)	4.55(2)	154.0(2)	48.4(3)
	λ_2	start values	1000000	0.508956	96.298	70
	λ_2	fit results	1582961(90644)	4.85(6)	142(2)	109(2)

Table 6.2.: Fit results and starting values of the fit algorithm for both orientations and the first two modes λ_1 and λ_2 . We also show values obtained from a fit to Engelsberg and Lowe’s data as well as values reported by Sorte et al. [51]. The starting values are given exactly as they are passed to the fitting routines, irrespective of significance of all the digits.

While we are convinced that the green curve in Fig. 6.10(a) is evidence for Fine’s second mode, we decided on an independent check, i.e., the measurement of the FID of CaF_2 for a different orientation of the crystal with respect to the applied magnetic field. The experimental data for the various attenuations are given in the appendix in Figs. A.1 and A.2, analogous to Figs. 6.7 and 6.8.

The composed FID and its analysis are given in Fig. 6.11. Due to the dependence of the secular part of the dipolar Hamiltonian on the orientation of the applied magnetic field, different shapes of the FID are obtained for different orientations, cf. section 2.2. For the (100) orientation the FID decays faster and oscillates at a higher frequency. The data can again be understood in terms of two modes with the decay rate of the second mode being about two times larger than the rate of the first mode. The fit results for both modes are given in Tab. 6.2.

6.6. Conclusion

We have studied the long-time behavior of a macroscopic system of dipole coupled spins $1/2$. The data are interpreted in terms of Fine’s theory that is based on the notion of microscopic chaos. While earlier work is in agreement with this theory, only a single decay mode could be found. Therefore, it is difficult to discriminate between other theories that use a memory function approach.

By increasing the signal-to-noise ratio by two orders of magnitude compared to published accounts, we can determine the first decay mode with high accuracy. After subtracting this mode from the FID we are left with a second universal decay mode that decays about two

times faster than the first mode. Our findings thus support Fine's theory that predicted a well-isolated second decay mode and correctly estimated the difference between the decay rates of the first and the second mode.

Finally, we would like to mention that the obtained values for λ_1 and λ_2 are related to the moments of the FID via the truncated dipolar Hamiltonian. To date, it is not possible to derive the measured eigenvalues from first principles, only rough estimates for the real parts are available.

One may hope that future experimental and theoretical work will eventually enable one to predict the observed eigenvalues from the Hamiltonian of the system. Such a prediction could also contribute further to our understanding of quantum chaos.

7. Conclusion

Within this thesis, we were concerned with NMR measurements in pulsed high magnetic fields up to 62 Tesla. We believe the work is a significant step towards the establishment of NMR as a routine method in pulsed high magnetic fields.

To summarize, we have first described in detail a custom-built spectrometer and a probe head that meet the challenging requirements of pulsed field NMR. The high sensitivity of the apparatus allowed for a precise measurement of the magnetic field's time dependence.

We have developed a method to fit a local model of the field's time dependence to the measured *phase* data. After the pulse, the field is known with high precision (better than 1 ppm), and the time dependence can be removed from the data, so that the signals appear as if they were taken at stable, static field. This is demonstrated by effective signal averaging also for a maximum field strength of 62 Tesla.

With the ability to remove the influence of the time dependence from the data, other questions could be addressed. Clearly, the removal of the time dependence enables a systematic study of the field's inhomogeneity. We have measured the longitudinal inhomogeneity for one pulsed magnet. As expected by symmetry, the inhomogeneity can be described in terms of a quadratic expansion about the field center, but a rather large constant contribution remains opaque.

By performing an experiment in a dual coil we have shown that NMR has potential well beyond the field strengths discussed here; a first experiment at 90 Tesla is within reach.

We have demonstrated the first chemical shift measurement in a pulsed magnet as well as a measurement of the Knight shift of metallic aluminum at 60 Tesla. We found a relatively large Knight shift compared to the values in the literature; further experiments are required to provide more robust experimental evidence.

We have discussed first measurements of T_1 and T_2 that were analyzed in terms of basic models. For both measurements a precise knowledge of the flip angle seems to be the most urgent improvement. This could be obtained, e.g., through the permanent availability of a sweepable low-field magnet in which a nutation experiment could be performed.

Finally, we have exploited our knowledge of basic NMR methodology to measure with high precision the FID and spin echoes of ^{19}F in solid calcium fluoride. The data were analyzed in terms of a recent theory by Fine based on the notion of microscopic chaos. Both spin echo and FID experiments are in excellent agreement with his theory providing a possible path to a better understanding of quantum chaos in macroscopic many-body systems.

Acknowledgement

The work presented here would not have been possible without the persistent help and support of quite a number of people.

I am deeply grateful to Jürgen Haase who has been a mentor of mine for many years. I can hardly imagine a better supervision, be it in scientific working or in “scientific surviving”.

I am thankful to Boris V. Fine for numerous intense discussions about the implications of his theory and the great motivation he offered.

Various people have been involved in the work at the HLD. Sebastian Greiser assisted with the early experiments demonstrating signal averaging. Frederik Wolff-Fabris and (later) Erik Kampert did a great job as user support for my experiments. I am thankful to Thomas Herrmannsdörfer and Jochen Wosnitza for their on-going confidence in my work and pulsed field NMR in general. I would like to thank Jacob Schäfer for suggesting the successful chemical shift measurement of ^{19}F spins. I thank Bettina Jee for supplying the MOF sample.

I would like to thank Charles P. Slichter and Mark S. Conradi for very motivating feedback and discussions related to my work.

Jonas Kohlrantz was involved in both the work at the HLD as in the measurements on calcium fluoride; working with him was truly enjoyable and stimulating. Steven Reichardt was involved in the aluminum measurements at high field.

Many people have made the research that is documented in this thesis a most memorable time. Among them are Christof P. Dietrich, Steffen Karalus, Wilhelm Kossack, Steffen Pottel and Carsten Schuldt.

For the last two years of this thesis, Christina Kny’s admirable and warm care for my son Anton was truly invaluable.

I am most thankful to my family for the continued support, especially to Helena for the “collaboration” on all kinds of technical matters.

I am grateful to Ulrike and Anton for constituting my own little family; it’s the best place to be!

This work was supported by “Europäischer Sozialfond” ESF, “Investitionen in Ihre Zukunft” project no. 080935191 as well as by Deutsche Forschungsgemeinschaft within the Graduate School BuildMoNa. Part of this work was supported by EuroMagnet II, EU contract no. 228043.

A. Composition of the CaF_2 FID for B parallel (100)

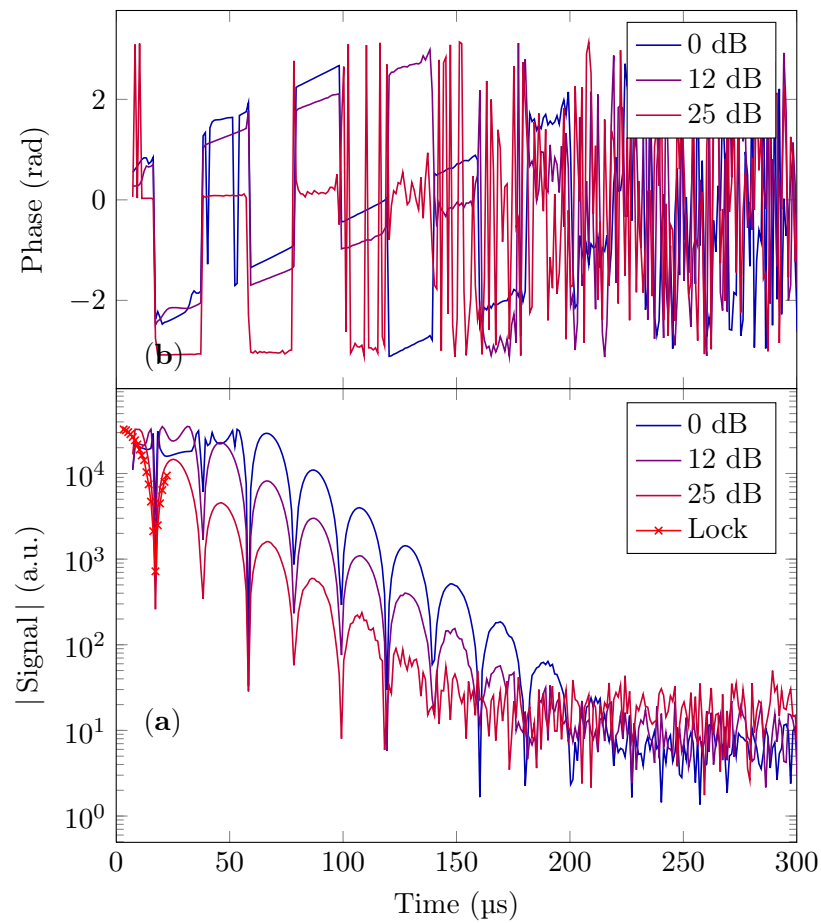


Figure A.1.: The same plot as in Fig. 6.7 for B parallel to the (100) direction of the crystal.

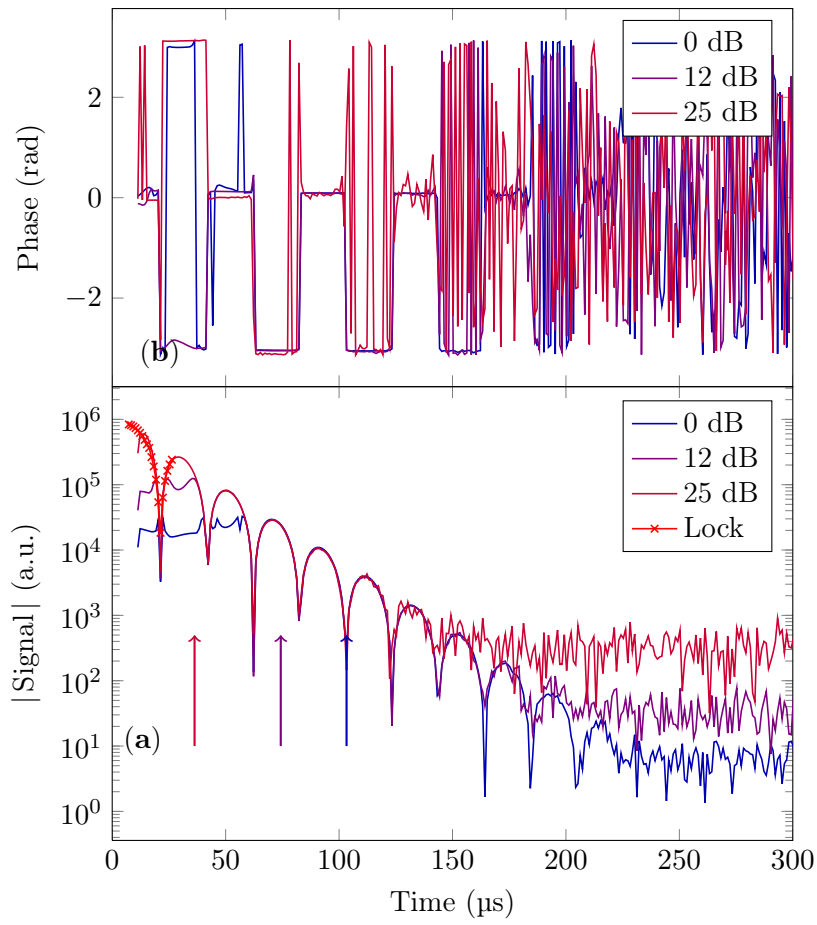


Figure A.2.: The same plot as in Fig. 6.8 for B parallel to the (100) direction of the crystal.

Bibliography

- [1] Haase, J., Eckert, D., Siegel, H., Eschrig, H., Müller, K. H., and Steglich, F. High-field NMR in pulsed magnets. *Solid State Nuclear Magnetic Resonance* **23**(4), 263–265, June (2003).
- [2] Haase, J. First ^2H NMR at 58 T. *Applied Magnetic Resonance* **27**(1), 297–302, March (2004).
- [3] Kozlov, M. B., Haase, J., Baumann, C., and Webb, A. G. 56 T ^1H NMR at 2.4 GHz in a pulsed high-field magnet. *Solid State Nuclear Magnetic Resonance* **28**(1), 64–67, July (2005).
- [4] Krämer, S. private communication with B. Meier, (2011).
- [5] Meier, B., Greiser, S., Haase, J., Herrmannsdörfer, T., Wolff-Fabris, F., and Wosnitza, J. NMR signal averaging in 62T pulsed fields. *Journal of Magnetic Resonance* **210**, 1–6, May (2011).
- [6] Fine, B. V. Long-time relaxation on spin lattice as a manifestation of chaotic dynamics. *International Journal of Modern Physics B* **18**(8), 1119–1195 (2004).
- [7] Fine, B. V. Long-time behavior of spin echo. *Physical Review Letters* **94**(24), 247601, June (2005).
- [8] Meier, B., Kohlrautz, J., and Haase, J. Eigenmodes in the long-time behavior of a coupled spin system measured with nuclear magnetic resonance. *arXiv:1112.3626*, December (2011).
- [9] Slichter, C. P. *Principles of Magnetic Resonance*. Springer Berlin, third enlarged and updated edition, February (2010).
- [10] Cowan, B. *Nuclear Magnetic Resonance and Relaxation*. Cambridge University Press, August (2005).
- [11] Abragam, A. *Principles of Nuclear Magnetism*. Oxford University Press, October (1983).
- [12] Levitt, M. H. *Spin Dynamics: Basics of Nuclear Magnetic Resonance*. Wiley & Sons, second edition, November (2007).

- [13] Van Vleck, J. H. The dipolar broadening of magnetic resonance lines in crystals. *Physical Review* **74**(9), 1168, November (1948).
- [14] Borckmans, P. and Walgraef, D. Irreversibility in paramagnetic spin systems: Free induction decay and spin diffusion. *Physical Review* **167**(2), 282, March (1968).
- [15] Borckmans, P. and Walgraef, D. Long-time behavior of the Free-Induction decay in paramagnetic spin systems. *Physical Review Letters* **21**(22), 1516, November (1968).
- [16] Bloembergen, N., Purcell, E. M., and Pound, R. V. Relaxation effects in nuclear magnetic resonance absorption. *Physical Review* **73**(7), 679, April (1948).
- [17] Belorizky, E., Fries, P. H., Helm, L., Kowalewski, J., Kruk, D., Sharp, R. R., and Westlund, P. Comparison of different methods for calculating the paramagnetic relaxation enhancement of nuclear spins as a function of the magnetic field. *The Journal of Chemical Physics* **128**, 052315 (2008).
- [18] Kowalewski, J., Egorov, A., Kruk, D., Laaksonen, A., Nikkhou Aski, S., Parigi, G., and Westlund, P. Extensive NMRD studies of Ni(II) salt solutions in water and water-glycerol mixtures. *Journal of Magnetic Resonance* **195**(1), 103–111, November (2008).
- [19] Kapitza, P. L. A method of producing strong magnetic fields. *Proceedings of the Royal Society A: Mathematical, Physical and Engineering Sciences* **105**(734), 691–710, June (1924).
- [20] Herlach, F. and Miura, N. *High Magnetic Fields: Science and Technology : Magnet Technology and Experimental Techniques*. World Scientific Publishing Company, , November (2003).
- [21] Zherlitsyn, S., Herrmannsdörfer, T., Wustmann, B., and Wosnitza, J. Design and performance of non-destructive pulsed magnets at the dresden high magnetic field laboratory. *Applied Superconductivity, IEEE Transactions on* **20**(3), 672–675 (2010).
- [22] Helm, T., Kartsovnik, M. V., Bartkowiak, M., Bittner, N., Lambacher, M., Erb, A., Wosnitza, J., and Gross, R. Evolution of the fermi surface of the Electron-Doped High-Temperature superconductor $\text{Nd}_{2-x}\text{Ce}_x\text{CuO}_4$ revealed by Shubnikov-de Haas oscillations. *Physical Review Letters* **103**(15), 157002, October (2009).
- [23] Andreev, A. V., Kuz'min, M. D., Narumi, Y., Skourski, Y., Kudrevatykh, N. V., Kindo, K., de Boer, F. R., and Wosnitza, J. High-field magnetization study of a $\text{Tm}_2\text{Co}_{17}$ single crystal. *Physical Review B* **81**(13), April (2010).
- [24] Sytcheva, A., Löw, U., Yasin, S., Wosnitza, J., Zherlitsyn, S., Goto, T., Wyder, P., and Lüthi, B. Magneto-Acoustic faraday effect in $\text{Tb}_3\text{Ga}_5\text{O}_{12}$. *Journal of Low Temperature Physics* **159**(1-2), 126–129, January (2010).

- [25] Zvyagin, S. A., Ozerov, M., Čižmár, E., Kamenskyi, D., Zherlitsyn, S., Herrmannsdörfer, T., Wosnitza, J., Wünsch, R., and Seidel, W. Terahertz-range free-electron laser electron spin resonance spectroscopy: Techniques and applications in high magnetic fields. *Review of Scientific Instruments* **80**(7), 073102 (2009).
- [26] Herrmannsdörfer, T., Krug, H., Pobell, F., Zherlitsyn, S., Eschrig, H., Freudenberger, J., Müller, K. H., and Schultz, L. The high field project at Dresden/Rossendorf: a pulsed 100 T/10 ms laboratory at an infrared Free-Electron-Laser facility. *Journal of Low Temperature Physics* **133**(1), 41–59, October (2003).
- [27] Wosnitza, J., Herrmannsdörfer, T., Skourski, Y., Zherlitsyn, S., Zvyagin, S. A., Drachenko, O., Schneider, H., Helm, M., Ghoshray, A., and Bandyopadhyay, B. Science at the dresden high magnetic field laboratory. *AIP Conference Proceedings* **1003**(1), 311–315, April (2008).
- [28] Pozar, D. M. *Microwave Engineering*. Wiley, third edition, February (2004).
- [29] Mizuno, T. and Takegoshi, K. Development of a cryogenic duplexer for solid-state nuclear magnetic resonance. *Review of Scientific Instruments* **80**(12), 124702–124702, December (2009).
- [30] Badilita, V., Kratt, K., Baxan, N., Mohmmadzadeh, M., Burger, T., Weber, H., Elverfeldt, D. v., Hennig, J., Korvink, J. G., and Wallrabe, U. On-chip three dimensional microcoils for MRI at the microscale. *Lab Chip* **10**(11), 1387–1390, April (2010).
- [31] Doty, F., Connick, T., Ni, X., and Clingan, M. Noise in high-power, high-frequency double-tuned probes. *Journal of Magnetic Resonance (1969)* **77**(3), 536–549, May (1988).
- [32] Hoult, D. I. and Richards, R. E. The signal-to-noise ratio of the nuclear magnetic resonance experiment. *Journal of Magnetic Resonance (1969)* **24**(1), 71–85, October (1976).
- [33] Hoult, D. I. The NMR receiver: A description and analysis of design. *Progress in Nuclear Magnetic Resonance Spectroscopy* **12**(1), 41–77 (1978).
- [34] Nyquist, H. Thermal agitation of electric charge in conductors. *Physical Review* **32**(1), 110, July (1928).
- [35] Levenberg, K. A method for the solution of certain problems in least squares. *Quart. Applied Math.* **2**, 164–168 (1944).
- [36] Marquardt, D. W. An algorithm for Least-Squares estimation of nonlinear parameters. *Journal of the Society for Industrial and Applied Mathematics* **11**(2), 431–441 (1963).

- [37] Haase, J., Eckert, D., Siegel, H., Eschrig, H., Müller, K., Simon, A., and Steglich, F. NMR at the frontier of pulsed high field magnets. *Physica B: Condensed Matter* **346-347**, 514–518, April (2004).
- [38] Zheng, G.-q., Katayama, K., Kandatsu, M., Nishihagi, N., Kimura, S., Hagiwara, M., and Kindo, K. ^{59}Co NMR at pulsed high magnetic fields. *Journal of Low Temperature Physics* **159**(1-2), 280–283, January (2010).
- [39] Gruschke, O. G., Baxan, N., Clad, L., Kratt, K., Elverfeldt, D. v., Peter, A., Hennig, J., Badilita, V., Wallrabe, U., and Korvink, J. G. Lab on a chip phased-array MR multi-platform analysis system. *Lab Chip*, December (2011).
- [40] Greiser, S. Diploma thesis, Leipzig (2011).
- [41] Carter, G., Bennett, L., and Kahan, D. Metallic shifts in NMR. *Progress in Materials Science* **20**, Part 1(0), 119–378 (1976).
- [42] Khan, H. R., Reynolds, J. M., and Goodrich, R. G. Magnetic field dependence of the knight shift in aluminum. *Physical Review B* **2**(12), 4796, December (1970).
- [43] Goodrich, R. G., Khan, S. A., and Reynolds, J. M. Knight shift in cadmium: Field and temperature dependence. *Physical Review B* **3**(8), 2379, April (1971).
- [44] Emsley, J. and Phillips, L. Fluorine chemical shifts. *Progress in Nuclear Magnetic Resonance Spectroscopy* **7**(0), 1–520 (1971).
- [45] Dolbier, W. R. *Guide to Fluorine NMR for Organic Chemists*. John Wiley & Sons, first edition, July (2009).
- [46] Pöpl, A., Kunz, S., Himsl, D., and Hartmann, M. CW and pulsed ESR spectroscopy of cupric ions in the Metal-Organic framework compound $\text{Cu}_3(\text{BTC})_2$. *The Journal of Physical Chemistry C* **112**(7), 2678–2684, February (2008).
- [47] Gul-E-Noor, F., Jee, B., Pöpl, A., Hartmann, M., Himsl, D., and Bertmer, M. Effects of varying water adsorption on a $\text{Cu}_3(\text{BTC})_2$ metal-organic framework (MOF) as studied by ^1H and ^{13}C solid-state NMR spectroscopy. *Physical Chemistry Chemical Physics* **13**(17), 7783–7788, April (2011).
- [48] Rowsell, J. L. and Yaghi, O. M. Metal-organic frameworks: a new class of porous materials. *Microporous and Mesoporous Materials* **73**(1–2), 3–14, August (2004).
- [49] Lowe, I. J. and Norberg, R. E. Free-Induction decays in solids. *Physical Review* **107**(1), 46, July (1957).
- [50] Engelsberg, M. and Lowe, I. J. Free-induction-decay measurements and determination of moments in CaF_2 . *Physical Review B* **10**(3), 822 (1974).

- [51] Sorte, E. G., Fine, B. V., and Saam, B. Long-time behavior of nuclear spin decays in various lattices. *Physical Review B* **83**(6), 064302, February (2011).
- [52] Morgan, S. W., Fine, B. V., and Saam, B. Universal Long-time behavior of nuclear spin decays in a solid. *Physical Review Letters* **101**(6), 067601 (2008).
- [53] Cho, H., Ladd, T. D., Baugh, J., Cory, D. G., and Ramanathan, C. Multispin dynamics of the solid-state NMR free induction decay. *Physical Review B* **72**(5), 054427 (2005).
- [54] Betsuyaku, H. Lowe-Norberg theory of Nuclear-Magnetic-Resonance free induction decay in solids. *Physical Review Letters* **24**(17), 934, April (1970).
- [55] Canters, G. and Johnson Jr., C. Numerical evaluation of moments and shapes of magnetic resonance lines for crystals and powders. *Journal of Magnetic Resonance (1969)* **6**(1), 1–14, January (1972).
- [56] Jensen, S. J. K. and Hansen, E. K. Sixth and eighth moments of the Magnetic-Resonance lines of a Dipolar-Coupled rigid lattice. *Physical Review B* **7**(7), 2910, April (1973).
- [57] Krylov, N. S. *Works on the Foundations of Statistical Physics*. Princeton University Press, December (1979).
- [58] Lin, Y., Lisitza, N., Ahn, S., and Warren, W. S. Resurrection of crushed magnetization and chaotic dynamics in solution NMR spectroscopy. *Science* **290**(5489), 118 –121, October (2000).
- [59] Jeener, J. Dynamical effects of the dipolar field inhomogeneities in High-Resolution NMR: spectral clustering and instabilities. *Physical Review Letters* **82**(8), 1772–1775, February (1999).
- [60] Sethna, J. P. *Statistical Mechanics: Entropy, Order Parameters and Complexity*. Oxford University Press, June (2006).
- [61] Fine, B. V., Elsayed, T. A., Sorte, E. G., and Saam, B. Asymptotic and intermediate long-time behavior of nuclear free induction decays in polycrystalline solids and powders. *arXiv:1201.1793*, January (2012).
- [62] Vollmers, K. W., Lowe, I. J., and Punkkinen, M. A method of measuring the initial behavior of the free induction decay. *Journal of Magnetic Resonance (1969)* **30**(1), 33–50, April (1978).